January 2017

Atomic-Level Structural Studies Of Rare-Earth Doped Sodium Phosphate Glasses Using High Energy X-Ray Diffraction And Complementary Techniques

Faisal Amir

ATOMIC-LEVEL STRUCTURE STUDIES OF RARE-EARTH DOPED SODIUM PHOSPHATE GLASSES USING HIGH ENERGY X-RAY DIFFRACTION AND COMPLEMENTARY TECHNIQUES

by

Faisal Amir
Master of Science, University of Minnesota, Duluth - USA, 2011

A Dissertation

Submitted to the Graduate Faculty

of the

University of North Dakota

in partial fulfillment of the requirements

for the degree, of

Doctor of Philosophy

Grand Forks, North Dakota
August
2017

This dissertation, submitted by Faisal Amir in partial fulfillment of the requirements for the degree of Doctor of Philosophy from the University of North Dakota, has been read by the Faculty Advisory Committee under whom the work has been done and is hereby approved.

Chairperson

(Yen Lee Loh)

This dissertation meets the standards for appearance, conforms to the style and format requirements of the Graduate School of the University of North Dakota, and is hereby approved.

Dean of the Graduate School

July 28, 2017

Date

PERMISSION

Title Atomic-level structural studies of rare-earth doped sodium phosphate glasses using high energy X-ray diffraction and complementary techniques

Department Physics and Astrophysics

Degree Doctor of Philosophy

In presenting this dissertation in partial fulfillment of the requirements for a graduate degree from the University of North Dakota, I agree that the library of this University shall make it freely available for inspection. I further agree that permission for extensive copying for scholarly purposes may be granted by the professor who supervised my dissertation work or, in his absence, by the chairperson of the department or the dean of the Graduate School. It is understood that any copying or publication or other use of this dissertation or part thereof for financial gain shall not be allowed without my written permission. It is also understood that due recognition shall be given to me and to the University of North Dakota in any scholarly use which may be made of any material in my dissertation.

Signature: 

Date 07/26/2017

Table of Contents

List of Figures

List of Tables

ACKNOWLEDGMENTS

I gratefully acknowledge the support of my advisor Dr. Kanishka Marasinghe for his support, guidance, patience and wonderful advice rendered throughout my graduate studies. I would also like to thank my committee members, Dr. Nuri Oncel and Dr. Loh for their valuable advice and support in completing this project. My thanks extend to Dr. William Schwalm and other professors, the secretary, technical staff, and all students in the Department of Physics and Astrophysics at the University of North Dakota for their unreserved help and support.

I would like to thank to Dr. Chris Benmore and Lawrie Skinner for their help in collecting and analyzing the HEXRD data at the Advance Photon Source. Many thanks go to Dr. May Stanley at the University of South Dakota for collecting the optical measurements.

Finally, I would like to thank my family and my sister Sahar Afshan, especially my Wife Perveen Akhter, for their continuous love, encouragement, support and being so wonderful towards me throughout my studies.

ABSTRACT

The atomic-scale structure of a series of $(RE_2O_3)_x(Na_2O)_y(P_2O_5)_{1-x-y}$ glasses *(RE = Pr, Nd, Er)* where $0.005 \leq x \leq 0.05$ has been characterized by high-energy X-ray diffraction technique (HEXRD). In addition, differential thermal analysis (DTA), Fourier transform infrared (FTIR) spectroscopy, and absorption and emission spectroscopy in visible and near IR ranges have been used as supplementary tools to validate structural features obtained from HEXRD techniques.Structural features such as inter-atomic distances and coordination numbers and their dependence on the concentration of RE_2O_3 have been obtained by analyzing pair distribution functions (PDF) extracted from diffraction data.

Coordination numbers for *P-O, Na-O, O-O,* and *P-P* were found to be independent of the RE_2O_3 concentration. In contrast, the *RE-O* coordination number varies between ≈ 8 and 7.2 as the RE_2O_3 concentration increases from 0.005 to 0.05. The variation of the bond distance between large rare-earth ions (*Pr,Nd*) and small rare-earth ion (*Er*) is approximately 0.2 Å, which is attributed to lanthanide contraction. The *Na-O* coordination number in these glasses was observed to ≈ 5.0 as the RE_2O_3 content increases. The overlapping correlation of *RE-O, Na-O,* and *O-O* in the same vicinity makes it difficult to calculate these coordination numbers.

DTA measurements were used for the investigation of thermal characteristics of glasses. From these measurements, it is evident that the glass transition temperature increases with increasing the RE_2O_3 $(RE = Pr, Er)$ content. FTIR was used to inspect the structural changes of the glasses. The doping of RE_2O_3 $(RE = Pr, Er)$ induces depolymerization of

the glasses at the Q^3 tetrahedral sites. The forming of the ionic linkages between phosphate chains is attributed to the increase in non-bridging oxygen (NBO). The cross-linkages density (CLD) increases with the RE_2O_3 ($RE = Pr, Er$) concentrations.

Absorption spectra for $x = 0.01$ of Er^{3+} and $0.005 - 0.05$ for Nd^{3+} doped glasses have been analyzed using Judd-Ofelt (JO) theory. The JO parameters have been used to predict radiative properties of luminescent levels of Er^{3+} and Nd^{3+} ions. Comparatively large photoluminescence lifetime $13.76\ msec$ ($x = 0.01$) for Er^{3+} and $476\ \mu sec$ (x = 0.005) for Nd^{3+} for the laser transition was observed. However, the quantum efficieny of the erbium doped glasses is ≈ 70 %. The influence of RE^{3+} ($RE = Er, Nd$) doping concentration on the emission spectra and lifetimes was investigated with model proposed by Auzel's limited diffusion model, in order to study the concentration quenching effect on luminescence. In this model, the fitting of the fluorescence lifetime experimental data gives us radiative lifetime (τ_0) and quenching concentration (N_0). For neodymium glasses, $\tau_0 = 467\ \mu sec$ and $N_0 = 5.98 \times 10^{20}\ ions/cm^3$ Nd^{3+} ion, and in erbium glasses, $\tau_0 = 12.4\ ms$ at $N_0 = 1.57 \times 10^{20}\ ions/cm^3$ for Er^{3+} ion. The Inokuti-Hirayama (IH) model has been applied to the non-exponential behavior of the decay profiles to investigate the mechanism involved in the energy transfer between the donors and acceptors. Emission spectra of rare earth phosphate glasses show that their fluorescence efficiency decreases with increasing rare-earth content even at relatively at low concentrations ($0.005 < x < 0.05$), suggesting that concentration quenching of lasing action may be present even at these concentrations.

CHAPTER 1

INTRODUCTION

The term “glass” implies an amorphous solid having a disordered atomic structure and exhibiting a region of glass transformation behavior regardless of the chemical constituent and method of preparation [1] [2]. In the last few decades, oxide glasses have attracted the attention of researchers and scientists’ due to their specific properties for many modern applications. Recent research on glasses is based on advanced uses such as X-ray protective glasses, fiber glasses, high refractive index glasses, photo-chromatic, and high-strength glasses.

About 100 years ago, phosphate glasses were developed for achromatic optical elements. These glasses have low dispersion and relatively high refractive indices compared to silicate-based optical glasses. Subsequently, alkaline-earth phosphate glasses drew attention due to their high transparency for ultra-violet light. But these early optical glasses had poor chemical durability stability, so their applications were limited. In the mid-twentieth century, researchers’ interest was drawn to alkali phosphates as they could be used in various industrial applications, such as sequestering agents for alkaline-earth metals and dispersants for clay processing and pigment manufacturing. More recently, phosphate glasses have been developed for a variety of specialty applications. Alkali alumino-phosphate compositions are used for specialty hermetic-seals. Zinc phosphate compositions can be co-formed with high temperature polymers to produce unusual

organic/inorganic composites. Iron phosphate glasses are used as nuclear waste hosts. Biocompatible phosphate glasses and glass-ceramics have medical applications. Amorphous lithium phosphates and phosphorous oxynitride glasses are used as solid-state electrolytes.

This chapter highlights the central concepts in glass formation that underpin the current understanding of the atomic-scale structure of glasses. An outline is given about the critical applications of phosphate glasses in different fields, after which a more general description is presented on glass network theory and the origin of the structural disorder observed in glassy systems. The discussion then focuses on the structural, vibrational, and optical properties of phosphate glasses.

1.1 Phosphate Glasses

1.1.1 Structure and Properties of Phosphate Glasses

There are three known phosphorus oxides P_2O_5 , P_2O_4, and P_2O_3 but only the pentoxide P_2O_5, can form a glass. This oxide glass former can be found in three crystalline forms, hexagonal, orthorhombic and tetragonal. All these three allotropic forms can form glasses when cooled from a melt. In both crystalline and glassy phosphates, the core building blocks are $(PO_4)^{-3}$ tetrahedra linked through a covalent bridging oxygen $(P-O-P\ linkages)$ to form various phosphate anions. These tetrahedra are classified using the Q^i terminology, where " i " represents the number of bridging oxygens per tetrahedron used initially in the description of aluminophosphate glasses [3] [4] as shown in Figure 1.1.

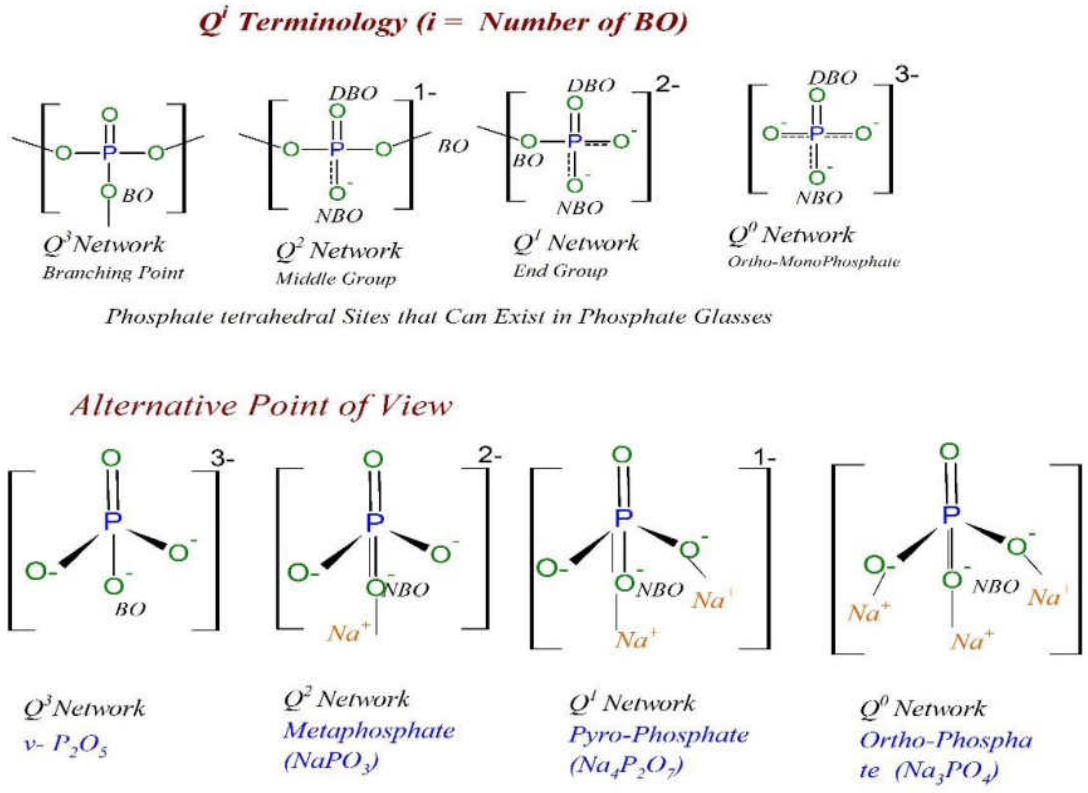

Figure 1. 1: Q-site network model for phosphate glasses. [5] [6].

The groups with different numbers of bridging oxygens are classified as Q^3- group (branching group),Q^2(iintermediate),Q^1(terminal) and Q^0(isolated) group. Each phosphorus-oxygen tetrahedral unit contains a maximum number of three bridging oxygens (BO) and a non-bridging oxygen (NBO), also called a terminal oxygen (TO). The presence of the terminal oxygen limits the number of cross-linkages to 3 in phosphorus glass. The terminal oxygen results from a short double-bond formed between phosphorus and oxygen with a significant $\pi - bond$ nature *[6]*. The $\pi - bond$ is more localized in pure P_2O_5 and can be partially delocalized on $P - O^-$ of *NBOs* in the following order $Q^3 \rightarrow Q^2 \rightarrow Q^1 \rightarrow Q^0$ by the depolymerization of the network. The number of cross-links in phosphate glasses is small as compared to those of silicate glasses of same metal oxide contents. On the other hand, a large number of terminal oxygen atoms exist. Thus, a high degree of flexibility remains for the orientation of the PO_4 group *[7]*. The extent of phosphate

structural depolymerization by the addition of a modifying oxide can be described either by the compositional dependence of the PO_4 tetrahedra distribution or by the compositional dependence of the bridging-to-non-bridging oxygen ratio. The pseudo-reaction in Equation 1.1 [5] summarizes the depolymerizing effects of the addition of a modifying oxide in term of $Q - network$ in Figure 1.2.

$$2Q^n + \ R_2O \ \rightarrow 2Q^{n-1} \qquad (1.1)$$

Equation 1.1 can also be used to predict the relative concentration of bridging to non-bridging oxygens. A $Q^3 - group$ has one terminal oxygen and 3/2 bridging oxygens, while $Q^2 - group$ has two terminal oxygens (considering there is no difference between the TO and NBO) and one (2/2) bridging oxygen. Therefore, ultraphosphate binary $(0 \leq x \leq 0.5)$ glass $(xR_2O).(1 - x)P_2O_5$ dependence on composition is given by Equation 1.2 by assuming that TO on Q^3 and NBO on Q^2 are the same [5].

$$\frac{BO}{NBO} = 0.5(3 - 4x) \qquad (1.2)$$

1.2 Classification of Phosphate Glasses

Phosphate glass networks are classified based on the oxygen-to-phosphorus ratio O/P which describes the degree of $P - O - P$ network polymerization or equivalently the linkages of neighboring PO_4 tetrahedra through bridging oxygen (BOs). Quantitatively the ratio of O/P determines the average number of bridging oxygens per P-tetrahedron and so hence the dominating Q^i species. The addition of glass modifiers such as alkali or alkaline earth oxides modifies the phosphate glass network from ultraphosphate to orthophosphate. These networks of phosphate glasses can be classified by the O/P ratios as [5].

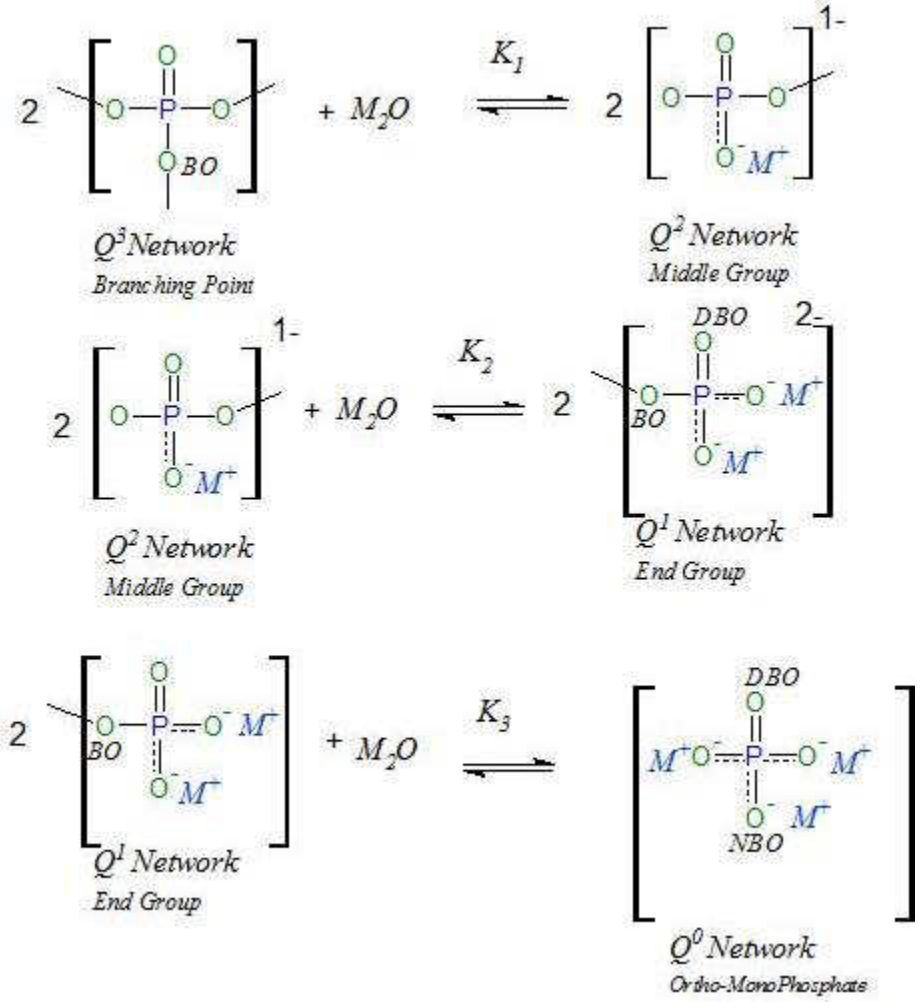

Figure 1. 2: Summarization of different pseudo-reactions in term of Q-network model. [6]

1. At $O/P = 2.5$ phosphate glass ($v - P_2O_5$) structure is a cross-linked network of Q^3 tetrahedra.
2. For $2.5 \leq O/P \leq 3.0$, we get ultraphosphate network (obtained by the addition of a metal oxide, MO) mainly made of Q^3 ($O/P = 2.5$) and Q^2($O/P = 3.0$) units. The network structure is partially depolymerized, and some of the bridging oxygens (BOs) in $P - O - P$ linkages are converted into NBOs in the $P - O - M$ linkage, which results in the conversion of Q^3 species to Q^2 species.[5] [8].

3. At $O/P = 3.0$, we get metaphosphate glasses. The glass network here is based entirely on Q^2 tetrahedra that form chains and rings which are linked by more ionic bonds between various metal cations and the non-bridging oxygens.
4. At $O/P > 3.0$ ($x > 0.5$), we get polyphosphate glasses characterized by decreasing Q^2 chain length and increasing fraction of Q^1 P-tetrahedra. The average chain length becomes progressively shorter as the O/P ratio increases.
5. At $O/P = 3.5$, we get the pyrophosphate glass network. It is dominated by phosphate dimers, two Q^1 tetrahedra linked by a common bridging oxygen. Pyro-phosphate glasses based on a variety of low-coordinated (CN < 6) conventional melt techniques can make metal oxides, including *SnO, ZnO CdO, PbO*, and Fe_2O_3. These latter glasses are analogous to silicate " invert glasses" [5]. The standard label of meta and pyrophosphate is shown in Figure 1.3.

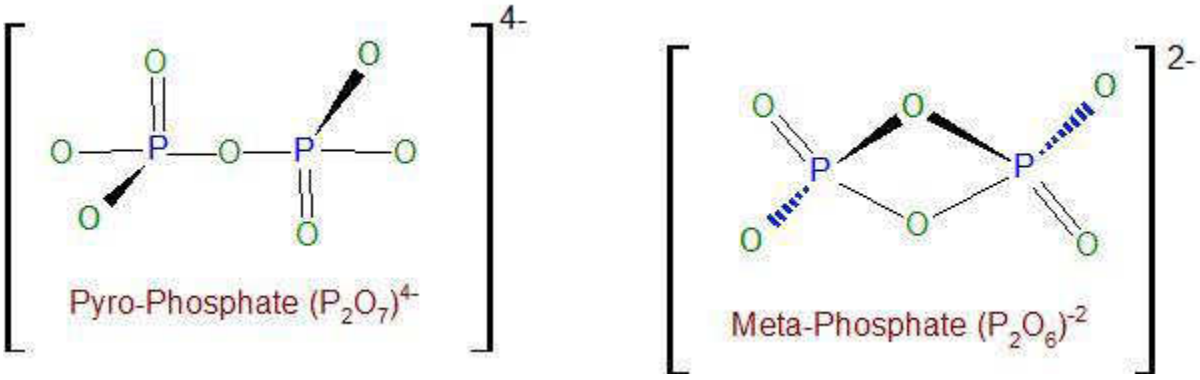

Figure 1. 3: The label for meta and pyro - phosphate glasses. [6]

6. *At* $O/P > 3.5$, we get an orthophosphate glass which contains isolated Q^0 (PO_4^{3-}) tetrahedra. The Transformation of Q-Network from pyro to Orthophosphate is shown in Figure 1.4.

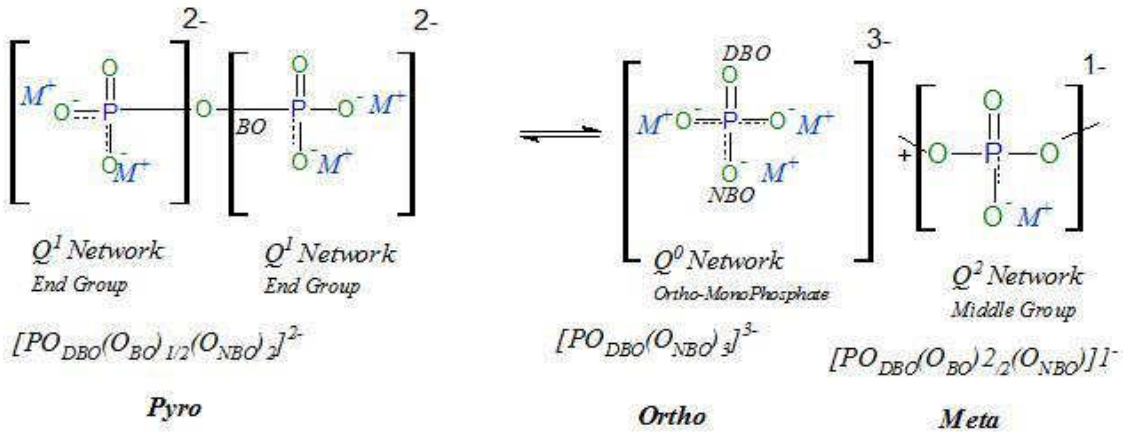

Figure 1. 4: Network modification of pyro phosphate glass to ortho network by the addition of modifier M. [6]

1.3 Applications of Phosphate Glasses

Phosphate glasses have been studied and commercialized for a variety of applications because of their useful physical properties including controllable chemical durability in aqueous environments, high thermal expansion coefficient, and relatively low melting and processing temperatures [9] [10]. Properties and applications of phosphate glasses vary dramatically with different compositions. This flexibility of phosphate glasses is due to the possibility to add many alkali, alkaline earth, transition metals, and rare-earth oxides to modify the structure and thus the properties. The outstanding thermal properties of phosphate glasses such as that mention above and low softening and transition temperatures and high electrical conductivity make them a material of choice for many technological applications as compared to other oxide glasses [11] [12] [13]. In addition to these thermal properties, attractive optical properties of rare-earth phosphate glasses such as rare-earth stimulated emission cross section, low thermal-optical coefficient and high ultraviolet transparency make them good candidate for laser media[11] [14].

In phosphate glasses, the glass former component is P_2O_5. The pure P_2O_5 has a melting point of 560 ℃, a boiling point of 605 ℃, a thermal-expansion-coefficient $\alpha = 13.7 \times 10^{-6}$ ℃$^{-1}$

and a refractive index of $n_e = 1.493$ ($\lambda = 546.1\ nm$) [3]. The UV edge of pure P_2O_5 is less than $150\ nm$, but absorption of water can shift it towards longer wavelength: $270\ nm$ for HPO_3 for example [3].

1.3.1 Chemical Durability

The chemical durability of phosphate glasses makes them useful in many other applications. The chemical durability can be varied from low to high by the additions of network modifying or network forming oxides to fit the needs of a particular application. Some applications of low chemical durable glasses are:

- Hard water treatment in which amorphous $NaPO_3$ is used as a sequestering agent to soften water since it has high solubility in aqueous solution
- Phosphate glass fertilizers are preferred over conventional mineral fertilizers due to their long-lasting action, and also, they are not pollutant [15] [16].
- Phosphate glasses as biomaterials have numerous applications in the engineering of hard and soft tissue essential for the repair and restoration of damaged and diseased tissues [17]. In Additions, copper, silver and gallium phosphate glasses can be used in antibacterial systems and drug delivery devices [18] [19].

On the other hand, phosphate glasses with high chemical durability are employed in applications, host matrices for vitrification of nuclear waste, sealing glassed, and fast-ion conductors for battery applications [20].

1.3.2 Optical Applications

Phosphate glasses have low optical dispersion and relatively high refractive indices as compared to silicate-based optical glasses. Rare-earth phosphate glasses [5] [21] [22] exhibit

interesting semiconductor properties, magneto-optical properties and magnetic transition properties. Such glasses can be used in applications such as spin glasses or optical isolators and optical switches [23] [24] [25] [26]. Alkaline earth phosphate glasses with a wide window of optical transmission, including a high transparency for ultraviolet light, make them suitable for optical systems [11] [27] [28]. They are used for high power laser applications because certain compositions enable large rare-earth cation content and low thermal-optical coefficient as compared to silicate glasses [11] [29]. Furthermore, their high tolerance for accommodating rare-earth ions has led to applications such as sensors, detectors, and receivers for medical and communication use [5]. For example, cerium alumino-phosphate glasses with a particular concentration of cerium are useful in high radiation conditions.

1.3.3 Sealing Glasses

The low glass-transition temperature and the high thermal expansion coefficient of phosphate glasses make them the material of choice for glass-metal sealing applications [9] [12] [13]. The thermal expansion coefficient for phosphate glasses is of the order of $18 \times 10^{-6}\ ℃^{-1}$. This is 36 times greater than silicate glasses [13]. Phosphate glasses can also be used in hermetic seals between glasses and high expansion metals such as aluminum. Alkali alumino-phosphate glasses with glass transition temperature under $400\ ℃$ have been developed for specially hieratics seals because of high thermal expansion coefficients (greater than $150 \times 10^{-7}\ ℃^{-1}$) [13]. Also, the sealing can be accomplished below the fusion temperature of metals. For examples, the range of their thermal expansion coefficients led to the development of sealing glasses based on $Na_2O/K_2O/Li_2O$ aluminophosphate glass composition [30].

Glass structure flexibility, low melting, and working temperature, and good thermal stability make phosphate glasses a better matrix for nuclear waste storage as compared to borosilicate

glasses for certain types of nuclear wastes. For example, lead-iron phosphate glasses have 100 - 1000 times' lower dissolution or corrosion rate than borosilicate glasses. Furthermore, they have lower working temperature(by approximately $100 - 250$ ℃) and lowers melt viscosities [31]. Iron phosphate glasses with Fe/P ratios between 1:3 and 2:3 can be used for the vitrification of high-level nuclear waste. It has an excellent chemical durability, which can be equivalent to or superior to silicate and borosilicate glasses [32] [33] [34] [35]. The chemical durability of several iron phosphate glasses vitrified with several types of simulated high-level nuclear waste meet all of the current US Department of Energy (DOE) requirements [32] [36].

1.4 Vibrational Properties of Phosphate Glasses

The absence of long-range order or periodicity in glasses has made it difficult to investigate the atomic arrangement and molecular interaction of them. However, much of the solid-state theory depends on crystalline symmetry, and it is precisely the lack of periodic structure in glasses which makes their study interesting. Zachariasen's [37] random network theory of glasses set phenomenological criteria useful in predicting whether a particular oxide is likely to form glasses and can be called a network former such as SiO_2, or P_2O_5 belong to this group. Cations of glass formers are highly charged, have small ionic radii and are tetrahedrally coordinated to oxygen. The cations which do obey the Zacharisen's rules are glass modifiers such as Na^+, K^+ and Ce^+.

These oxides have large ionic radii, and they prefer to be localized in octahedral oxygen environments. As mentioned previously,$v - P_2O_5$ and $c - P_2O_5$ structures consist of a PO_4 tetrahedra bonded with adjacent tetrahedra via bridging oxygens (BOs) forming ring -like structures as shown in Figure 1.5.

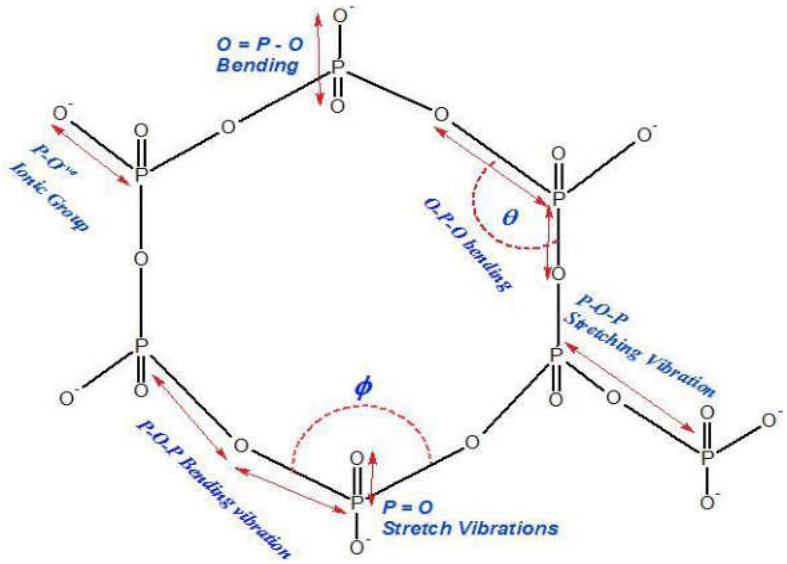

Figure 1. 5: Structure of pure vitreous $\boldsymbol{P_2O_5}$*, which consist of distinct double bonds and P-O-P linkages. [38]*

The additions of the cations depolymerize the phosphate network and also breaks these rings into chains at metaphosphate compositions. These chains are linked together by the interaction between the metal cations and the non-bridging oxygens (NBOs) of the glass former as shown in Figure 1.6.

Infrared and Raman spectroscopy can be used to probe the nature of the bonds between the metal cation and its surrounding oxygens. Specifically, the vibrational spectra can distinguish those metal cations which exhibit a predominantly covalent interaction with oxygen from those metal cations which show mainly ionic interactions with the polyphosphate anionic chains [40] [41]. The IR spectroscopy is a useful tool in studying the changes that take place in the glass network and is sensitive to short-range ordering and local interaction in the glass [38].

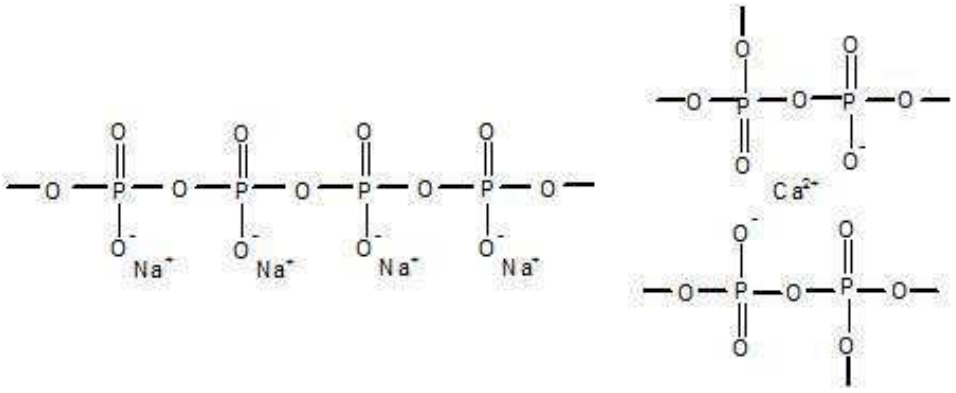

Figure 1. 6: Addition of modifier in phosphate glass results in the conversion of the 3-D network to linear chains. This linear chain structure results in cleavage of P-O-P linkages and creates NBOs in a glass. [39]

Many researchers [42] have applied IR spectroscopy to explain various structural aspects of phosphate glasses. Most of these studies were based on the assignment and shift of IR absorption bands. However, a more recent study used deconvolution method [43] for analyzing the IR spectra of borate glasses to determine the concentration of borate structural units. This deconvolution method has now become very useful in the analyses of IR spectra [39].

In phosphate glasses, the frequency of the $P = O$ band is at $1300 - 1190\ cm^{-1}$. This high frequency is related to the stretch vibration of $P = O$ due to the asymmetry of PO_4 tetrahedra. The frequency of $P = O$ is greatly influenced by the chemical nature of the substitutional group on phosphorus and also by the formation of hydrogen bonding [44] [45].

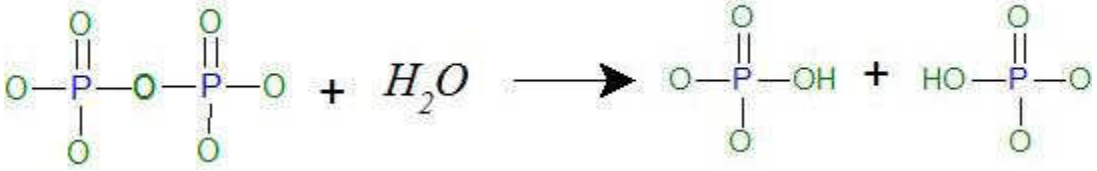

Figure 1. 7: Depolymerization of phosphate network due to presence of water. [5]

The absorption of water in to glass structure also depolymerize the phosphate network and form $P-H\ modes$(OH group $(2400-2300\ cm^{-1})$) and weak $P-O-H$ $(2700\ cm^{-1})$ as shown in Figure 1.7.

The sensitivity of $P=O$ to the formation of hydrogen bonding lower the frequency as compared to that of P_2O_5. However, this bond is not observed in metaphosphate glasses [46], because of indifference between the NBOs and DBOs and the formation of a unified $(PO_2)^{-ve}$ terminal group. These groups exhibit symmetric $(1140-1320\ cm^{-1})$ and asymmetric $(1000-1170\ cm^{-1})$ vibrations modes. At lower frequencies, symmetric $(1030-1170\ cm^{-1})$ and asymmetric $(940-1025\ cm^{-1})$ vibrational modes of $(PO_3)^{2-}$ were observed due to the incorporation of more network modifiers in to the glass network.

One more particular feature of the vibrational spectra of phosphate is the fact that the asymmetric $(850-1060\ cm^{-1})$ and symmetric $(650-800\ cm^{-1})$ stretching vibrations of the $P-O-P$ bridges. The $P-O-P$ asymmetric vibrations had been observed to shift towards the lower frequencies with increasing length of the $P-O-P$ chain. The frequency shifts resulting from the increase in the $P-O-P$ bond angle can by calculated from Equation 1.3 [47].

$$\nu_s = 1330\sqrt{k\left(\frac{1}{M_p}+\frac{1}{M_O}\,(1+cos\theta)\right)}$$

$$\nu_{as} = 1330\sqrt{k\left(\frac{1}{M_p}+\frac{1}{M_O}\,(1-cos\theta)\right)} \qquad (1.3)$$

Normal modes of phosphate chains in metaphosphate composition [48] are shown in Fig 1.8 along with bending vibration of phosphate polyhedra and $O-P-O$ bending modes.

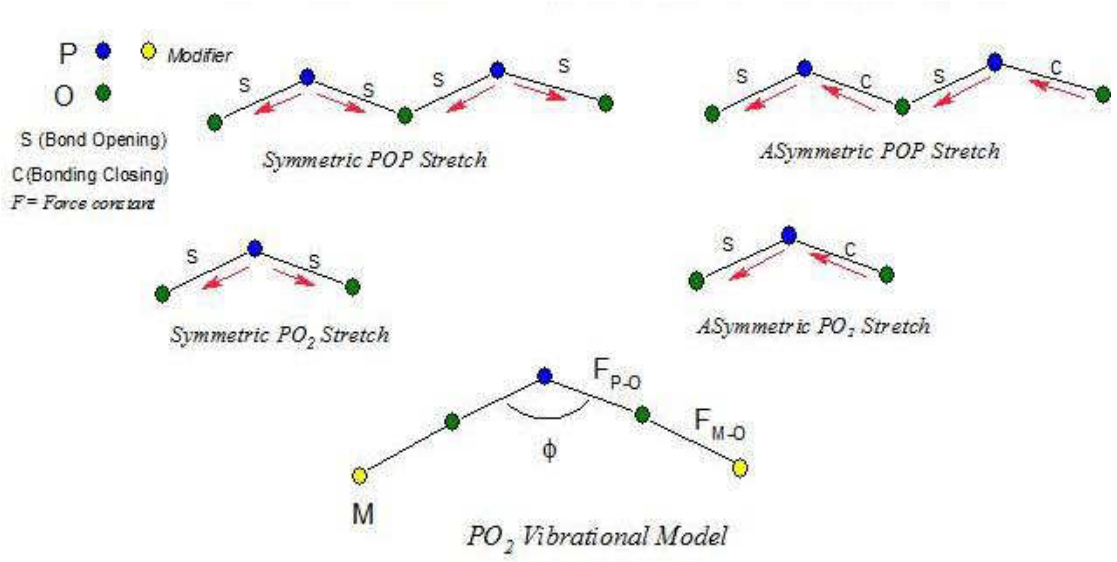

Figure 1. 8: Different vibrational modes in meta- phosphate chain. [48]

1.5 Optical Properties of Phosphate Glasses

Optical properties of rare-earth ions are widely made use of in lasers, amplifiers, up-conversion devices, scintillators and Faraday rotators. Various radiative and non-radiative transitions of the rare-earth ions between the 4f levels extend from the ultraviolet to the infrared region. Therefore, the absorption and emission spectroscopy is a useful tool for the characterization of the role of rare-earth ions in glasses. The knowledge of the relationships between the host glasses and the rare-earth ions is essential to design glasses for specific applications.

Spectroscopic properties of rare-earth ions are influenced by the host glass composition. Local structure and bonding features are characterized by covalency, asymmetry, coordination number and the distance to the ligand of the rare-earth sites. Furthermore, long-range effects such as rigidity and ionic packing ratio have an influence the spectroscopic properties. Hence, spectroscopic properties of the rare-earth ions can be used to investigate the local structure and

bonding around them [49] [50]. Incorporation of the rare-earth ions in the glasses structure can range from sparse random distribution to the formation of rare-earth pairs or clusters.

1.5.1 Electronic Structure of Rare-Earth Ions

The rare-earth ions of interest are the lanthanides, a group of fourteen elements from atomic number 57 (lanthanum) to 71 (lutetium), placed in the sixth period of the periodic table and characterized by filling of the 4f shell. The neutral atom ground state configuration of a Xenon core ($1s^2\ 2s^2 2p^6 3s^2 3p^6 3d^{10} 4s^2 4p^6 4d^{10} 5s^2 5p^6$) with two outer electrons $6s^2$ and varying numbers of $4f$ electrons. Their oxidation sate is $+3$, having lost their $6s$ electrons and one electron from the $4f$ shell, leaving the ions La^{3+} through Lu^{3+} with electronic configuration of the form $[Xe]4f^N$, with N varying from 0 to 14.

Optical properties of the rare-earth ions in the visible and near infrared spectral region are determined by the $4f$ electrons, which are well shielded by the outer $5s$ and $5p$ electrons [51] [52] [53]. As a consequence of this screening, the interaction between the $4f$ electrons and the surrounding medium is very weak, both with the crystal field of the host and the lattice phonons. This result in a narrow spread of the Stark-level structure.

The energy levels for a given electronic configuration can be determined and labeled using the quantum numbers L, S, and J, where L is the total orbital angular momentum, S is the total spin and J is the total angular momentum. In Russell-Saunders coupling scheme the value of L and S are obtained by combining the l and s values of all electrons, and J is calculated as $L + S$. The different J states have separations usually on the order of $10^3\ cm^{-1}$. Only the electrons in the $4f$ shell contribute to the calculation. The L and S values are zero for filled shells. Therefore, all the optical transitions take place within the $4f$ shell. However, in principle, they are forbidden due to

the parity selection rules of the electric dipole transitions. Nevertheless, these transitions, although characterized by low probabilities [54], are observed due to the mixing of the $4f^N$ states with empty higher-lying states of opposite parity $4f^{N-1}5d$ induced by the crystal field [55].

Table 1.1: Multipole operators and selection rules.

Operator			***Selection Rules***			
Operator		Parity	S	L	J	Parity
Electric Dipole	$\vec{P} = -e\sum_i \vec{r_i}$	Odd	$\Delta S = 0$	$\Delta L = 0, \pm 1$	$\Delta J = 0, \pm 1$	Opposite
Magnetic Dipole	$\vec{M} = -\frac{e\hbar}{2m}\sum_i \vec{l_i} + 2\vec{s_i}$	Even	$\Delta S = 0$	$\Delta L = 0$	$\Delta J = 0, \pm 1$	Same
Quadrupole	$\vec{Q} = \frac{1}{2}\sum_i (\vec{k}.\vec{r_i})\vec{r_i}$	Even	$\Delta S = 0$	$\Delta L = 0, \pm 1, \pm 2$	$\Delta J = 0, \pm 1, \pm 2$	Same

These transitions are called “weakly allowed." Whereas typical upper-state decay times are of the order of a few nanosecond in the case of allowed transitions for spontaneous emission. Weakly allowed transitions can have upper-state decay times typically between microseconds and milliseconds. Such long-lived levels are called metastable states. The selection rules are summarized in Table 1.1 [54]. The crystal field, beside causing the parity mixing also causes a splitting of the energy levels due to the Stark effect, typically on the order of $10^2\ cm^{-1}$ and are shown in Figure 1.9 [54].

Figure 1. 9: Effect of different terms of the Hamiltonian on the energy splitting. [54]

1.5.2 Spectroscopic Investigation of Rare-Earth Ions

1.5.2.1 Absorption Spectrum

Optical absorption and fluorescence spectroscopy are important techniques in the study of RE^{3+} doped systems because they allow the determination of natural frequencies of Ln^{3+} ions. The $4f$ electronic orbitals in RE^{3+} ions are incompletely filled. So, the ions absorb electromagnetic radiation in the spectral regions of ultraviolet, visible and the near-infrared [51]. The intra–$4f^n$ transitions and, the inter$-\ 4f^n \rightarrow\ 4f^{n-1}\ 5d^1$ transitions or charge transfer transitions occur in these regions. It is also possible to correlate the positions of these $4f \rightarrow 5d$ transitions with the standard (III-II) and (IV-III) reduction potentials for the lanthanides [56] [57].

Optical properties of RE^{3+} ions in a solid matrix are affected by changes in the environment of the RE^{3+} ion and its interaction with ligands. According to the Judd-Ofelt (JO) theory [58] [59] intensities of a set of absorption lines for a particular RE^{3+}ion in any matrix is characterized by three intensity parameters Ω_λ $(\lambda = 2, 4\ and\ 6)$. These parameters depend on the symmetry of the crystal field (CF) at the RE^{3+} site and the strength of covalence character of the Re^{3+}ion-ligand bond. Therefore, it is of interest to study the dependence of these intensity parameters on the glass composition. From these parameters, several important optical properties such as radiative transition probabilities, radiative lifetimes (τ_R) of the excited states and branching ratios (β) can be estimated.

1.5.2.2 Fluorescence Spectrum

The fluorescence spectrum can also be analyzed by essentially the same procedure as for the absorption spectrum except that the nature of the emission process will yield additional information concerning the ground-state multiplets of the ion. Fluorescence involves an optical

transition between electronic states which is characteristic to the radiating substance. Depending upon the type of fluorescing ion and its environment the radiation lifetime of the excited electronic states varies from 10^{-10} to 10^{-1} s. In the case of RE^{3+} ions, the most striking feature of the fluorescent emission is that it occurs in the spectral region where the crystal or glass is non-absorbing. RE^{3+} ions act as great fluorescing centers in a matrix. The fluorescence of an active RE^{3+} ion is influenced by the asymmetry of the surrounding binding forces. The position (λ_p), intensity full width at half maximum of the emission band ($\Delta\lambda_p$), and the lifetime (τ_R)of the fluorescing state are affected by the coordination environment. The stimulated emission cross-section, $\sigma(\lambda_p)$, one of the important parameters which determine laser characteristics of a given transition of RE^{3+} ion, can be evaluated from the emission studies. The experimental branching ratios, β_R, equal to the relative intensities of the emission bands of transitions to the same ground level, can also be evaluated from the emission studies. All these parameters are used to compare the theoretical branching ratios predicted from the JO theory [58] [59]. For a given RE^{3+}ion, above parameters can be varied over a wide range by changing the composition of the material.

1.5.2.3 Lifetime of Excited States

The luminescence lifetime of a given energy level is the time constant describing the decay of ions from that level which is exponential in the absence of energy-transfer processes. It is also defined as the time needed for an ensemble of ions excited to a certain energy level to decrease to the ≈ 0.37 (*1/e*) of its original number. It is inversely proportional to the probability per unit time of the decay of an ion from that level. The inverse of the luminescent lifetime can be written as a sum of inverse lifetimes which characterize the different decay paths. These paths can be radiative or non-radiative. Radiative decay results in the spontaneous emission of a photon. In non-radiative

decay, the energy is transferred to phonons, i.e., vibrations of the host matrix. The following equation relates the various contributions to the luminescence lifetime:

$$\frac{1}{\tau\,(J)} = A\,(J) + A_{non-rad}\,(J \rightarrow J-1) \tag{1.4}$$

where τ is the luminescence lifetime of level J and $A_{non\text{-}rad}$ is the decay rate constant of multiphonon relaxation from level J to level $J-1$, related to the energy gap ΔE between one energy level and the next lower level by the equation [55] [60]

$$A_{non-rad} = C\,[n(T)+1]^{p} e^{-\alpha\,\Delta E} \tag{1.5}$$

where C and α are host-dependent parameters, p is the number of phonons necessary to bridge the energy gap, and $n(T)$ is the Bose-Einstein occupation number for the effective phonon mode at the temperature T given by

$$n(T) = \frac{1}{Exp\left[{h\tilde{\nu}c}/{k_B T} - 1\right]} \tag{1.6}$$

In Equation (1.6), $h\tilde{\nu}c$ is the phonon energy described in wavenumbers, $\tilde{\nu}$ which are usually on the order of $10^3\ cm^{-1}$ in glass materials. Given $p = {\Delta E}/{h\tilde{\nu}c}$ Equation. (1.5) can be rewritten as

$$A_{non-raad} = C \exp\left[\left(\frac{ln(n(T)+1)}{h\tilde{\nu}c} - \alpha\right)\Delta E\right] \tag{1.7}$$

Because $\frac{ln(n(T)+1)}{h\tilde{\nu}c}$ $(\approx 10^{-5}\ cm) << \alpha\ (\approx\ 10^{-3}\ cm)$ [55], we obtain

$$A_{non-raad} = C \exp[(-\alpha)\Delta E] \tag{1.8}$$

1.5.2.4 Energy Transfer Between Ions

Transitions between energy levels due to absorption, spontaneous and stimulated emission, and non-radiative decay, all of which were described above, are single-ion processes. As the

dopant concentration increases and the ions get spatially closer to one another, energy transfer processes between neighboring ions may occur. These processes are believed to occur mainly due to an electric dipole-dipole interaction and are thus proportional to R^{-6}, where R is the distance between two ions. Moreover, they can be either resonant or non-resonant (involving the creation or destruction of phonons). Non-radiative transitions are multiphonon and energy transfer processes. multiphonon relaxation is affected by the electron-phonon coupling strength and phonon energy of the host matrix. Cross-relaxation is an energy transfer process between a given type of the rare-earth ions. It plays an important role at higher rare-earth concentration. Its probability depends on the distance and multipolar interaction between the rare-earth ions. The distance is determined by the distribution of the rare-earth ions in the matrix. The interaction is characterized by the so-called micro parameters of energy transfer processes.

Energy migration occurs when energy is transferred from an excited ion (donor) to a neighboring ion initially in its ground state. The first ion relaxes to the ground state and the second is excited. This process is called a donor-donor transfer because the newly excited ion can act as a donor ion for a subsequent energy-transfer process. This process can eventually result in loss of excitation through energy dissipation at an impurity (such as an OH^- group). Moreover, it can enhance the probability of occurrence of the following process.

Energy-transfer upconversion (ETU) is the process in which energy transferred from an excited ion (donor) to a neighboring ion which is also excited. The first ion relaxes to the ground state and the second is excited to an even higher state. This process is called donor-acceptor transfer. Different types of energy-transfer processes described above are depicted in Figure 1.10.

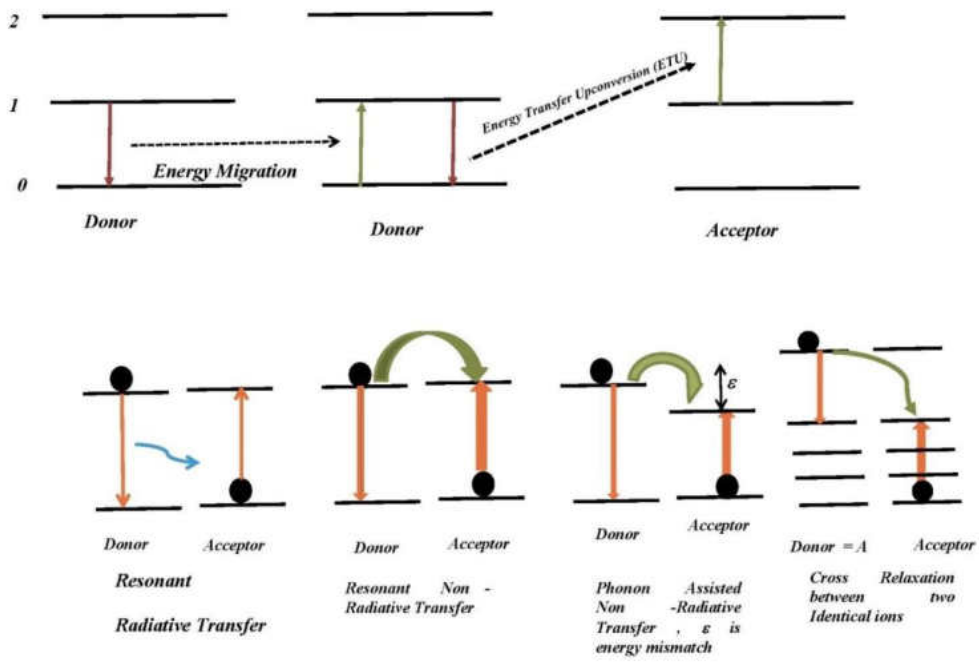

Figure 1. 10: Different energy transfer processes between the ions. [50]

1.5.3 Judd-Ofelt (JO) Theory

The Judd-Ofelt theory [58] [59]can be applied absorption spectrum of a rare-earth-ion-doped material to successfully calculate and characterize optical transitions occurring in the rare-earth-ion-doped material itself.

According to Judd-Ofelt theory, the electric dipole line strength $S_{cal}(cm^2)$ of the transition between the initial state J characterized by the quantum numbers (S, L, J) and the final state J' given by the quantum numbers (S', L', J') can be written as [61]

$$S_{cal}(J \rightarrow J') = \sum_{t=2,4,6} \Omega_t \left|\langle (S,L), J \| U^{(t)} \| (S',L'), J' \rangle\right|^2 = \Omega_2 \left[U^{(2)}\right]^2 + \Omega_4 \left[U^{(4)}\right]^2 + \Omega_6 \left[U^{(6)}\right]^2 \quad (1.9)$$

Here, $\Omega_t(t = 2,4,6)(cm^2)$ are the Judd-Ofelt parameters, characteristic of the ion host interaction, and $U^{(t)}(t = 2,4,6)$ are the doubly reduced matrix elements which depend only on the rare-earth ion because they are calculated with Eigenfunctions of the free ion. Since they are independent of the host, these values can be obtained from literature [62] [52]. In the standard Judd-Ofelt technique, the three Judd-Ofelt parameters Ω_2, Ω_4 and Ω_6 are determined by measuring the absorption line strengths for a number of ground-state transitions.

The measured line strength $S_{meas}(cm^2)$ of the chosen bands can be determined using the expression:

$$S_{meas}(J \rightarrow J') = \frac{3ch\,(2J+1)}{8\pi^3 \bar{\lambda}\, e^2} \left[\frac{9n}{(n^2+2)^2}\right] \int_{manifold} \sigma_{abs}(\lambda)\, d\lambda \qquad (1.10)$$

where e is the elementary charge, J is the angular momentum of the initial state, and n is the wavelength-dependent refractive index which is determined from Sellmeier's dispersion equation [59].

A least-square fit of S_{meas} to S_{calc} is used to obtain the values of the three Judd-Ofelt parameters $\Omega_t(t = 2,4,6)$, which can then be applied to Equation. (1.9) to calculate the line strengths corresponding to the transition from the upper manifold states to their corresponding lower-lying manifold states. With these line strengths, we can calculate the radiative decay rate constants $A(J \rightarrow J')$ of electric dipole transitions between an excited state J and lower-lying manifolds J'.The total radiative decay rate constant A and radiative lifetime τ_{rad} of each excited state J and the radiative branching ratios $\beta(J \rightarrow J')$ using the following relationships

$$A(J \rightarrow J') = \frac{64\,\pi^4 e^2}{3h(2J+1)\,\lambda^3}\left[\frac{n(n^2+2)^2}{9}\right] S_{calc}(J \rightarrow J') \quad (1.11)$$

$$\frac{1}{\tau_{rad}(J)} = A(J) = \sum_{J'} A(J \rightarrow J') \quad (1.12)$$

$$\beta(J \rightarrow J') = \frac{A(J \rightarrow J')}{\sum_{J'} A(J \rightarrow J')} = A(J \rightarrow J')\tau_{rad}(J) \quad (1.13)$$

1.5.3.1 Variations in Judd-Ofelt (JO) Parameters

According to JO theory, the spontaneous emission probabilities of forced electric dipole transitions of rare-earth ions can be calculated from measurements of absorption, refractive index, and density of samples. Three intensity parameters ($\Omega_t, t = 2,4,6$) associated with glass composition are used to calculate emission probabilities. The relationship between these parameters and the nature of glass host is of particular interest to the development of new optical applications.

Ω_2 parameter increases with increasing covalency and asymmetry at the rare-earth sites. The effect of covalency on Ω_2 decreases, which depends on the energy difference between the $4f$ and $5d$ states of the rare-earth ions [49] [63]. The degree of covalency is determined by the nephelauxetic ratio (the measure of the covalency between rare-earth ions and surrounding ligand) of $RE^{3+}, f \rightarrow d$ absorption band. Ω_2 increases linearly with β as the phosphate contents in the glass increases [49]. It depends strongly on the ionic radius of modifier cations (of glasses) which in turn influences the polarizability of oxygen around RE^{3+}. It also increases with an increase in the valence of the network-forming Mn cation (in the case of glasses) and slightly increases with the number of electrons of RE^{3+} ions. On the other hand, Ω_4 is affected by the factors causing changes

in both Ω_2 and Ω_6. The dependency on the covalency of Ω_6 is different than that for Ω_2. It is more affected by the radial integral between the $4f$ and $5d$ states of the rare-earth ions. Increasing $\sigma-$ electron donation from the ligand to the rare-earth ions within the $\sigma-$bond, decreases the radial integral. Thus Ω_6 decreases as the electron density donated from the ligands increases, and the Coulomb interaction between the RE^{3+} ion and the ligands decreases.

The variation of these intensity parameters depends on the type of network modifier more than the concentration of the network modifier except in the case of Ω_2 of borate glasses. Hence, the parameters are not expected to be significantly affected by the concentration of non-bridging oxygen. It is also well known that Ω_2 is sensitive to local structure in the vicinity of RE^{3+} ions. In all the glass system (silicate, borate and phosphate) similar variation of $\Omega_4, \Omega_6$with composition has been observed [64] [65].

In phosphate glasses, Ω_2 varies systematically with the ionic radii of the network modifier because phosphate glasses are composed of phosphate chain and RE^{3+} ion sit comfortably into certain sites in the chain and become network modifier. This site selectivity of Nd^{3+} ions in phosphate glasses is supported by the observation that the bandwidth of the emission spectrum of Nd^{3+} in phosphate glasses was narrower than that in silicate glasses. Furthermore, the polarizability of oxygen ions around Nd^{3+} ions affects the radiative property and the covalency of the $Nd-O$ bond. The covalency of the bond also depends on the electron donating power. Since electron donating power is affected by the ionic radius of modifier ions in phosphate glasses, the parameter Ω_2 is related to the ionic radius of the modifier [63].

1.5.3.2 Effect of Number of 4f Electrons on JO Parameters

Ω_2 is independent of the number of $4f$ electrons [66], Ω_4 and $\Omega_6$decreases monotonically, in other words, they are less dependent on the numbers of $4f$ electrons. According to Dieke diagram, the energy gap between the barycenter of the $4f$ orbital and that of the $5d$ orbital increases with increasing number of $4f$ electrons of the rare-earth ions. The variation of the energy gaps with the number of the $4f$ electrons suggests that, as the number of $4f$ electrons of RE^{3+} ion increases, the degree of admixing between $4f$ and $5d$ orbitals decreases and accordingly, the magnitude of Ω_6 decreases. Moreover, the Ω_6 parameter also relates to the covalency between the rare-earth ion and oxygen ion. The Ω_6 of Pr^{3+}; Sm^{3+} Tb^{3+}; Dy^{3+}, Ho^{3+} and Tm^{3+} increase and that of Er^{3+} decreases with the redshifts of the transition. As for Nd^{3+} because two peaks are distinguished mainly in the ${}^4I_{9/2} \rightarrow {}^4F_{7/2}$ and ${}^4S_{3/2}$ transition by Stark splitting, the relative intensity ratio between these peaks are used to determine the covalency parameter of Nd^{3+} ion site [64]. For Nd^{3+} ion, the Ω_6 also show the increasing tendency with the red shift of ${}^4I_{9/2} \rightarrow {}^4F_{7/2}$ and ${}^4S_{3/2}$ transition.

1.6 McCumber Theory / Reciprocity Theorem

The theory of McCumber [46] generalizes the Einstein relations for broadband transitions, which are typical for Re^{3+}in glassy environments. The theory shows that at any frequency, the absorption, spontaneous emission, and stimulated emission spectra are related by very simple relations. These relations are obtained in the context of narrow energy widths of the individual Stark levels and thermal equilibrium between the impurity ions and the host. The McCumber relation is extremely useful in connecting the absorption and emission cross sections, especially in predicting spectral shapes of transitions that are experimentally inaccessible. According to the

above theory, when a two-sharp level system is considered, the relation between the emission and absorption cross-sections between the upper and lower levels is be given by Equation. 1.14 [67]

$$\sigma_{abs} = \sigma_{em} \tag{1.14}$$

where σ_{abs} is the absorption cross section and $\sigma_{em}$is the emission cross-section.

Einstein predicted that a two-level system might have degeneracy in its upper-level as well as lower-level, a typical situation with free ions [67]. When the above situation takes place, the ratio of the absorption and emission cross-sections is not unity anymore but is the ratio of the degeneracy of the upper-level to that of lower-level as shown below.

$$d_1\sigma_{abs} = d_2\sigma_{em} \tag{1.15}$$

where d_1 and d_2 are the degeneracies of the lower and upper levels

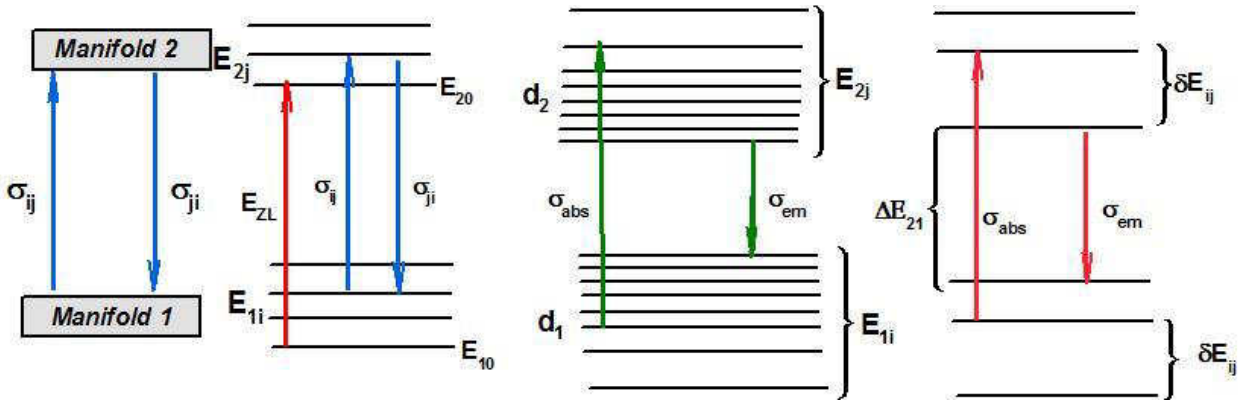

Figure 1. 11: Representation of optical transitions between two Stark manifolds in a rare-earth doped system. [50]

The above theory, called reciprocity theory, is valid only when an impurity is in free space. However, the situation is more complicated when we consider a diluted distribution of impurity ions in a medium. It is the generalization of the above situation proposed by McCumber [68] called

the *McCumber theory* that can be applied to a laser medium with a dilute distribution of impurities. The crystal field splitting removes the degeneracy of the impurity ion forming manifolds with a spread of energy levels as shown in Figure 1.11.

These levels have energies comparable to that of the thermal energy and hence, the population distribution of the levels occurs according to Boltzmann distribution. Due to this scenario, the emission from the higher level of the upper manifold is weaker than that of the lower level of the same manifold. A similar situation applies to absorption as well. The Equation (1.16) and Equation (1.17) give the absorption and emission cross sections [69].

$$\sigma_{abs} = \sum_{ij} d_i \left[\frac{Exp[-{}^{E_i}/_{k_B T}]}{Z_l} \right] \sigma_{ij}\, d_j \tag{1.16}$$

$$\sigma_{em} = \sum_{ij} d_j \left[\frac{Exp[-{}^{E_j}/_{k_B T}]}{Z_u} \right] \sigma_{ji}\, d_i \tag{1.17}$$

where Z_l and Z_u are the partition functions of the lower and upper levels and given by [70]

$$Z = \sum_{k} d_k \exp\left(-{}^{E_k}/_{k_B T}\right) \tag{1.18}$$

In above equations, *Ei* and *Ej* are the energies of the lower and upper levels respectively, *k* is the Boltzmann constant, *T* is the temperature in Kelvin, d_1, and d_2 are the degeneracy of the lower and upper levels respectively. Furthermore, $\sigma_{ij}(\nu)$ and $\sigma_{ji}(\nu)$ are the absorption and emission cross-section of the transition, respectively, between two individual Stark levels with energy E_{0i} and E_{iJ} belonging to the lower and upper manifold, respectively. The term in the square brackets in Equation (1.16) and Equation (1.17) gives the Boltzmann distribution of the population in the different levels of *d* degeneracy.

The transition between any two levels of the upper manifold and lower manifold can be considered for the derivation and the energy of any transition as shown in Equation (1.19) is given by [69]

$$E_j - E_i = h\nu - E_{zL} \tag{1.19}$$

where E_{ZL} is the zero-line energy (energy between the lowest Stark levels of the two manifolds under consideration), h is the Planks constant, and ν is the frequency of the photon emitted or absorbed. Diving Equation. (1.16) by Equation (1.17) and using Equation (1.18), we get [69]

$$\sigma_{em}(\nu) = \sigma_{abs}(\nu)\frac{Z_l}{Z_u}\, exp\left[\frac{(E_{ZL} - h\nu)}{kT}\right] \tag{1.20}$$

Using Equation. (1.18), Equation. (1.19) and Equation. (1.20) along with Equation. (1.20) [68]

$$\omega = 2\pi\nu = \frac{E_j - E_i}{\hbar} \tag{1.21}$$

where ω is the angular frequency of the radiation, and $\hbar$ is reduced Planck's constant. From the above discussion, we can derive the McCumber equation given below [68]

$$\sigma_{em}(\nu) = \sigma_{abs}(\nu) exp\left[\frac{\hbar(\mu - \omega)}{kT}\right] \tag{1.22}$$

Here, $\hbar\mu$ is the net free energy to excite one impurity from a lower Stark level to a higher Stark level, and where

$$exp\left[\frac{\hbar(\mu)}{kT}\right] = \left(\frac{N_j}{N_i}\right)_{eq} \tag{1.23}$$

Equation. (1.21) can also be written out as an equivalent to Equation. (1.24)

$$\sigma_{em}(\nu) = \sigma_{abs}(\nu) exp\left[\frac{\varepsilon - h\nu}{kT}\right] \tag{1.24}$$

which is the *exact McCumber relation* for absorption and emission cross sections at any particular frequency *v*. ε which is the temperature dependent excitation energy is calculated using the Equation. (1.23) and Equation. (1.24) shown below.

$$exp\left[-\frac{\varepsilon}{kT}\right] = \left(\frac{N_j}{N_i}\right)_{eq} \tag{1.25}$$

$$\left(\frac{N_j}{N_i}\right)_{eq} = \exp\left(\frac{\Delta E_{21}}{kT}\right)\frac{1 + \sum_{j=2}^{d2}\exp\left(-{}^{\delta E_{2j}}/_{kT}\right)}{1 + \sum_{j=2}^{d1}\exp\left(-{}^{\delta E_{1j}}/_{kT}\right)} \tag{1.26}$$

where $\Delta E_{21} = E_{21} - E_{11}$ is the energy difference between the lowest level of each manifold, and δE_{ij} is the difference of energy between the i^{th} level and the lowest level of the j^{th} manifold as shown in Figure 1.11.

To use the above equation, one needs a detailed knowledge of the complete electronic structure of the incorporated *RE* in a host. An alternate approximate method for calculating the ratio of the population of sublevels at thermal equilibrium [71]

$$\frac{N_2}{N_1} = \exp\left(\frac{-\Delta E_{21}}{kT}\right)\frac{1 - \exp\left(-{}^{\delta E_1}/_{kT}\right)1 - \exp\left(-{}^{d_j\delta E_2}/_{kT}\right)}{1 - \exp\left(-{}^{\delta E_2}/_{kT}\right)1 - \exp\left(-{}^{d_i\delta E_1}/_{kT}\right)} \tag{1.27}$$

All the parameters of the above equation were explained before. In this approach, we made two approximations were made

- the sublevels are equally spaced in energy such that $E_{ij} = (j-1)E_i$ and
- δE_1 and δE_2 are a low energy and high energy half widths respectively, of the emission spectrum or the absorption spectrum measured at room temperature. The number of manifolds in one level is $J + 1/2$ [72]

These approximations reduce the number of necessary parameters needed for McCumber calculation. Hence, the choice of either exact or approximate McCumber theory depends on the trade-off between accuracy and the knowledge of energy level splitting in the host. The McCumber theory derived here is valid only under certain assumptions, which if violated would result in massive distortions of the estimated CS values. The following assumptions are critical in calculating the CS values using McCumber theory to obtain reasonable accuracy [71]:

- The lifetime of the manifold is longer than that of the time taken to achieve thermal equilibrium in each manifold.
- The spectral width of every level is small when compared to thermal distribution, kT.

The first assumption is satisfied most of the time, but the second assumption needs to be carefully verified. The second assumption breaks at temperatures above room temperature, due to the effect of broadening phenomena on the transitions.

References

[1] J. E. Shelby, Introduction to Glass Science, Cambridge: The Royal Society of Chemistry, 2005.

[2] A. C. Wright, "The Structure of Amorphous Solids by X-Rays and Neutron Diffraction," *Advances in Structure Research by Diffraction Methods,* pp. 1-84, 1974.

[3] E. T. LEE, "Development and Characterization of Phosphate glass for Athermalization," Southhampton, 2004.

[4] E. Lippmaa, M. Maegi, A. Samoson, G. Engelhardt and A. R. Grimmer, "Structural Studies of silicate by solid-state high-resolution Silicon-29 NMR," *Journal of American Chemical Society,* vol. 102, no. 15, pp. 4889-4893, 1980.

[5] R. K. Brow, "Review: The Structure of Simple Phosphate Glasses," *Journal of Non-Crystalline Solids,* vol. 263 & 264, pp. 1-28, 2000.

[6] J. V. Wazer, Phosphorus and its compounds, vol. 1, Interscience Publishers, 1958.

[7] U. Hoppe, "A Structural Model for Phosphate Glasses," *Journal of Non-Crystalline Solids,* vol. 195, pp. 138-147, 1996.

[8] R. K. Brow, R. J. Kirkpatrick, and G. L. Turner, "The short-range structure of sodium phosphate glasses I. MAS NMR studies," *Journal of Non-Crystalline Solids,* vol. 116, pp. 39-45, 1990.

[9] R. K. Brow and D. R. Tallant, "Structural Design of Sealing Glasses," *Journal of Non-Crystalline Solids,* vol. 222, pp. 396-406, 1997.

[10] J. Bunker, G. Arnold, and J. Wilder, "Phosphate Glass dissolution in aqueous solution," *Journal of Non-Crystalline Solids,* vol. 64, no. 3, pp. 291-316, 1984.

[11] M. Weber, "Science and Technology of Laser Glasses," *Journal of Non-Crystalline Solids,* vol. 123, no. 13, pp. 208-222, 1990.

[12] J. A. Wilder Jr, "Glasses and Glass Ceramics for Sealing to Aluminum Alloy," *Journal of Non-Crystalline Solids,* vol. 123, no. 2, pp. 879-884, 1980.

[13] R. K. Brow, L. Kovacic, and R. Loehman, "Novel Glass Sealing Technologies," *Ceramic Transactions,* vol. 70, pp. 177-187, 1996.

[14] K. Kawamura, H. Hosono, H. Kawazoe, N. Matsunami and Y. Abe, "Large enhancement of electrical conductivity in Magnesium phosphate glasses by ion implantation of the proton," *Journal of the Ceramic Society of Japan,* vol. 104, no. 1211, pp. 688-690, 1996.

[15] P. Quinn and J. Schoenau, "Effects of conventional and controlled release phosphorus fertilizer on crop emergence and growth under controlled environment conditions," *Journal of Plant Nutrition,* vol. 33, no. 9, pp. 1253-1263, 2010.

[16] K. G. Karapetyan, V. A. Senichenkov, G. S. Zenin and M. N. Ryabova, "Kinetics of dissolution of glassy Fertilizers," *Russian Journal of Applied Chemistry,* vol. 78, no. 9, pp. 1383-1385, 2005.

[17] J. C. Knowles, "Phosphate Based glasses for biomedical applications," *Journal of Material Chemistry,* vol. 13, pp. 2395-2401, 2003.

[18] V. Valappil, D. M. Pickup, D. L. Carroll, C. K. Hope, J. Pratten, R. J. Newport, M. E. Smith, M. Wilson and J. C. Knowles, "Effect of Silver contents on the structure and antibacterial activity of silver-doped phosphate based glasses," *Antimicrobial Agents and Chemotherapy,* vol. 51, pp. 4453-4461, 2007.

[19] T. Gilchrist, D. Healy and C. Drake, "Controlled silver-releasing polymers and their potential for urinary tract infection control," *Biomaterials,* vol. 12, p. 7678, 1991.

[20] D. Ravaine, "Ionic Transport Properties in Glasses," *Journal of Non-Crystalline Solids,* vol. 73, no. 13, pp. 287-303, 1985.

[21] A. Marino, S. Arrasmith, L. Gregg, S. Jacobs, G. Chen, and Y. Duc, "Durable phosphate glasses with lower transition temperature," *Journal of Non-Crystalline Solids,* vol. 289, no. 13, pp. 37-41, 2001.

[22] N. Peyghambarian and A. Schulzgen, "Fiber Lasers: High Power devices in compact packages," *Opt Photon News,* vol. 16, pp. 36-41, 2005.

[23] F. Wedgwood and A. Wright, "Short Range antiferromagnetic ordering in Vitreous Fe2O3-P2O5," *Journal of Non-Crystalline Solids,* vol. 21, no. 1, pp. 95-105, 1976.

[24] J. L. Shaw, A. C. Wright, R. N. Sinclair, G. K. Marasinghe, D. Holland, M. R. Lees and C. R. Scales, "Spin-glass-like antiferromagnetic interactions in iron phosphate glasses," *Journal of Non-Crystalline Solids,* vol. 345 & 346, pp. 245-250, 2004.

[25] H. Akamatsu, K. Fujita, S. Murai and K. Tanaka, "Magneto-optical properties of transparent divalent iron phosphate glasses," *Applied Physics Letters,* vol. 92, no. 25, 2008.

[26] L. Abbas, L. Bih, A. Nadiri, Y. E. Amraoui, D. Mezzane and B. elouadi, "Properties of Mixed LiO2 and Na2O Molybdenum Phosphate glasses," *Journal of Molecular Structure,* vol. 876, no. 13, pp. 194-198, 2008.

[27] R. Rogojan, P. E. Sterian, and M. Elisa, "Transmission and absorption spectra of Aluminophosphate doped glasses with rare-Earth ions," *Proc SPIE,* vol. 3416, pp. 245-251, 1998.

[28] R. Waesche and R. Bruckner, "Tg, UV-transparency and mixed oxide effect of Ulta-pure ternary alkaline earth metaphosphate glasses," *Journal of Non-Crystalline Solids,* vol. 107, no. 23, pp. 309-315, 1989.

[29] D. Ehrt and W. Seeber, "Glass for High-performance optics and laser technology," *Journal of Non-Crystalline Solids,* vol. 129, no. 13, pp. 19-30, 1991.

[30] R. K. Brow and D. E. Day, "Ammonia-Treated phosphate glasses useful for sealing to metals." US Patent 5045508, Jan 1991.

[31] B. Sales and L. Boatner, "Lead Phosphate glass as a stable medium for the immobilization and disposal of high-level nuclear Waste," *Materials Letters,* vol. 2, no. 4, pp. 301-304, 1984.

[32] D. E. Day, Z. Wu, C. S. Ray, and P. Hrma, "Chemical durable iron phosphate glass waste forms," *Journal of Non-Crystalline Solids,* vol. 241, no. 1, pp. 1-12, 1998.

[33] C. W. Kim and D. E. Day, "Immobilization of Hanford Law in iron phosphate glasses," *Journal of Non-Crystalline Solids,* vol. 331, no. 1, pp. 20-31, 2003.

[34] W. Huang, D. E. Day, C. S. Ray, C. W. Kim and A. Mogus-Milankovic, "Vitrification of high chrome oxide nuclear waste in iron phosphate glasses," *Journal of Non-Crystalline Solids,* vol. 327, no. 1, pp. 46-57, 2004.

[35] L. N. Ma, "Dissolution behavior of Phosphate Glasses," Missouri University of Science and Technology, Missouri, 2014.

[36] C. W. Kim, C. S. Ray, D. Zhu, D. E. Day, D. Gombert, A. Aloy, A. Mogus-Milankovic and M. Karabulut, "Chemcialdurable iron phosphate glasses for vitrifying sodium-bearing waste (SBW) using conventional and cold crucible induction melting (CCIM) techniques," *Journal of Nuclear Materials,* vol. 322, no. 2, pp. 152-164, 2003.

[37] W. H. Zachariasen, "The atomic arrangement in glasses," *Journal of American Chemical Society,* vol. 54, no. 10, pp. 3841 - 3851, 1932.

[38] C. Dayanand, G. Bhikshamaiah, V. J. Tyagaraju and M. Salagram, "Review: Structural investigations of phosphate glasses: a detailed infrared study of the x(PbO)-(1-x)P2O5 vitreous system," *Journal of Material Science,* vol. 31, pp. 1945 - 1967, 1996.

[39] Y. M. Moustafa and K. El-Egili, "Infrared spectra of sodium phosphate glasses," *Journal of Non-Crystalline Solids,* vol. 240, pp. 144-153, 1998.

[40] G. J. Exarhos, P. j. Miller and W. M. Risen Jr, "Interionic vibrations and glass transitions in ionic oxide metaphosphate glasses," *Journal of Chemical Physics,* vol. 60, no. 11, pp. 4145 - 4155, 1974.

[41] B. N. Nelson and G. J. Exarhous, "Vibrational spectroscopy of cation site interaction in phosphate glasses," *Journal of chemical physics,* vol. 71, no. 7, pp. 2739 - 2747, 1979.

[42] B. Bridge and N. D. Patel, "Composition dependence of the infrared absorption spectra of molybdenum phosphate glasses and some crystalline," *Journal of Non-Crystalline Solids,* vol. 91, no. 1, pp. 27-42, 1987.

[43] Y. M. Moustafa, H. Doweidar, and G. El-Damrawi, "Utilisation of infrared spectroscopy to determine the fraction of the four coordinated borons in borate glasses," *Physics and chemistry of glasses,* vol. 35, no. 2, pp. 104-106, 1994.

[44] A. Efimov, Optical constants of inorganic glasses, Laser, optical science and technology, Taylor & Francis, 1995.

[45] D. E. Corbridge, The infrared spectra of phosphorus compounds, New York: Eds Interscience, 1969.

[46] A. N. Lazarev, Vibrational spectra, and structure of silicate glasses, New York consultant Bureau, 1952.

[47] A. A. Higazy and B. Bridge, "Infrared spectra of vitreous system Co3O4-P2O5 and their interpretation," *Journal of Material Science,* vol. 20, no. 7, pp. 2345 - 2358, 1985.

[48] G. b. Rouse, P. J. Miller, and W. m. Risen Jr, "Mixed Alkali Glass spectra and structure," *Journal of Non-Crystalline Solids,* vol. 28, pp. 193-207, 1978.

[49] H. Ebendroff-Heidepriem and D. Ehrt, "Optical spectroscopy of rare-earth ions in glasses," *Glastech Ber. Glass Sci Technol,* vol. 71, no. 10, pp. 289-299, 1998.

[50] L. Agazzi, "Spectroscopic Excitation and quenching processes in rare-earth ion doped Al2O3 and their impact on amplifier and laser performance," 2012.

[51] G. H. Dieke, Spectra and Energy Levels of Lanthanide Ions in Crystals, New York: John Wiley, 1968.

[52] W. T. Carnall, P. R. Fields, and K. Rahnak, "Electronic energy levels in the Trivalent Lanthanide Aqua ions 1. Pr3+,Nd3+,Pm3+,Sm3+,Dy3+,Ho3+,Er3+ and Tm3+," *Journal of Chemical Physics,* vol. 49, pp. 4424-4442, 1968.

[53] W. T. Carnall, G. L. Goodman, K. Rajnak and R. S. Rana, "A systematic analysis of the spectra of the lanthanides doped into single crystal LaF3 ," *Journal of Chemical Physics,* vol. 90, pp. 3443-63, 1989.

[54] B. M. Walsh, "Advances in spectroscopy for lasers and sensing," in *Judd-Ofelt theory: Principles and Practices*, Netherlands, Springer, 2006, pp. 403-433.

[55] W. J. Miniscalco, "Optical and electronic properties of rare-earth ions in glasses," in *Rare-Earth doped fiber lasers and amplifiers*, New York, Marcel Dekker, 1993.

[56] L. J. Nugent, R. D. Baybarz, J. L. Burnett and J. L. Ryan, "Electron-transfer and f → d absorption bands of some lanthanide and actinide complexes and the standard (III–IV) oxidation potentials for each member of the lanthanide and actinide series," *Journal of Inorganic and Nuclear Chemistry,* vol. 33, no. 8, pp. 2503-2530, 1971.

[57] L. J. Nugent, R. D. Baybarz, J. L. Burnett and J. L. Ryan, "Electron-transfer and f-d absorption bands of some lanthanide and actinide complexes and the standard (II-III) oxidation potential for each member of the lanthanide and actinide series," *Journal of Physical Chemistry,* vol. 77, no. 12, pp. 1528-1539, 1973.

[58] B. R. Judd, "Optical absorption intensities of rare-earth ions," *Phys Rev,* vol. 127, pp. 750-761, 1962.

[59] G. S. Ofelt, "Intensities of crystal spectra of rare-earth ions," *The Journal of Chemical Physics,* vol. 37, no. 2, pp. 511-520, 1962.

[60] E. Desurvire, Erbium-Doped fiber amplifiers: Principles and Applications, New York: John Wiley and Sons, 1994.

[61] M. P. Hehlen, M. G. Brik, and K. W. Kramer, "50th anniversary of the judd-ofelt Theory: An experimentalist's view of the formalism and its application," *Journal of Luminescence,* vol. 136, pp. 221-239, 2013.

[62] A. A. Kaminskii, Crystalline Laser: Physical Processes and Operating Schemes, New York: CRC Press, 1996.

[63] H. Ebendorff- Heidepriem, W. Seeber and D. Ehrt, "Spectroscopic properties of Nd3+ ions in phosphate glasses," *Journal of Non-Crystalline Solids,* vol. 183, pp. 191-200, 1995.

[64] Y. Nageno, H. Takebe, and K. Morinaga, "Correlation between radiative transition probabilities of nd3+ and composition in silicate, borate, and phosphate glasses," *Journal of American Ceramic Society,* vol. 76, no. 12, pp. 3081 - 3086, 1993.

[65] H. Takebe, Y. Nageno and K. Morinaga, "Effect of network modifier on spontaneous emission probabilities of Er3+ in oxide glasses," *Journal of American Ceramic Society,* vol. 77, no. 8, pp. 2132 - 2136, 1994.

[66] H. Takebe, Y. Nageno and K. Morinaga, "Compositional dependence of Judd-ofelt parameters in Silicate, borate and phosphate glasses," *Journal of American Ceramic Society,* vol. 78, no. 5, pp. 1161 - 1168, 1995.

[67] R. M. Martin, "“Reciprocity between Emission and Absorption for Rare Earth Ions in the glass," Worcester, 1993.

[68] D. E. McCumber, "Einstein relations connecting emission and absorption spectra," *Phys Rev,* vol. 136, no. 4A, p. 954, 1964.

[69] S. A. Payne, L. L. Chase, L. K. Smith, W. L. Kway and W. L. Krupke, " Infrared Cross section measurements for crystals doped with Er3+, Tm3+, and Ho3+," *IEEE Journal of Quantum Electronics,* vol. 28, no. 11, 1992.

[70] S. A. Payne, L. L. Chase, H. W. Newkirk, L. k. Smith and W. F. Krupke, "LiCaALF6: Cr3+: A promising new solid-state laser material," *IEEE Journal of Quantum Electronics,* vol. 24, no. 11, p. 2243, 1988.

[71] R. A. Martin and R. S. Quimby, "Experimental evidence of the validity of the McCumber theory relating emission and absorption for rare-earth Glasses," *Journal of Optical Society of America B,* vol. 23, no. 9, p. 1770, 2006.

[72] G. C. Righini and M. Ferrari, "Photoluminescence of Rare-earth doped glasses," *Rivista Del Nuovo Cimento,* vol. 28, no. 12, pp. 1-53, 2005.

CHAPTER 2

SCATTERING THEORY

2.1 Introduction

Scattering is one several ways in which X-ray interact with matter. In the classical description of the scattering event, the electric field of the incident X-rays exerts a force on the electron which then accelerates and radiates the scattered wave. Classically, the wavelength of the scattered wave is same as that of the incident one. This scattering is called elastic scattering. In quantum mechanical treatments, where the incident X-ray photon has a momentum $\hbar\vec{k}$ and energy $\hbar\omega$, energy may be transferred to the electron a way that the scattered photon has a lower frequency than the incident one. This inelastic scattering process is called the Compton Effect. However, the elastic scattering in X-rays is the primary process that is exploited in the investigation of the structure of materials. It can be shown that this description is valid for electrons bound to the atom where the energy of the incident beam is far from the absorption edges of the material [1]. The momentum transfer of a photon in a scattering event is

$$\vec{Q} = \vec{k'} - \vec{k} \qquad (2.1)$$

where $\vec{k}$ and $\overrightarrow{k'}$ are the wavevectors of the incident and scattered wave, respectively. The quantity $\vec{Q}$ is known as the scattering vector/diffraction vector (momentum transfer). The vector relationship between $\vec{Q}, \vec{k}$ and $\overrightarrow{k'}$ can be displayed pictorially with the help of scattering triangle as in figure 2.1 [2].

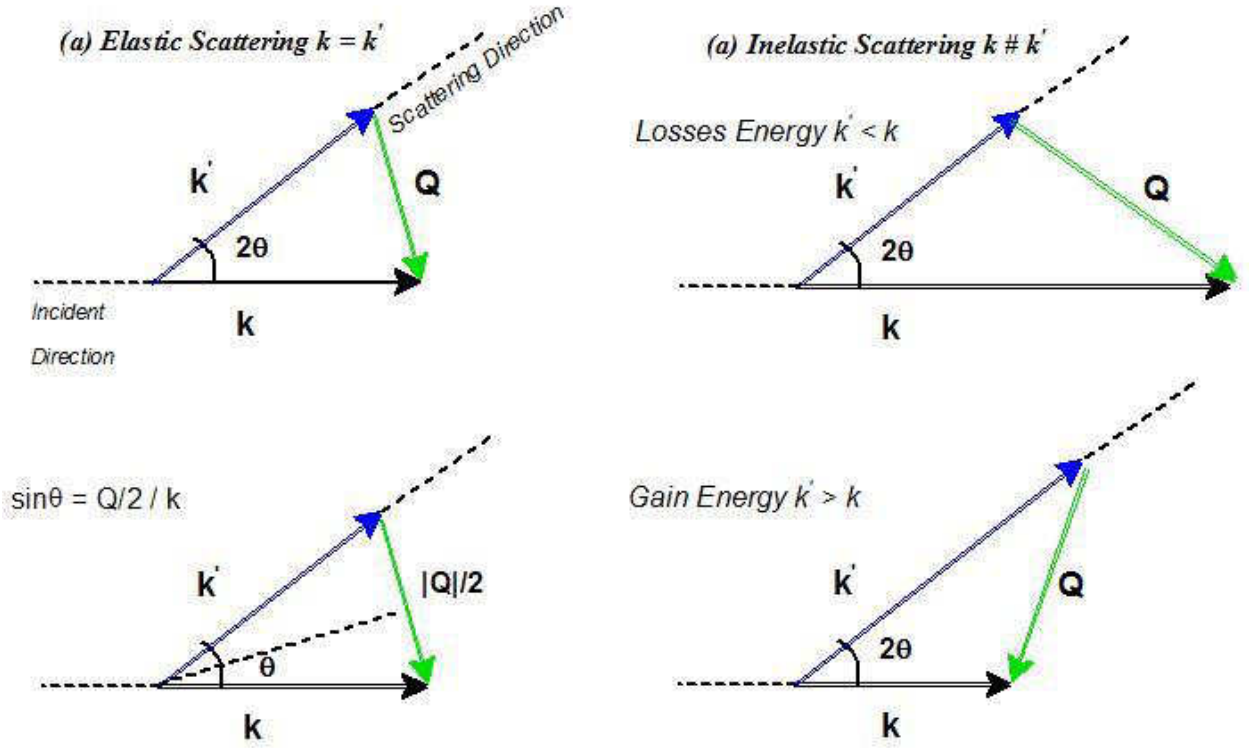

Figure 2. 1: Scattering triangle for both elastic and inelastic scattering events. [2]

The scattering triangle also emphasizes that the magnitude and direction of $\vec{Q}$ is determined by the magnitude and directions of incident and scattered vectors and the angle of 2θ through which the X-rays or neutrons is deflected during the scattering process. Generally, 2θ is referred as scattering angle. For elastic scattering, (Figure 2.1 a) $k = k'$, the magnitude of diffraction vector is given by

$$\left|\vec{Q}\right| = \frac{4\pi}{\lambda} sin\theta \qquad (2.2)$$

where λ is the wavelength of the scattered photon/neutron and $\theta = \ \theta/2$. In the case of powder measurements, the only relevant quantity is the magnitude of the diffraction vector $\left|\vec{Q}\right|$. Because $sin\theta \ \leq 1$, the experimentally accessible range of Q is limited to less than $4\pi/\lambda$ [3].

This chapter discusses the theoretical background of X-ray diffraction by glasses and the relation of the theory to the experimentally obtained interference function. The real space correlation can be obtained from the Fourier inversion of the interference function and can be used to determine structural information, such as bond distance and coordination numbers. Furthermore, a review of rare-earth doped phosphate glasses and role of different modifiers in phosphate glasses such as aluminum and water is presented.

2.2 The Scattering Cross-Section

An important concept in scattering experiment is the scattering cross-section. Imagine an experiment in which a monochromatic beam of neutron or X-rays (hereafter generally referred as probes) are incident upon a sample containing *N* atoms. The total scattering cross-section is defined as

$$\sigma = {}^{N_s}/_{N\,\Phi} \qquad (2.3)$$

Where Φ is the incident probe flux and N_s is the number of probes scattered per unit time. The differential scattering cross-section, which is the quantity measured in a diffraction experiment, is given by

$$\frac{d\sigma}{d\Omega} = \frac{N_s'}{N\,\Phi d\Omega} \qquad (2.4)$$

where N_s' is the number of probes scattered per unit time into the solid angle $d\Omega$. Figure 2.2 represent the scattering process and applies to any scattering probe.

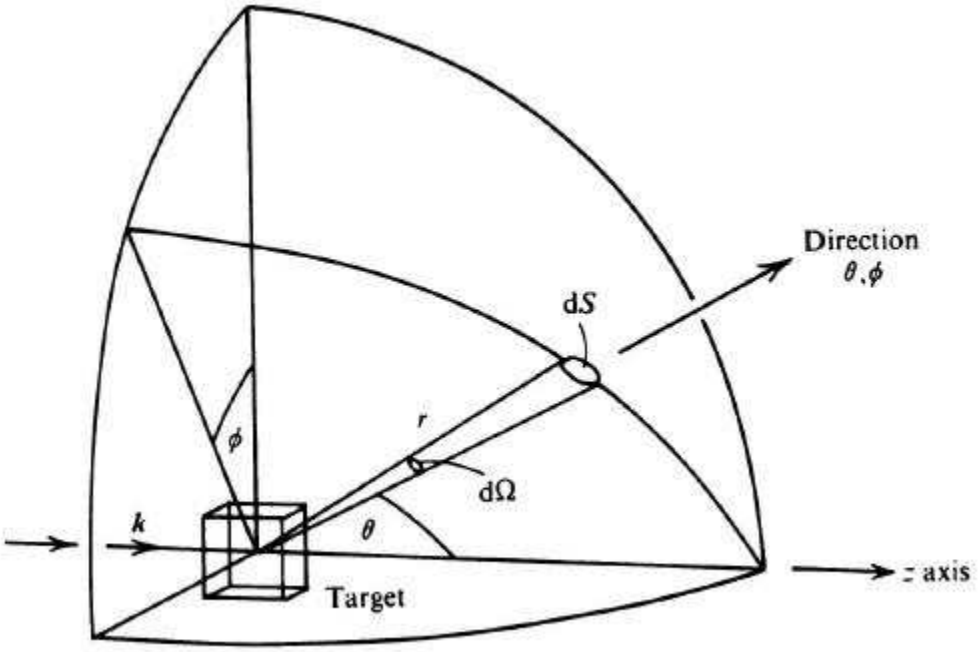

Figure 2. 2: Geometric representation of a diffraction experiment. Note that $\boldsymbol{ds = r^2 d\Omega}$ *and k represents the direction of the incident probe. [4]*

2.3 Scattering: General

The formal derivation of the theory of diffraction by amorphous materials can be attributed toVan Hove [5] [4] correlation function, and such a derivation is presented by Wright et al. [6] [7] [8] [9] [10]. The following theory is based on the simpler derivation by Urnes [11].

In a scattering experiment, a scattering probe of wavevector, $\vec{k}_i$ and energy E_i is incident on a sample and is scattered through an angle 2θ, resulting in a scattered wavevector probe of $\vec{k}_f$ and energy E_f, such that each scattering event is characterized by an energy transfer

$$\hbar\omega = E_i - E_f \tag{2.5}$$

and a momentum transfer

$$\hbar\vec{Q} = \hbar\vec{k}_i - \hbar\vec{k}_f \tag{2.6}$$

Here $\hbar\omega$ and $\hbar\vec{Q}$ is the energy and momentum transferred to the sample, respectively. To determine the structure of a sample, only the value of $\vec{Q}$ is needed, when scattering is elastic (i.e. $\hbar\omega = 0$). In this case the, probe wavelength, remains unchanged and the magnitude of $|\vec{Q}|$ is given by Equation 2.7

$$|\vec{Q}| = Q = \frac{4\pi}{\lambda} sin\theta \tag{2.7}$$

In reality, a detector at a fixed scattering angle 2θ, records both elastic and inelastic contribution. The total intensity I_T of the scattered probe is in fact given by [3]

$$I_T = I_c + I_{IC} + I_{MC} + I_{BG} \tag{2.8}$$

where I_c is the coherent scattering intensity, I_{IC} is the incoherent intensity, I_{MC} the multiple-scattering intensity, and I_{BG} the background intensity. It can be used to perform the integration over ω at a constant angle. The inelastically scattered probe can be used to gain information about the dynamics of the sample. The information on the structure and lattice dynamics are contained in the coherent scattering cross-section ($\frac{d\sigma_c}{d\Omega}$). The relationship of coherent scattering cross-section with the experimentally obtained coherent scattering I_c is given by the Equation 2.9

$$I_c = APC \frac{d\sigma_c}{d\Omega} \tag{2.9}$$

Where *A* is the absorption factor which depends on the geometry of the sample and nature of scattering particles, *C* is the normalization factor, and *P* is the electric polarization factor [1].

2.4 Scattering by a Group of Atoms

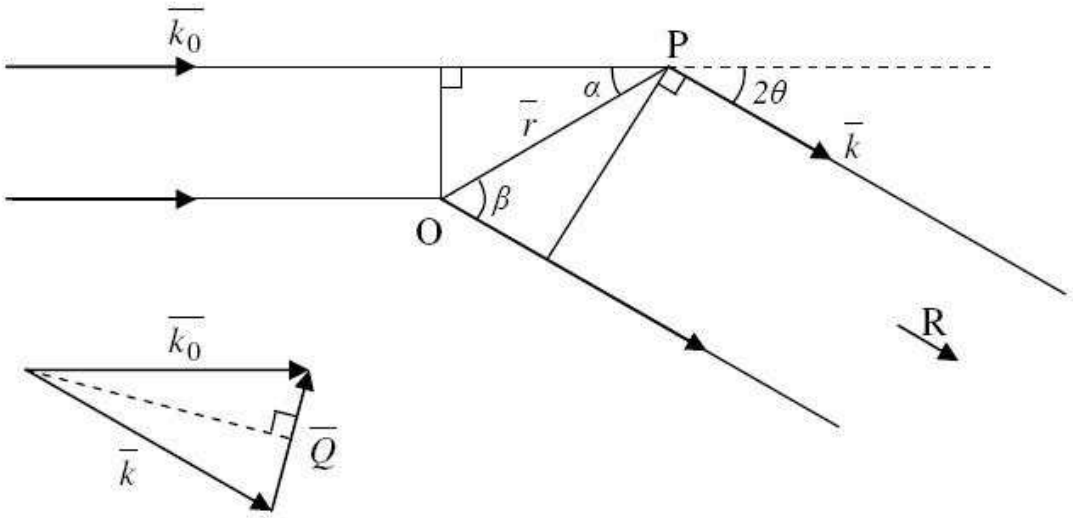

Figure 2. 3: Scattering of a probe by a sample through and angle $\boldsymbol{2\theta}$*.*

Figure 2.3 depicts a situation where there is an atom at P a vector distance $\vec{r}$ away from the arbitrary origin O. A detector is placed at some distance$R$, such that $R \gg r$. The phase at R, of a wave scattered at P relative to one scattered at O, is

$$\Phi = \frac{2\pi\,(r\,cos\alpha - r\,cos\beta)}{\lambda} \tag{2.10}$$

By substituting $\vec{r}\,.\vec{k}_i = \frac{2\pi}{\lambda}\,rcos\alpha$ and $\vec{r}\,.\vec{k}_f = \frac{2\pi}{\lambda}\,rcos\beta$, the phase difference can be expressed as

$$\Phi = \vec{r}\,.\left(\vec{k}_i - \vec{k}_f\right) = \vec{r}\,.\vec{Q} \tag{2.11}$$

And the amplitude $A_i(Q)$ of the scattered wave from this single atom can be given as

$$A_i(Q) = a(Q)Exp(\imath\,\vec{r}\;.\vec{Q}\,) \tag{2.12}$$

In Equation 2.8, $a(Q)$ represents X-ray form factor, $f(Q)$. When the scattering takes place from a system of N atoms, the amplitudes need to be summed over all the atoms, taking into account the relative phases as in Equation 2.13

$$A_N(Q) = \sum_{n=1}^{N} a_n(Q) Exp(\imath\, \vec{r}_n \ . \vec{Q}\ ) \tag{2.13}$$

The scattering intensity is obtained by multiplying $A_N(Q)$ by its complex conjugate [12]

$$I_N(Q) = \ A_N(Q)\ A_N^*(Q) = \sum_{p=1}^{N}\sum_{q}^{N} a_p(Q)\, a_q(Q) Exp(\imath\, \vec{r}_{pq}\ . \vec{Q}\ ) \tag{2.14}$$

where p and q are any two individual atoms regardless of type. It should be noted that the summation over p and q are taken over all atoms in the sample and that $I_N(Q)$ depends on the interatomic distance vector $\vec{r}_{pq} = \vec{r}_p - \vec{r}_q$and is independent of the arbitrary origin. Equation (2.14) is universal for crystal, amorphous solids, liquids, and gases because no assumptions have been made about the atomic arrangement in the sample.

2.5 Scattering by an Isotropic Samples

A sample described as isotropic has no preferred orientation such that, for any given interatomic vector $\vec{r}_{pq}$, there will be other equivalent vectors in the sample in all possible directions with respect to $\vec{Q}$. This allows the vector formalism to be relaxed and Equation (2.14) can be rewritten as an average over all directions [12]

$$I_N(Q) = \sum_{p} \overline{a_p^2(Q)} + \sum_{p}\sum_{p\neq q} \overline{a_p(Q)a_q(Q)}\ \frac{\sin(r_{pq}Q)}{r_{pq}Q} \tag{2.15}$$

Equation 2.15 is known as the Debye equation and can be used to calculate the scattered intensity provided that all the interatomic distances be known or can be calculated. In an amorphous material, the interatomic vectors are unknown, and it becomes necessary to look at the atomic correlation in real space to make sense of the structure.

2.6 Radial Distribution Function

The atomic arrangement is related to the radial density function $\rho(r)$, which describes how the number density fluctuates as a function of radial distance from an atom at an arbitrary origin. It should be noted that $\rho(r)$ is the average over all atoms in the sample taken as the center. Equation (2.16) defines $\rho(r)$ for a sample of N atoms

$$\rho(r) = \frac{\sum_n^N \rho_n(r)}{N} \tag{2.16}$$

Where $\rho_n(r)$ is the radial density distribution around the nth atom. The total correlation function is defined as

$$t(r) = 4\,\pi\, r\, \rho(r) \tag{2.17}$$

Moreover, the differential correlation functions $\rho(r)$, is obtained by subtracting the average density term from $t(r)$

$$d(r) = 4\pi\, r[\rho(r) - \rho_0] \tag{2.18}$$

where ρ_0 is the average number density of the bulk sample. It is useful to recognize that for a sample containing m different atom types, $t(r)$, and hence $d(r)$, can be represented as the sum of $\frac{m(m+1)}{2}$ independent component correlations.

$$t(r) = \sum_i \sum_j t_{ij}(r) = \sum_i \sum_j 4\pi r \rho_{ij}(r) \tag{2.19}$$

Equation (2.19) defines the distribution of atom type j about the i^{th} atom in one compositional unit of the sample. A composition unit contains a number of atoms of each kind in proportion to the composition of the sample. It is typical to normalize the number of atoms per compositional unit to unity. A diffraction experiment measures a combination of correlations, but the weighting given to each correlation depends on the probe being used. It is possible to rewrite Equation (2.15) in terms of $t_{ij}(r)$ as

$$I(Q) = \sum_p \overline{a_p^2(Q)} + \sum_p \sum_{p \neq q} \overline{a_p(Q) a_q(Q)} \int_0^\infty t_{pq}(r) \frac{\sin(r_{pq} Q)}{r_{pq} Q} \, dr \tag{2.20}$$

where $I(Q)$ is the scattering intensity per compositional unit. The second term on the right-hand side of Equation (2.20) can be broken into two further terms, the first involving $d_{pq}(r)$ and the second involving ρ_0 as in Equation (2.21).

$$\begin{aligned} I(Q) = \sum_p \overline{a_p^2(Q)} + \sum_p \sum_{p \neq q} \overline{a_p(Q) a_q(Q)} \int_0^\infty d_{pq}(r) \frac{\sin(rQ)}{Q} \, dr \\ + \int_0^\infty 4\pi r \rho_0 \left[\sum_i \overline{a_i(Q)} \right]^2 \frac{\sin(Qr)}{Q} \, dr \end{aligned} \tag{2.21}$$

The 3rd term on the right-hand side of Equation (2.21) usually called $I_0(Q)$, becomes a $\delta-$ function at $Q = 0$ for a sample of infinite extent. It is assumed that the contribution of the 3rd term is condensed into unscattered the primary beam and is, therefore, not recorded. It should be noted that $I(Q)$ is equivalent to the measured quantity $d\sigma/d\Omega$ define earlier.

The part of $I(Q)$ that is of interest is called the interference function $i(Q)$ and is defined as

$$Q\ i(Q) = Q[I(Q) - \sum_p \overline{a_p^2(Q)} - I_0(Q)]$$
$$= \sum_p \sum_{p \neq q} \overline{a_p(Q) a_q(Q)} \int_0^\infty d_{pq}(r) \sin(r\ Q)\ dr \quad (2.22)$$

From Equation 2.22 it can be seen that $Q\ i(Q)$ is the weighted sum of the sin Fourier transform of $d_{pq}(r)$, with $\overline{a_p(Q)}$ and $\overline{a_q(Q)}$ being the weighting factor.

2.7 Experimental Real Space Correlation Function

It is necessary to use a Fourier transformation to extract the real space correlation function from the experimentally obtained interference function. Theoretically, the experimental differential correlation function $D(r)$, is the sine Fourier transform of $Q\ i(Q)$ with $i(Q) = S(Q) - 1$. This would be the case if data could be collected from zero up to an infinite extent in Q. In this case, it would follow that $D(r)$ is the sum over all atom pairs of the component differential correlation function $d_{ij}(r)$. Experimentally, data cannot be collected over an infinite extent in Q and the relationship between $D(r)$, and $d_{ij}(r)$ is not straight forward, and the Fourier transform requires the use of modification function $M(Q)$ [13]

$$D(Q) = \frac{2}{\pi} \int_0^\infty Q\ i(Q) M(Q) \sin(Qr) dQ \quad (2.23)$$

The form of $M(Q)$ is discussed later, but it is important to note that $M(Q) = 0$ for $Q > Q_{max}$. The total experimental correlation function $T(r)$, can be developed from $D(r)$ with the addition of the so-called average density term $T^0(r)$, which is the Fourier transform of $QI_0(Q)$

$$T(r) = D(r) + T^0(r) = \sum_i \sum_j t_{ij}^*(r) \quad (2.24)$$

The asterisk $(*)$ in Equation 2.24 is used to identify a component that is probe dependent. Equation 2.24 defines $T(r)$ as being a sum of $t_{ij}^{*}(r)$, which is not the same as $t_{ij}(r)$ defined in Equation 2.19. However, convolution relates these two functions as shown in Equation 2.25

$$t_{ij}^{*}(r) = \int_{0}^{\infty} t_{ij}(r')\big[\, P_{ij}(r-r') - \, P_{ij}(r+r')\big]dr' \qquad (2.25)$$

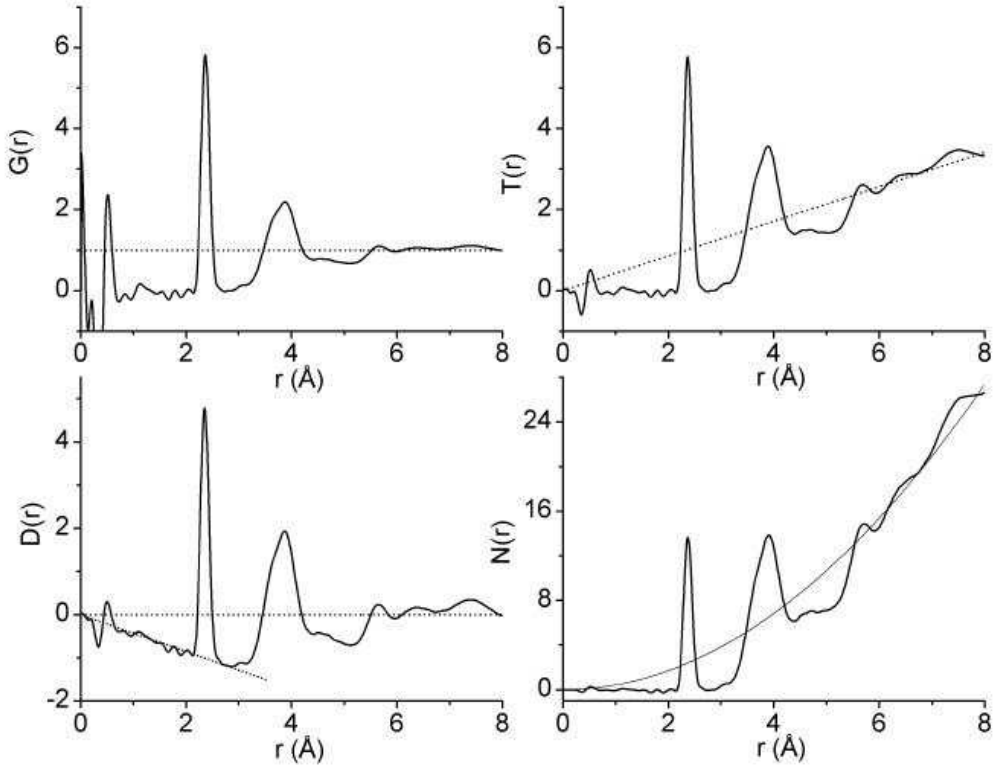

Figure 2. 4: Different representation of the X-ray PDF for $GeSe_2$ glass; $G(r)$ oscillating about unity at high-r and zero at low-r , $T(r)$ oscillating about zero at low-r and $4\pi\rho r$ at high-r , $D(r)$ oscillating about $-4\pi\rho r$ at low-r and zero at high-r , $N(r)$ oscillating about zero at low-r and $4\pi\rho r^2$ at high-r. [16]

There are many different formalisms for the total structure factor $S_X(Q)$. These have been summarized by Keen [14]. Other commonly used real space representation [15] include the total

pair distribution function $T_x(r)$, which is useful for peak fitting for glassy spectra. The differential pair distribution function, $D(r)$, which removes the bulk density emphasizes the longer r correlation, and also the radial distribution function $N_X(r)$ has a direct physical interpretation as the number of atoms that are present within range r and $r + dr$. All these different representations of X-ray pair distribution function are shown in Figure 2.4 for $a\ GeSe_2$ glass [16].

2.8 Application to X-ray Diffraction

The quantity that defines the strength of X-ray scattering is the atomic form factor or scattering factor $f(Q)$. $f(Q)$ exhibits resonance behavior for energies near an absorption edge. This is due to anomalous dispersion, which not only affects the magnitude of the collision photon but also imparts a phase shift, described by a complex component of $f(Q)$. X-ray diffraction experiments tend to be conducted at energies sufficiently away from the absorption edges, and the contribution of a complex component of $f(Q)$ becomes very small. In X-ray diffraction, the scattering process is between the interacting X-rays and the electrons in the atom. The absorption of the incident X-ray photon result in excitation of the electronic system followed immediately by the relaxation and re-emission of an X-ray photon. Since the atomic diameter is comparable to the X-ray wavelength, it is necessary to consider intra-atomic interference effects, which account for the Q dependence of atomic form factor. The form of $f(Q)$ for most elements have been calculated and modeled as the sum of four Gaussians plus a constant. The atomic scattering factors can be reconstructed using the nine parameters in equation 2.26

$$f(Q) = \sum_{i=1}^{4} a_i e^{-b_i s^2} + c \qquad (2.26)$$

where a_i, b_i and c are tabulated (see the International Tables of Crystallography and $s = Q/4\pi$. Where possible the parameters for ionic species were used rather than neutral atoms because electrons involved in bonding are shifted away from their parent atom effectively creating ionic states and the atoms can no longer be described as isolated. The X-ray differential scattering cross-section can then be defined as per Equation 2.21, with the atomic scattering factors assuming the role of $a(Q)$

$$\frac{d\sigma}{d\Omega} = I(Q) = i(Q) + \overline{f^2(Q)} \tag{2.27}$$

Since the scattering is due to the electron cloud around each atom, the direct sine Fourier transform of the X-ray $i(Q)$ (as in Equation 2.23) yields the electronic correlation function. This suffers from poor real space resolution because the electron clouds have a significant size compared to the X-ray wavelength. It is convenient to divide the X-ray $i(Q)$ by the averaging scattering factor per atom squared, $f_e^2(Q)$, sometimes referred to as the sharping function. This has the effect of collapsing the scattering to that expected of a point scatterer, with $f_e(Q)$ having the form

$$f_e(Q) = \sum_i c_i f_i(Q) \tag{2.28}$$

where c_i and $f_i(Q)$ are the concentration and scattering factor of the ith atom type in the sample respectively. This modification means that the X-ray total correlation functions, $T^X(r)$ has a form

$$T^X(r) = 2\,\pi^2 \rho_0 r + \int_o^\infty \frac{Qi(Q)}{f_e^2(Q)}\; M(Q) Sin(r\,Q) dQ \tag{2.29}$$

$T^X(r)$ has units of Å^2 and has been multiplied by a factor of $\pi/2$, as compared to neutron correlation function. The X-ray component peak function $P_{ij}^X(r)$, become complicated by the Q-

dependence of form factors, and for data normalized to sharping function is define by Equation 2.30.

$$P_{ij}^{X}(r) = \frac{1}{\pi}\int_{0}^{\infty} \frac{f_i(Q)f_j(Q)}{f_e^2(Q)}\, M(Q)Cos\,(r\,Q)dQ \qquad (2.30)$$

Because $f(Q)$ is different for each type of atom, $P_{ij}^{X}(r)$ is different for each ij atomic pair.

2.9 The Modification Function

The termination of pair distribution function (PDF) at Q_{max} is equivalent to multiplication by a modification function $M(Q)$. The effect of $M(Q)$ can be investigated by looking more closely at $P_{ij}^{X}(r)$. The termination at Q_{max} causes two errors in PDF. The first a loss of resolution, and second, the introduction of spurious ripples of wavelength Q_{max}.

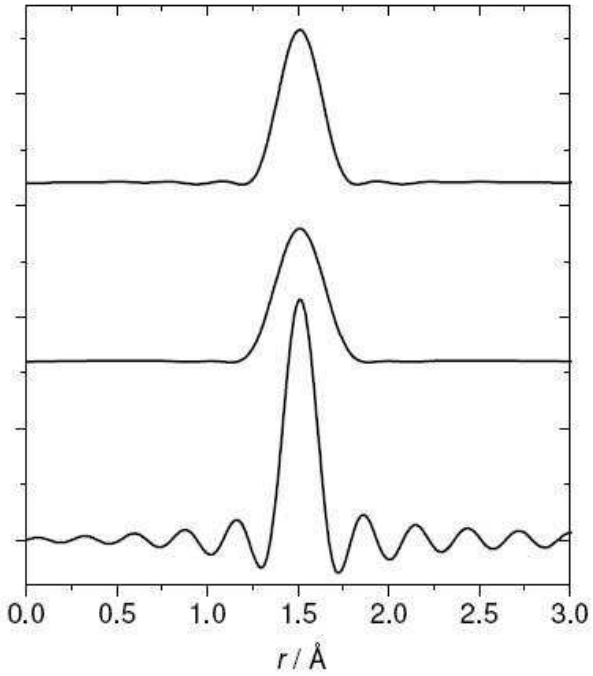

Figure 2. 5: Variation of $\boldsymbol{P_{ij}^{X}(r)}$ using Step function (bottom), Hanning (Middle) and Lorch (Top) modification functions.

If a sharp truncation is used $(i.e. M(Q) = 1)$ over the extent of measured Q, hereafter referred to as Step modification function then $P_{ij}^{X}(r)$ exhibits pronounced termination ripples on either side of the central maximum [17] (see Figure 2.5). These features can be misinterpreted as being real and can lead to false results. It is possible to reduce the termination ripples by using a different form of $M(Q)$ to damp high Q oscillations. Many variations of $M(Q)$ have been formulated [18], but two are of particular interest here.

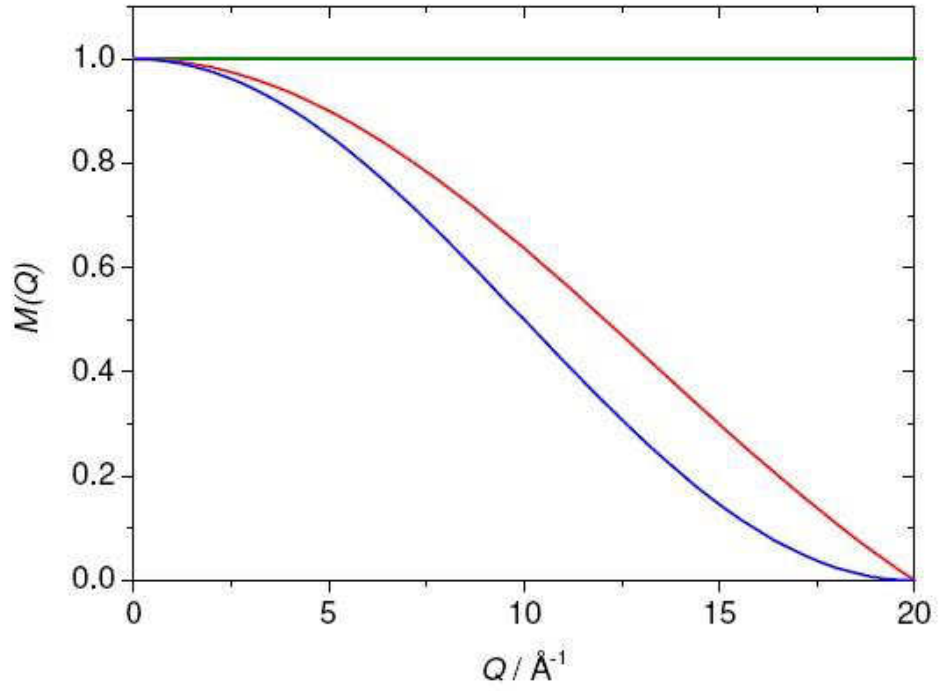

Figure 2. 6: Graphical representation of $\boldsymbol{M(Q)}$ *over the range of* $\mathbf{0} \leq \boldsymbol{Q} \leq \mathbf{20}$ $\mathbf{Å^{-1}}$, *Hanning (Blue) and Loch (Red) and Step function (Green).*

The first is the modification function proposed by Lorch (91).

$$M(Q) = \begin{cases} \dfrac{Sin(\Delta r\, Q)}{\Delta r\, Q} & if\ \ Q \leq Q_{max} \\ 0 & otherwise \end{cases} \qquad (2.31)$$

The second is the raised cosine Hanning function

$$M(Q) = \begin{cases} 1 + \cos(\frac{Q\Delta r}{2}) & if\ Q \leq Q_{max} \\ 0 & otherwise \end{cases} \quad (2.32)$$

In Equations 2.31 and 2.32, Δr defines the experimental real space resolution and is equal to π/Q_{max}. The different forms of $M(Q)$ are highlighted in Figure 2.6.

References

[1] B. E. Warren, X-Ray Diffraction, New York: Addison-Wesley, 1969.

[2] R. Pynn, "Neutron Scattering, A Primer," *Los Alamos Science, Neutron Diffraction,* vol. 19, 1990.

[3] T. Egami and S. J. Billinge, "Crystallographic analysis of complex materials," in *Underneath the Bragg Peak: Structure analysis of complex materials*, Elsevier, 2003, pp. 25-54.

[4] G. L. Squires, Introduction to the Theory of Thermal Neutron Scattering, Cambridge: Cambridge University Press, 2012.

[5] L. V. Hove, "Correlations in space and time and born approximation scattering in the system of interacting particles," *Phys Rev,* vol. 95, pp. 249-262, 1954.

[6] D. I. Grimley, A. C. Wright and R. N. Sinclair, "Neutron scattering from vitreous silica IV: time-of-flight Diffraction," *Journal of Non-Crystalline Solids,* vol. 119, no. 1, pp. 49-64, 1990.

[7] P. A. Johnson, A. C. Wright and R. N. Sinclair, "Neutron scattering from vitreous silica II: Twin axis diffraction experiment," *Journal of Non-Crystalline Solids,* vol. 58, no. 1, pp. 109-130, 1983.

[8] R. N. Sinclair and A. C. Wright, "Neutron Scattering From Vitreous silica 1: The Total-Cross-section," *Journal of Non-Crystalline Solids,* vol. 57, no. 3, pp. 447-464, 1983.

[9] A. C. Wright and R. N. Sinclair, "Neutron Scattering From Vitreous silica 3: Elastic Diffraction," *Journal of Non-Crystalline Solids,* vol. 76, no. 23, pp. 351-368, 1985.

[10] A. J. Leadbetter and A. C. Wright, "Diffraction studies of glass structure 1: Theory and Quasi-crystalline model," *Journal of Non-Crystalline Solids,* vol. 7, pp. 23-36, 1972.

[11] J. Mackenzie, a Modern aspect of the vitreous state, Butterworths, 1960.

[12] S. J. Billinge, "The atomic pair distribution function: Past and Present," *Z kristallogr,* vol. 219, pp. 117-121, 2004.

[13] A. J. Leadbetter and A. C. Wright, "Diffraction studies of glass structure 3: Limitations of the Fourier Methods for polyatomic glasses," *Journal of Non-Crystalline Solids,* vol. 7, pp. 141-155, 1972.

[14] D. A. Keen, "A comparison of various commonly used correlation functions for describing total scattering," *Journal of Applied Crystallography,* vol. 34, pp. 172-177, 2001.

[15] S. Susman, K. J. Volin, D. G. Montague and D. L. Price, "The structure of vitreous and liquid GeSe2," *A neutron diffraction study,* vol. 125, p. 168, 1990.

[16] C. J. Benmore, "X-ray Diffraction from glasses," in *Modern glass characterization*, Wiley - American Ceramic Society, 2015, pp. 241-267.

[17] C. Simmons and O. El-Bayoumi, Experimental Techniques of Glass Science, American Ceramic Society, 1993.

[18] J. Waser and V. Schomaker, "The Fourier Inversion of diffraction data," *Review of Modern Physics,* vol. 25, no. 3, pp. 671-690, 1953.

[19] E. Lorch, "Neutron diffraction by Germania, Silica, and radiation damaged silica glasses," *Journal of Physics C: Solid state physics,* vol. 2, no. 2, p. 229, 1969.

CHAPTER 3

EXPERIMENTAL SETUP

This chapter deals with the experimental techniques of glass preparation, measuring thermal and physical properties, High Energy X-ray diffraction (HEXRD) data, and absorption, photoluminescence, and FTIR spectra for rare earth-doped sodium phosphate glasses. All these techniques are useful to understand the atomic-level structure of these glasses and the influence of that on the thermal, vibrational, and optical properties. Moreover, the optical response of the rare-earth ion in any host can be understood from knowledge of energies, and intensities of the transitions involved. In the present work, we have systematically studied the influence of g Na_2O and Re_2O_3 concentrations on the structural and spectroscopic properties of phosphate glasses. One objective of the study was to find the Na_2O concentration that yield the highest T_g which would be useful for waveguide fabrication and other applications. We have also attempted to study how the Re_2O_3 $(Re = Pr, Nd, Er)$ concentration influence concentration quenching, fluorescence bandwidth $(\Delta\lambda_e)$, fluorescence lifetime (τ_f) and quantum efficiency of Re^{3+}. Furthermore, an analysis of fluorescence and infrared spectra is expected to provide valuable information on the modifications in the local structural units. Such information is crucial for developing practical applications for these glasses.

3.1 Glass Preparation

There are a wide variety of techniques for the synthesis of glasses such as melt-quenching, sol-gel, chemical vapor deposition, sputtering, glow discharge, etc. Out of these, the melt-quenching technique and sol-gel processing are most popular, being relatively easy to prepare laboratory scale samples [1].

3.1.1 Melt-Quenching Technique

In this process, a stoichiometric batch (the mixture of raw materials) is melted at a temperature range $1100 - 1600$ ℃ for a certain duration depending on the melting point of its components and the viscosity of the melt. After casting, the glass is properly annealed near the glass transition temperature to remove residual thermal stresses. A schematic representation of glass preparation by the melt-quenching technique is depicted in Figure 3.1. The batch is prepared by proper selection of raw materials followed by chemical calculations, weighing and mixing. The homogenization of the glass melts is ensured by occasional stirring of the molten mass by a platinum, alumina, or silica glass rod. Glass melting crucibles may be fused silica (SiO_2), alumina (Al_2O_3), pure platinum (Pt) or oxide dispensed strengthened (ODS) platinum. Even though pure platinum (Pt) or ODS platinum crucibles yield samples with minimum contamination, they are very expensive. We used alumina crucibles.

3.1.2 Rare-Earth-Doped Sodium Phosphate Glasses

Samples of nominal composition $xRE_2\,O_3 - yNa_2O - (1 - x - y)\,P_2O_5$ prepared at the Physics & Astrophysics Department, University of North Dakota. Glasses were prepared using mixtures of P_2O_5 , $NaHCO_3$ and high purity (99.999 % RE_2O_3 ($RE = Pr, Nd, Er$) with $0.005 \leq x \leq 0.05$ ($x = molar\ fraction$), and $x + y = 0.4$.

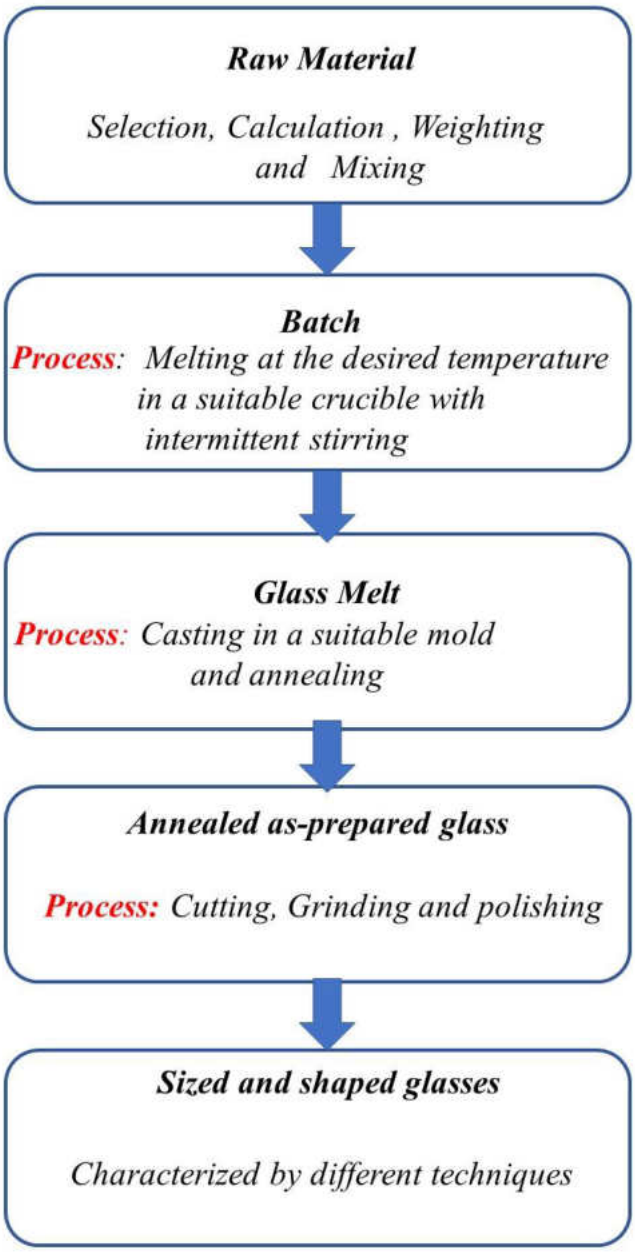

Figure 3. 1: Schematic illustration of different steps of glass preparation by the melt-quenching technique. [1]

By the addition of Na_2O, we can prepare phosphate glasses with very low- rare-earth concentration without the risk of increasing the hygroscopic nature of glasses. Furthermore, the addition of Na_2O also provides suitability for the fabrication of optical waveguide devices by ion-

exchange and also improves the rare-earth solubility, leading to the possibility of using a high concentration of dopants, which is crucial in the design of high-efficiency short length fiber amplifiers [2] [3]. The batch was mixed and melted in an open crucible at 1300 ℃ for 1 $hour$ in a high-temperature furnace. The melt was quenched in air by pouring into 1 cm ×1 cm ×5 cm steel mold. Quenched samples were transferred to an annealing furnace as soon as it solidified, and annealed at 300 ℃ for approximately 90 $minutes$ as shown in Figure 3.2. As final prepared glasses are similar to those shown in Figure 3.3.

The composition of the rare-earth doped sodium phosphate glass samples was analyzed using both Energy Dispersive X-ray Analysis (EDAX) and normalization method proposed by Mehdi Ali et al [4]. Figure 3.4 gives the composition of the glasses on ternary plot.

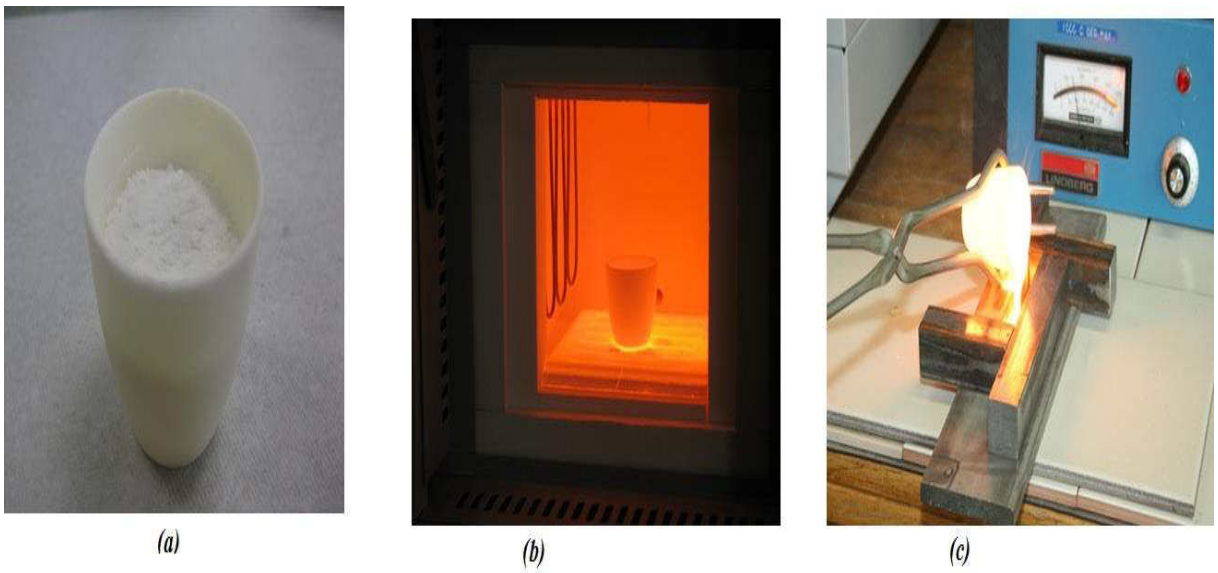

Figure 3. 2: (a) Batched amount of P_2O_5, Na_2CO_3 and RE_2O_3 were mixed (b) Melt at 1300 ℃ *for 1 hour (c) Melt were quenched in air and transferred to an annealing furnace at* 300 ℃ *for 90 minutes.*

Figure 3. 3: Pr(green), Nd(purple) and Er (pink) doped sodium phosphate glasses.

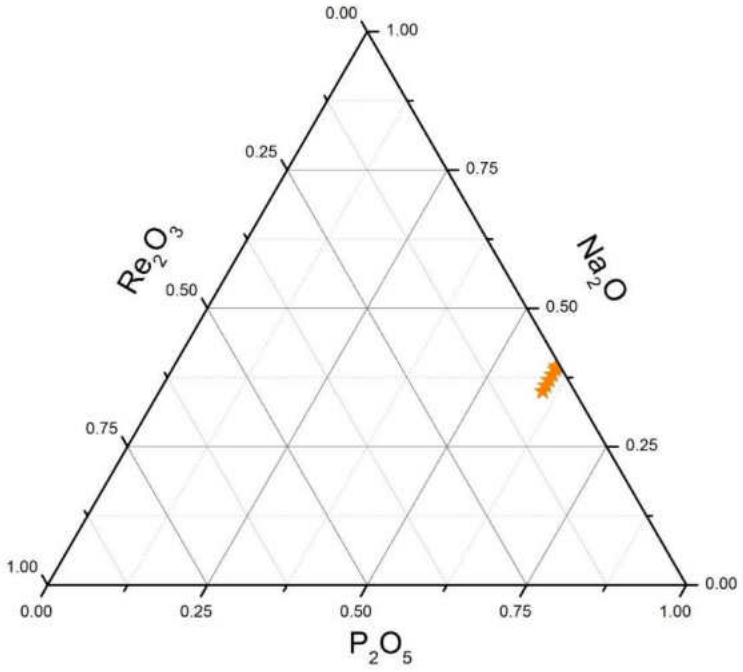

Figure 3. 4: Ternary plot representing the composition of the rare-earth doped sodium phosphate glasses investigated.

3.2 Data collection

3.2.1 Density Measurements

Densities of samples at room temperature using the Archimedes principle with Kerosene as the immersion liquid [5]. The number density, density and molar volume of these glasses are shown in Table 3.1

3.2.2 Molar Volume Calculations

The molar volume of the glass samples can be calculated from the following expression (97)

$$V_m = \frac{M}{\rho} = \frac{\sum n_i M_i}{\rho} \tag{3.1}$$

where M_i is the molecular weight for component i, n_i is the molar fraction of the i^{th} component, ρ is the sample density in g/cm^3, and M is the molecular weight of the sample.

3.3 High Energy X-Ray Diffraction (HEXRD)

The X-ray diffraction experiments were performed at beamline 11 IDC at the Advance Photon Source (APS) at Argonne National Lab (ANL) Illinois. The incident photon energy was 114.80 keV($\lambda = 0.010783\, nm$). Powder samples were loaded into thin-walled polyimide capillary tubes ($D = 1.3716\, mm$) and placed in a X-ray beam of cross-section 0.5 ×0.5 mm^2 and 10^{11} $photons/sec$ flux. The scattered intensities were measured using an amorphous silicon detector ($Perkin\ Elmer - XRD$ 1621). Data for each sample was acquired in 10 sets for 30 seconds. Each sample was measured at two sample -detector distance, 380 mm ($2\theta = 0.01^{\circ} - 42.2^{\circ}, Polarization = 0.99$) and 420 mm. Data sets were also measured for the empty tube and dark current. For instrumental calibration, a reference CeO_2 sample was also measured. usable dynamic range after the data reduction was $Q \approx 0.05 - 29$ Å^{-1}, yielding a real space resolution.

Table 3. 1: Density and Number Density of $(\boldsymbol{RE_2O_3})_x(\boldsymbol{Na_2O})_y(\boldsymbol{P_2O_5})_{1-x-y}$ *,* $\boldsymbol{RE = Pr, Nd, Er}$ *glasses*

ID	***Composition (molar fraction)***		***Density***	
	$RE_2O_3(x)$	$Na_2O\ (y)$	$\rho(\frac{g}{cm^3})$	$\rho_0(\frac{Atoms}{Å^3})$
Pr0.005	0.005	0.395	2.545	0.074513
Pr0.01	0.01	0.39	2.578	0.074704
Pr0.02	0.02	0.38	2.628	0.074658
Pr0.03	0.03	0.37	2.716	0.075700
Pr0.04	0.04	0.36	2.730	0.074663
Pr0.05	0.05	0.35	2.794	0.075046
Nd0.01	0.01	0.39	2.697	0.078110
Nd0.02	0.02	0.38	2.623	0.074429
Nd0.03	0.03	0.37	2.673	0.074365
Nd0.04	0.04	0.36	2.732	0.074554
Nd0.05	0.05	0.35	2.796	0.074891
Er0.005	0.005	0.395	2.661	0.077734
Er0.01	0.01	0.39	2.725	0.078596
Er0.02	0.02	0.38	2.774	0.078098
Er0.03	0.03	0.37	2.820	0.077545
Er0.04	0.04	0.36	2.902	0.078015
Er0.05	0.05	0.35	2.905	0.076386

$\Delta r = 0.21$ Å where $\Delta r \approx 2\pi/Q_{max}$. A sketch of HEXRD setup is shown in Figure 3.5, and the flowchart of HEXRD data analysis is provided in figure 3.6.

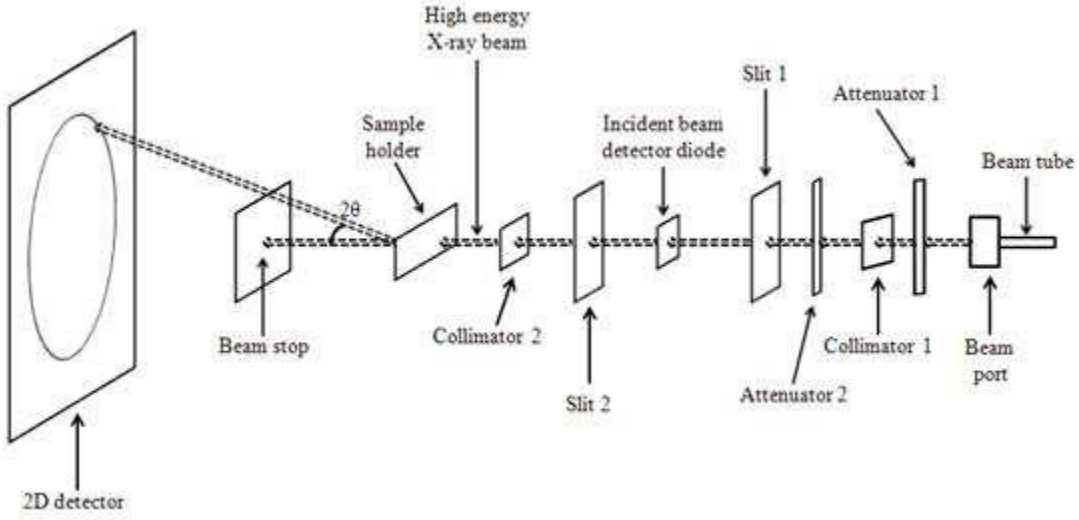

Figure 3. 5: Sketch of HEXRD setup at APS, Argonne National Lab.

3.4 Differential Thermal Analysis (DTA)

The thermal analysis is usually carried out using a group of techniques in which a physical sample property is measured as a function of temperature, while the sample is subjected to predefined heating or cooling rates. In DTA, the temperature difference between a sample and an inert reference material is measured under same heat treatment. If the sample undergoes a chemical or phase change, a temperature difference $\Delta T = T_{Sample} - T_{Reference}$, will be observed between the sample and the reference.

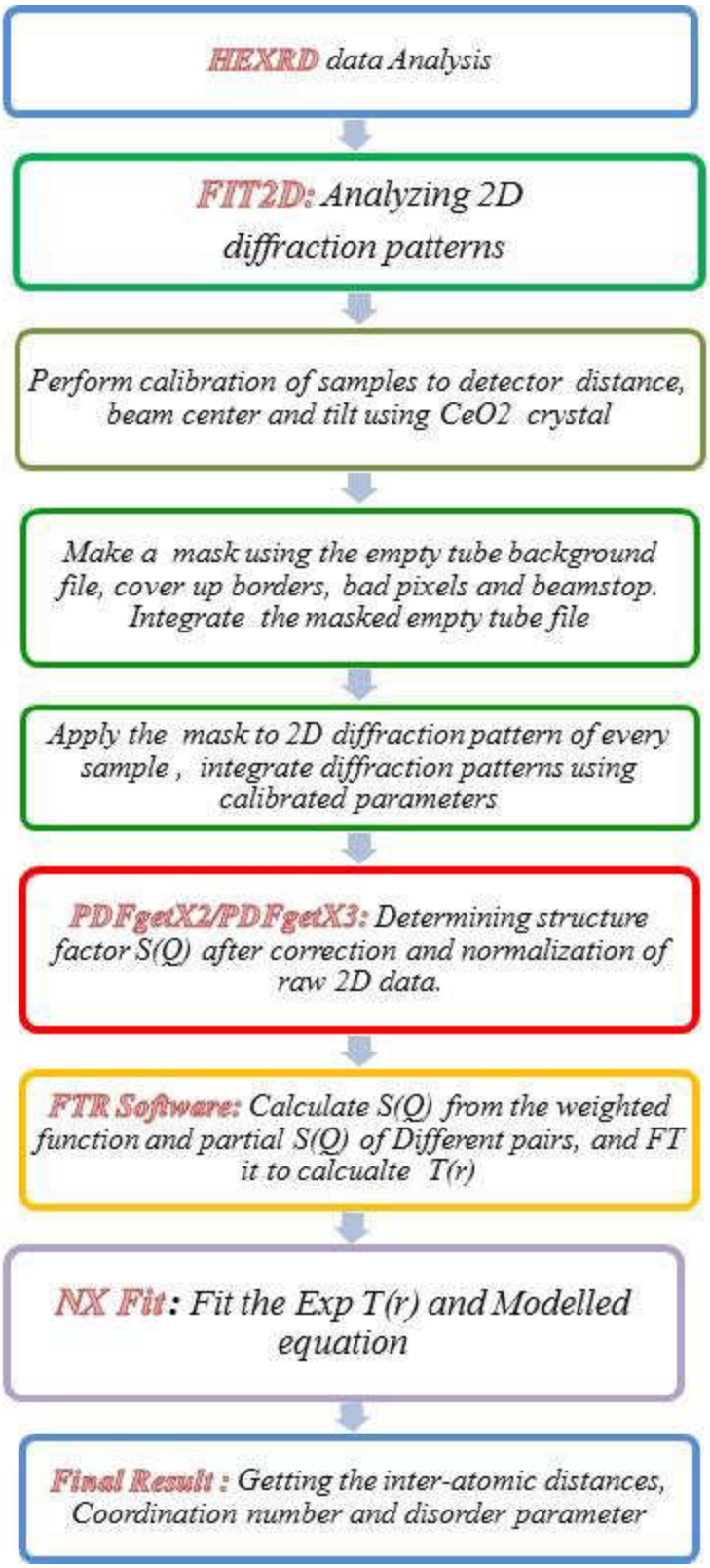

Figure 3. 6: Flow chart of HEXRD data analysis.

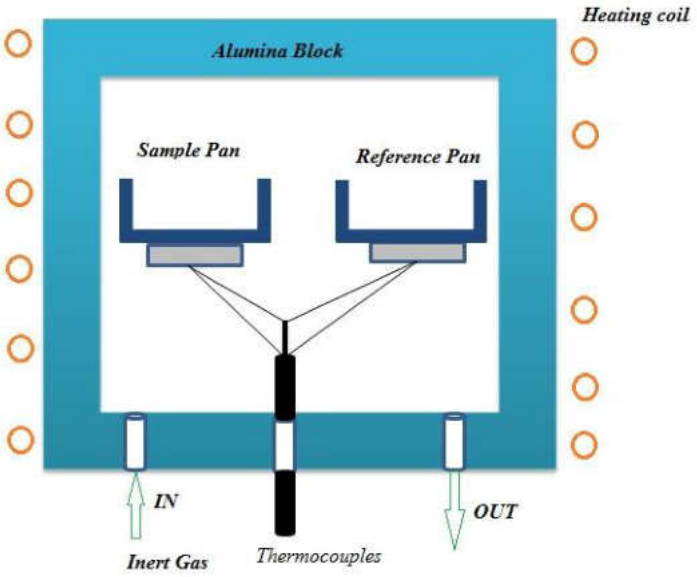

Figure 3. 7: Differential thermal analysis (DTA) Setup for glass transition measurement.

Differential Thermal Analysis (DTA) measurements were done using Perkin-Elmer DTA 7 setup. All measurements were performed at a heating rate of $10\ ℃/min$ using platinum holders. About 30mg of glass powder was heated in a alumina crucibles in air from $150\ ℃$ to $800\ ℃$.

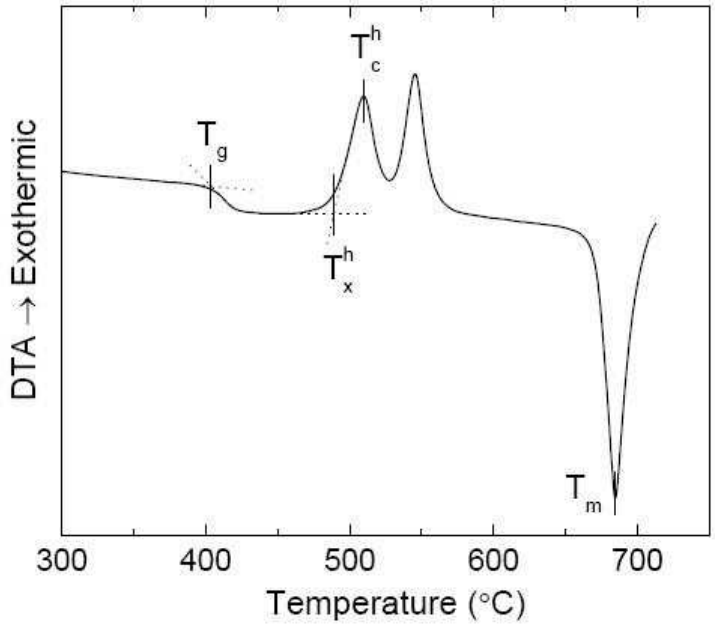

Figure 3. 8: DTA data of powder glass in air at $10\ ℃/min$.

All the samples were preheated in the DTA above the glass transition temperature T_g then cooled at the constant rate of $-10\ ℃/min$ to eliminate the fictive temperature effects before re-heating at the same rate to record T_g. The schematic of DTA setup is shown in Figure 3.7.

Several parameters relevant to glass stability on heating are obtained from DTA or DSC (Differential Scanning Calorimetry) experiments, which provide characteristic temperature, including the glass transition temperature T_g, the crystallization onset temperature T_x^h, and the crystallization peak temperature of heating T_c^h [7]. The melting point T_m, solidus temperature T_S and liquid temperature T_L of a composition are also important characteristic temperatures. From DSC/DTA data, the T_S and T_L can be determined for some glasses by the beginning (onset) and the end (offset) of the melting endotherms. The characteristic DTA curve is shown in Figure 3.8 [8].

3.5 Fourier Transform Infrared Spectroscopy (FTIR)

Glass structure was characterized by Fourier Transform Infrared (FTIR) spectroscopy. FTIR spectra of glasses were recorded with a Thermo-Nicolet (Nexus 879) FTIR spectrometer in the wavenumber range from $400 - 1400\ cm^{-1}$ and from $400 - 4000\ cm^{-1}$. The measurements were made on glass powder by mixing and grinding a small quantity of glass powder with spectroscopic grade dry KBr powder. The mixture were then compressed to form thin pellets for testing. All the measurements were done at $2\ cm^{-1}$ resolutions. The layout of FTIR setup is shown in Figure 3.9 [9].

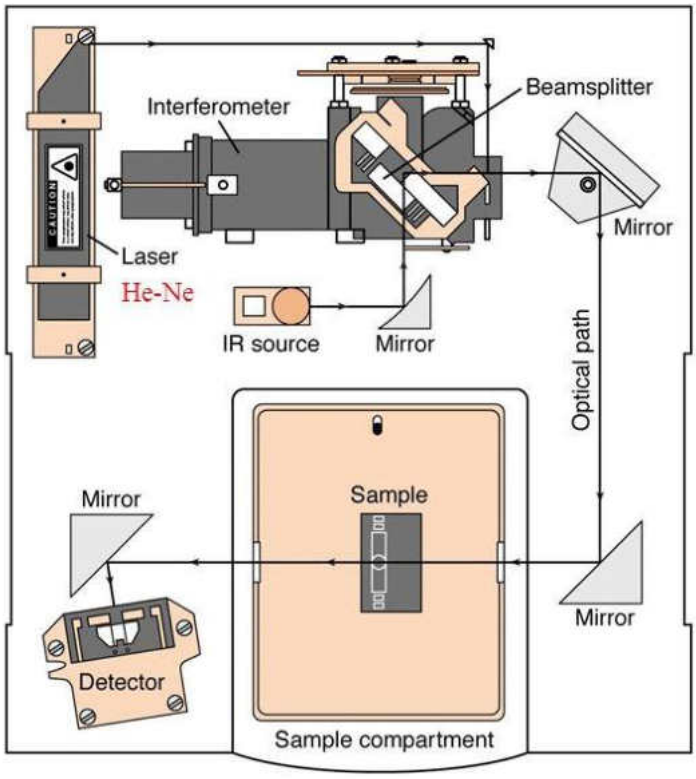

Figure 3. 9: Layout and beam path of Nexus 870 FTIR spectrometer.

3.6 FT-Raman Spectroscopy

For Raman measurements, fine glass powder was examined using Fourier Transform Raman (FT-Raman) spectrometer (Model Nexus 760) equipped with a 2W $Nd{:}YAG$ laser ($1064\ nm$) and near-infrared (NIR) interferometer coupled to either a liquid nitrogen cooled Germanium (Ge) or Indium Gallium Arsenide (InGaAs) detectors at room temperature. An interferometer converts the Raman signal into an interferogram, permitting the detector to collect the entire Raman spectrum simultaneously. Application of the Fourier Transform algorithm to the interferogram converts the results into a conventional Raman spectrum. FT-Raman is the best choice in situations where samples fluoresce or are likely to contain minor impurities that may fluoresce. The room temperature FT-Raman spectrum was recorded using InGaAs detector with a resolution of 2 cm^{-1}.

All samples were ground into fine powder and placed in NMR sample tubes. The Raman spectra are usually presented by the Stoke shift, whereas anti-Stoke shifted spectras were omitted. The layout of FT-Raman spectrometer is shown in Figure 3.10.

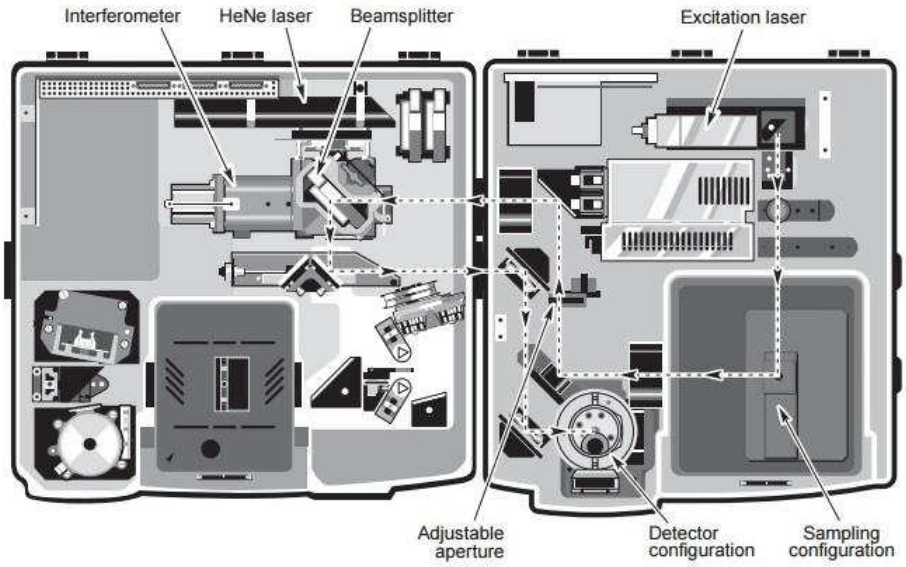

Figure 3. 10: FT-Raman spectrometer layout and beam path. [9]

3.7 Optical Measurements

3.7.1 Absorption Spectra

The absorption spectra were measured on a Perkin Elmer Lambda 1050 UV/VIS spectrometer at the Department of Chemistry at the University of North Dakota. All the glass samples were cut and polished into a thin disk of thickness $\approx 4-6\ mm$.The recorded absorption data was collected in the range from $400-1100\ nm$ at a resolution of $3nm$, and all the transitions were assigned using the Dieke diagram [10]. The oscillator strengths $\Omega_k(k=2,4,6)$ were calculated using JO theory. The Schematic diagram of JO program is shown in Figure 3.11.

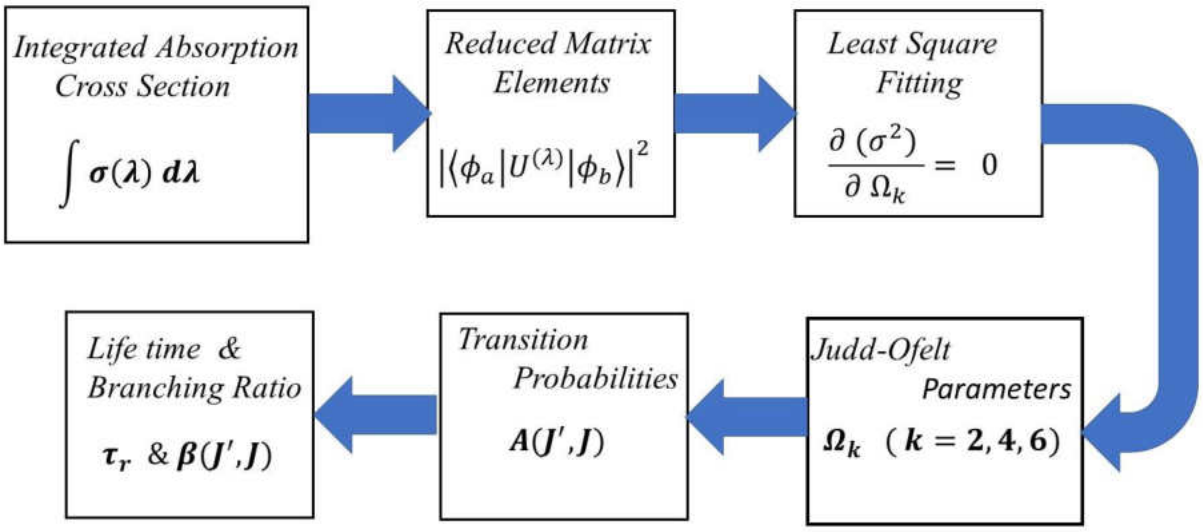

Figure 3. 11: Schematic diagram of JO analysis.

3.7.2 Lifetime Measurements

Luminescence decay measurements were performed at the University of South Dakota (USD) for Er^{3+} and Nd^{3+}doped sodium phosphate glasses. Erbium doped samples were excited with 522 nm laser, which excites Er^{3+} ions to state $^4S_{3/2}$ level. The luminescence decay of Er^{3+} ions from $^4I_{13/2} \rightarrow {}^4I_{15/2}$ transition at 1530 nm was observed. Nd^{3+} doped samples were excited with a 532 nm laser, which excites Nd^{3+} ions to state $^4G_{7/2}$ level. The luminescence decay of Nd^{3+} ions from$^4F_{3/2} \rightarrow {}^4I_{11/2}$ transition at 1064 nm was observed. Decay curves were obtained using a digital oscilloscope. The experimental setup for the lifetime measurements is shown in Figure 3.12.

3.7.3 Emission Measurements

Emission measurements were recorded in visible and NIR region at room temperature. The NIR spectra were recorded on FTIR spectrometer (model Nexus 870 FT-IR, Nicolet) using $Nd{:}\,YAG$ laser with a wavelength of $1064\,nm$ at University of North Dakota, UND. All the measurements were recorded with a resolution of $2\ cm^{-1}$.

The emission measurements were recorded at USD at 532 nm wavelength for excitation laser and monitoring the emission of $^4I_{13/2} \rightarrow {}^4I_{15/2}$ transition for Erbium samples and from $^4F_{3/2} \rightarrow {}^4I_{11/2}$ transition for Nd samples. Luminescence signal was acquired using time-resolved photon counting by feeding the pre-amplified output of photomultiplier to a multichannel scaler (Stanford Research System SR 430).

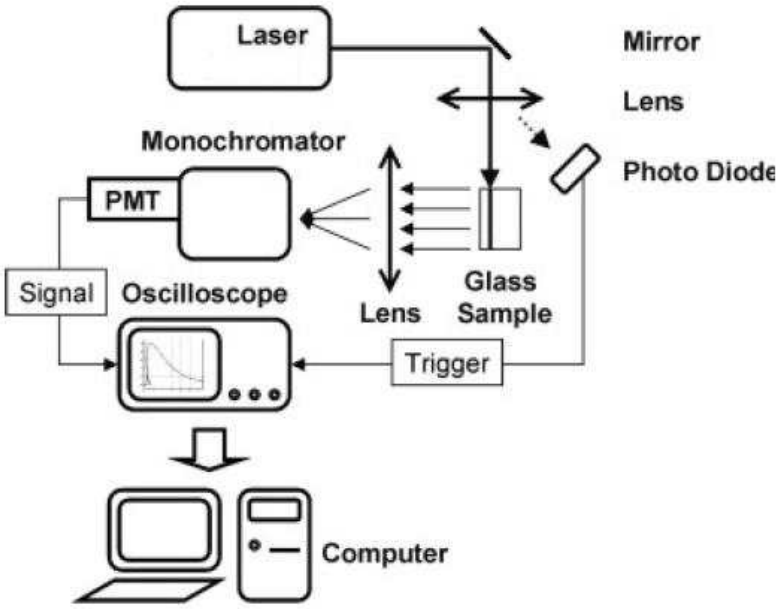

Figure 3. 12: Experimental setup for fluorescence lifetime measurement (Schematically)

References

[1] Karmakar, Rademann and Stepanov, Glass Nanocomposites :Synthesis, properties and applications, William Andrews, 2016.

[2] P. Nandi , A. Srinivasan and G. Jose, "Structural dependent thermal and optical properties of rare-earth doped glasses with mixed glass formers," *Optical Materials,* vol. 31, pp. 653-659, 2009.

[3] G. Lakshminarayana, J. Qiu, M. G. Brik, G. A. Kumar and I. V. Kityk, "Spectral analysis of Er3+, Er3+/Yb3+ and Er3+/Tm3+/Yb3+-doped TeO2-ZnO-WO3-TiO2-Na2O glasses," *Journal of Physics : Condensed Matter,* vol. 20, pp. 375101-375109, 2008.

[4] M. Ali, K. G. Marasinghe, R. Hart, C. Benmore, N. Wyckoff and R. K. Brow, "Normalization and sample composition analysis of binary rare-earth phosphate glasses by high energy X-ray scattering," *Physics and Chemistry of Glasses : Europeanjournal of Glass Science and Technology PArt B,* vol. 47, no. 2, pp. 146-149, 2006.

[5] U. B. Chanshetti, V. A. Shelke, S. M. Jaghav, S. G. Shankarwar, T. k. Chondhekar, A. G. Shankarwar, V. Sudarsan and M. S. jogad, "Density and Molar Volume studies of Phosphate glasses," *Physics, chemistry and Technology,* vol. 9, no. 1, pp. 29-36, 2011.

[6] P. Shih, "Thermal , chemical and structural characterization of Erbium-Doped Sodium Phosphate Glasses," *Materials chemistry and Physics,* vol. 84, no. 1, pp. 151-156, 2004.

[7] R. J. Seyler, Assignment of the Glass Transition, Astm Intl, 1994.

[8] L. N. Ma, "Dissolution Behavior of Phosphate Glasses," Missouri University of Science and Technology, 2014.

[9] *NXR FT-Raman Spectrometer User's Guide,* Thermo electron corporation, 2003.

[10] G. H. Dieke and H. M. Crosswhite, "The Spectra of the Doubly and Triply Ionized Rare Earths," *Applied Optics ,* vol. 2, no. 7, pp. 675-686, 1963.

CHAPTER 4

RESULTS AND DISCUSSION

4.1 Results

4.1.1 Density Measurements

The density of the samples was measured using Archimedes method at room temperature. The density of the glasses increases linearly with the rare-earth concentration as shown in Figure 4.1.

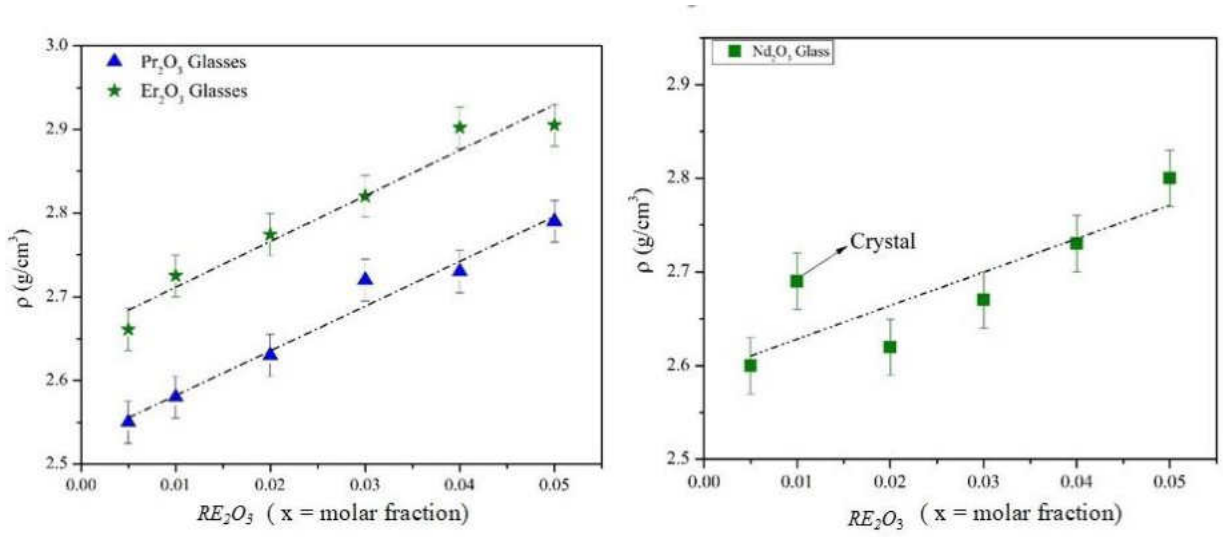

Figure 4. 1: Dependence of the density of Pr, Er and Nd doped sodium phosphate glasses on RE_2O_3 concentration with error bars at $\pm 0.03\ g/cm^3$.

The molar volume V_m of the glass, which tells us about the changes in structural unit increases linearly with increasing the rare-earth concentration as shown in Figure 4.2.

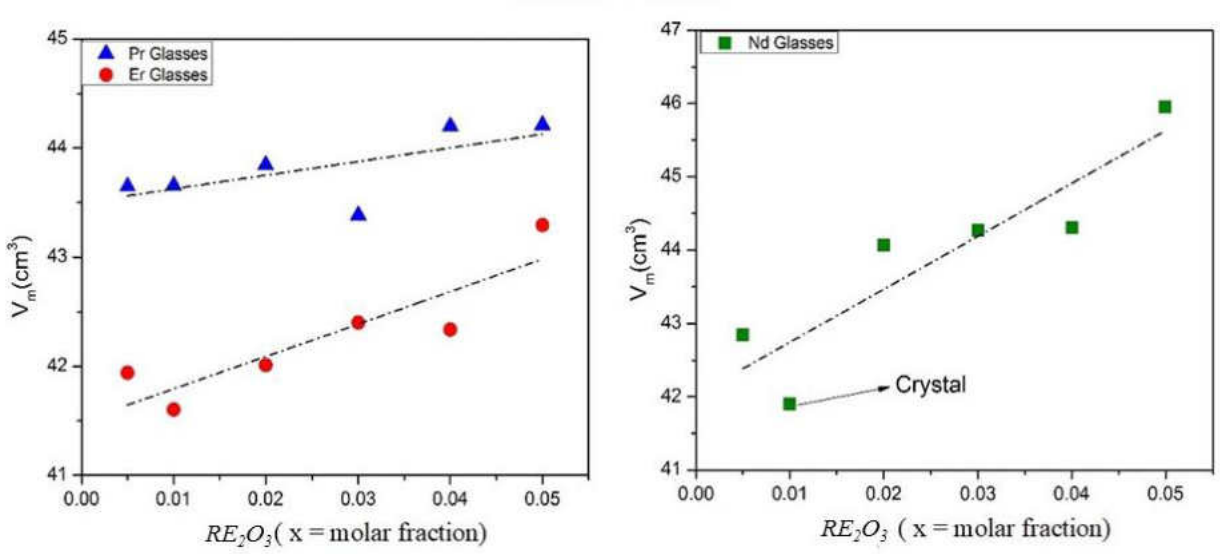

Figure 4. 2: Dependence of the molar volume of Pr, Er and Nd doped sodium phosphate glasses on RE_2O_3 concentration.

4.1.2 Thermal Properties

The glass transition temperatures (T_g), were determined by the differential thermal analysis (DTA) at a heating rate of 10 ℃$/min$.These temperatures were reproducible to $\pm$ 5 ℃ . Data acquisition and processing was done with Perkin-Elmer's Pyris software. From DTA data, one can calculate onset temperature and glass transition temperature. DTA data and measured T_g for erbium *x = 0.01* is shown in Figure 4.3, 4.4 and Figure 4.5.

The glass transition temperature increases with increasing the RE_2O_3 $(RE = Pr, Er)$ concentration as shown in Figure 4.6.

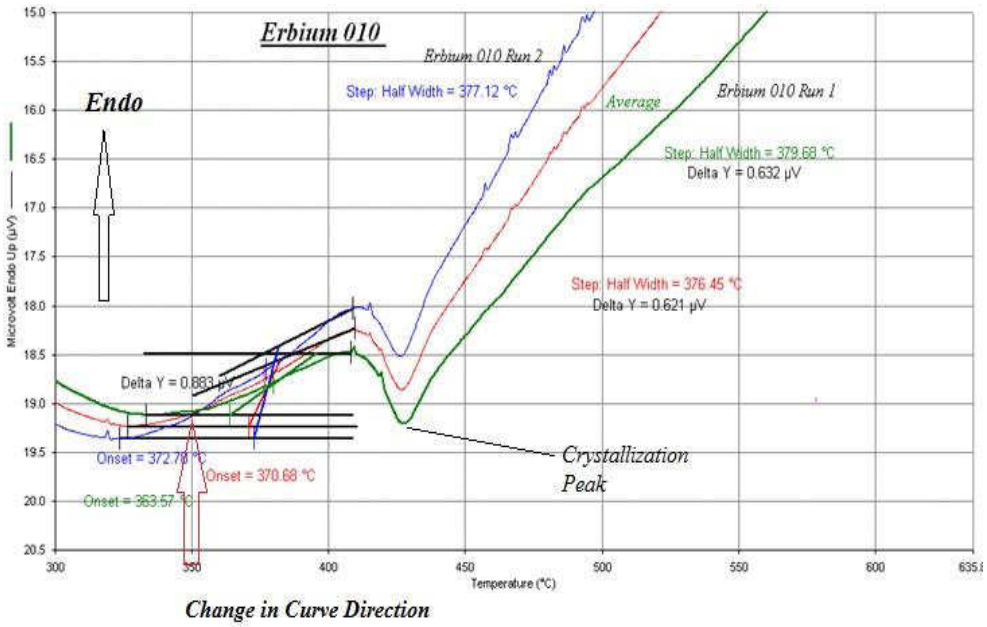

Figure 4. 3: DTA curve for erbium (x =0.01) doped sodium phosphate glasses.

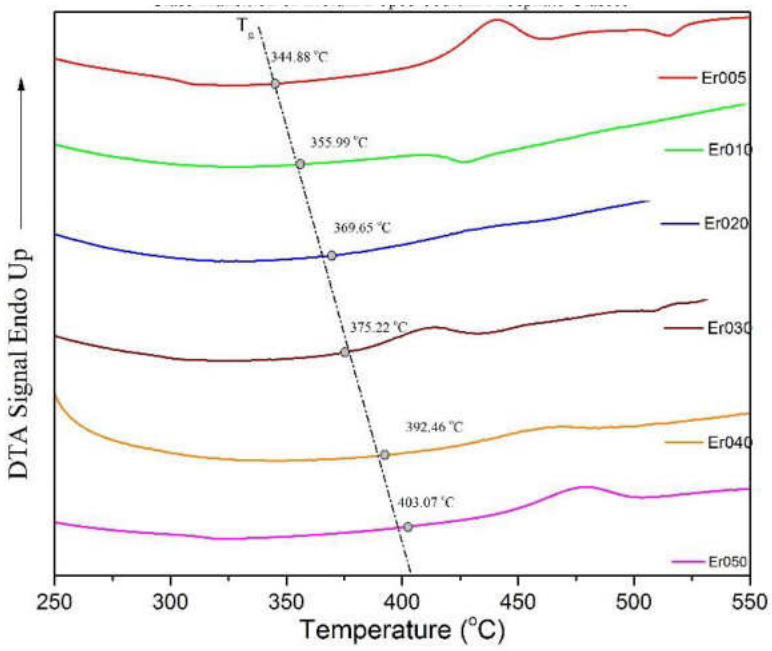

Figure 4. 4: DTA curve for erbium doped samples. The dotted line represents the glass transition temperature of these samples.

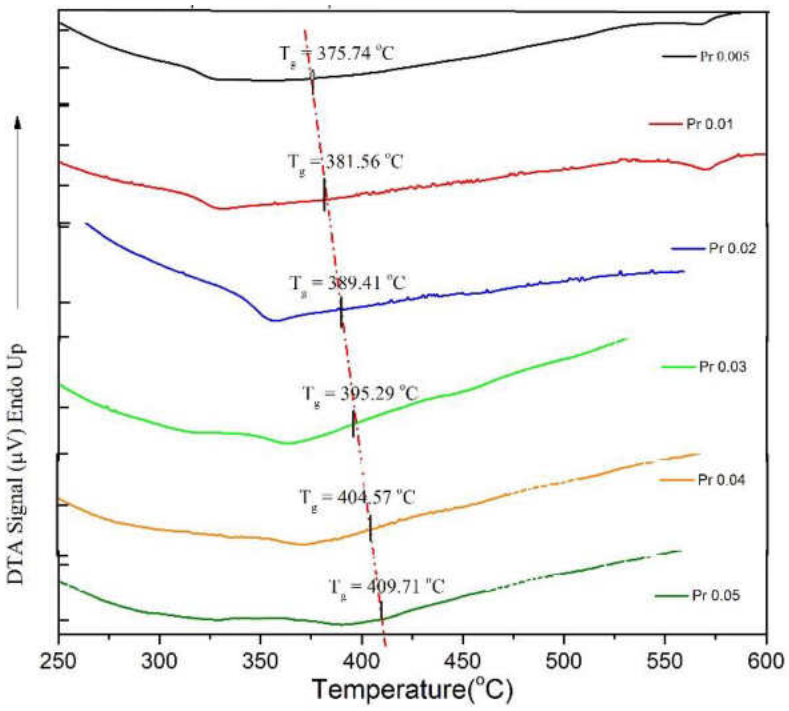

Figure 4. 5: DTA curve for praseodymium doped samples. The dotted line represents the glass transition temperature of these samples.

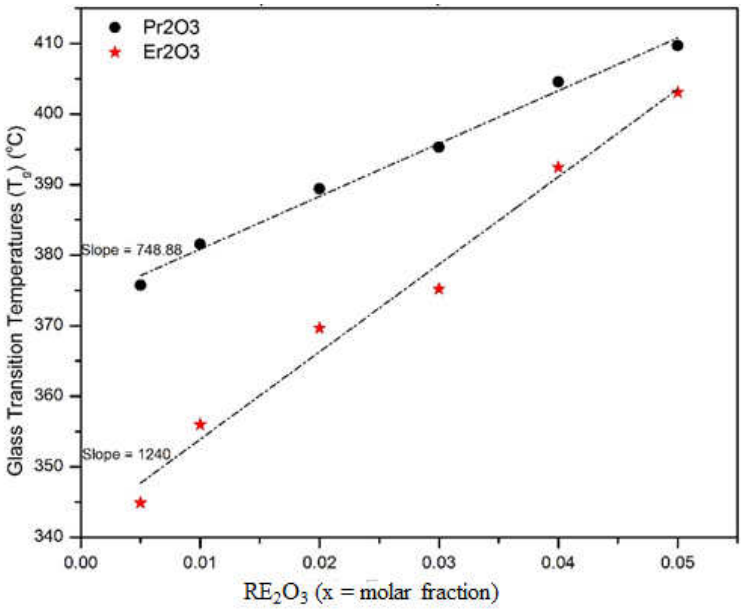

Figure 4. 6: DTA measurements of glass transition temperatures of praseodymium and erbium doped sodium phosphate glasses.

4.1.3 Vibrational Properties

IR spectroscopy is a power tool to probe the short and intermediate-range in glasses. FTIR spectra were recorded with a Thermo Nicolet (Nexus 870) FTIR spectrometer in the wavenumber range $400 - 1400\ cm^{-1}$and from $400 - 4000\ cm^{-1}$. Figures (4.7- 4.9) shows the spectra in the frequency range of $400 - 1400\ cm^{-1}$.

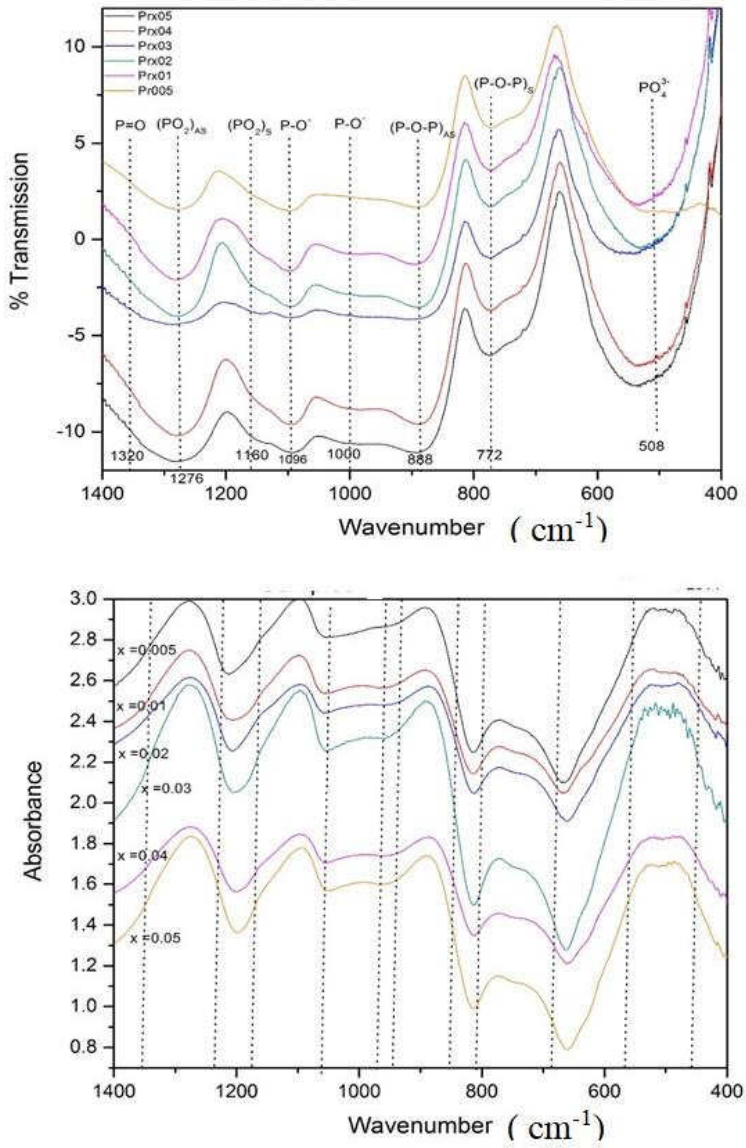

Figure 4. 7: IR transmission and absorbance spectra of Pr doped sodium phosphate glasses. Dotted lines represent the assignment of vibrational bands.

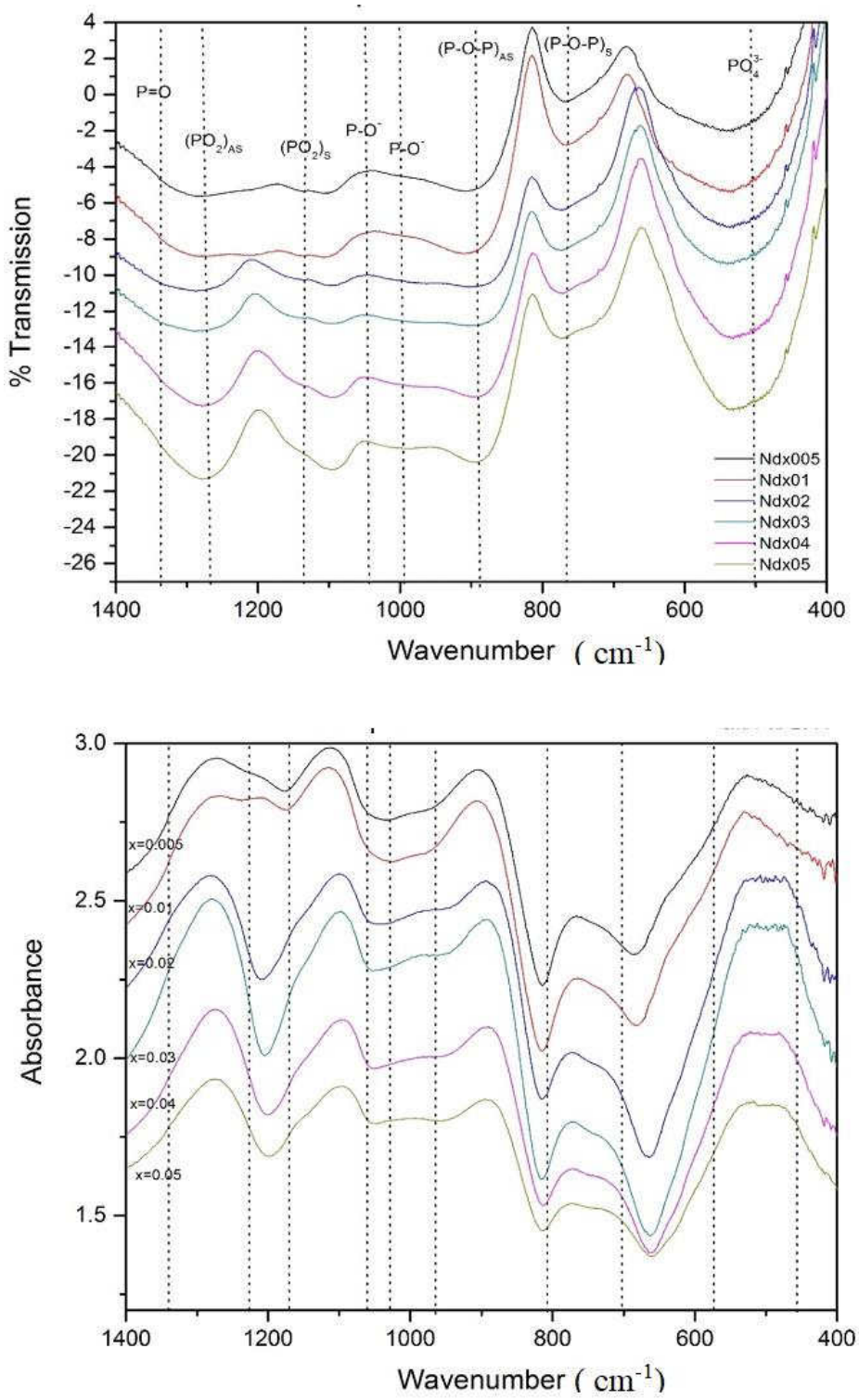

Figure 4. 8: IR transmission and absorbance spectra of Nd doped sodium phosphate glasses. Dotted lines represent the assignment of vibrational bands.

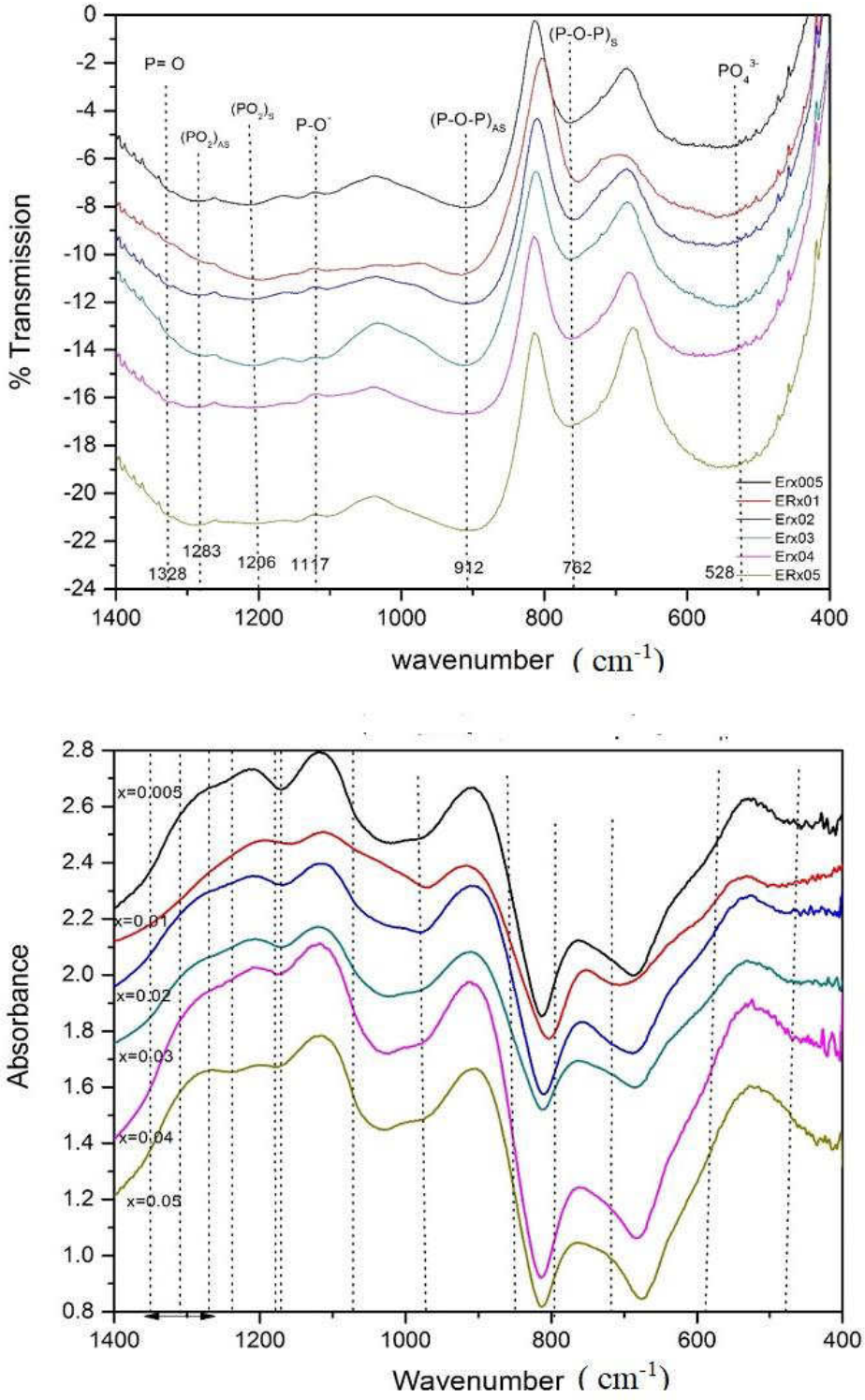

Figure 4. 9 : IR transmittance and absorbance spectra of Er doped sodium phosphate glasses. The dotted line represents the vibration band assignments per ref. [1]

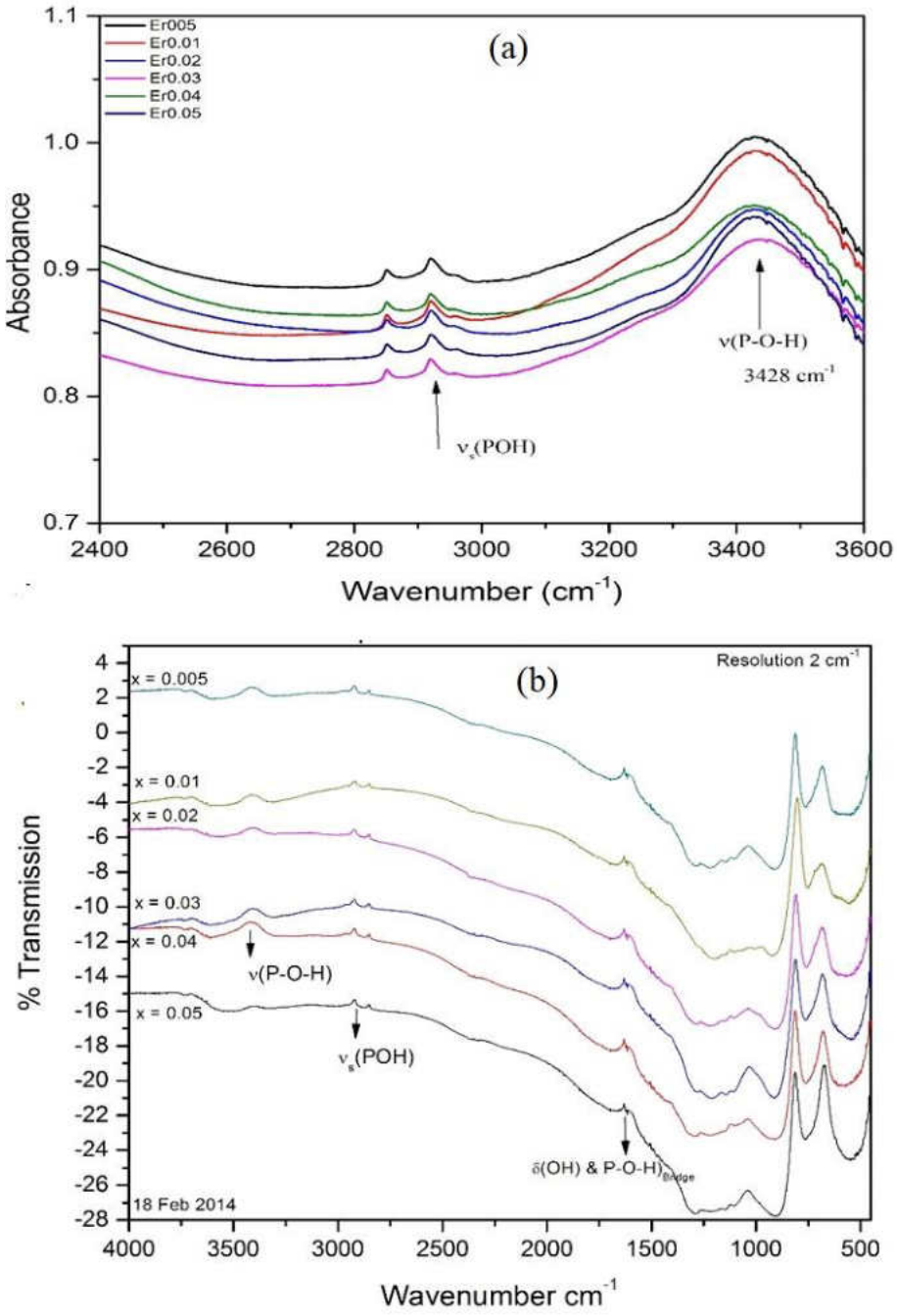

Figure 4. 10: IR spectra indicating the presence of water in glass samples from 400-4000 cm^{-1} *(a) Absorbance spectra from 2400-3600* cm^{-1} *from the presence of OH group (b) IR spectra of erbium doped sodium phosphate glasses.*

The frequency of P = O ($1350\ cm^{-1}$) is affected by the presence of water (which is probably absorbed during the preparation of pellets for IR measurement) as in Figures 4.10.

4.1.3.1 Assignment of Vibrational Bands After Calculations

Structural parameters calculated with and without water are shown in Figure 4.11.

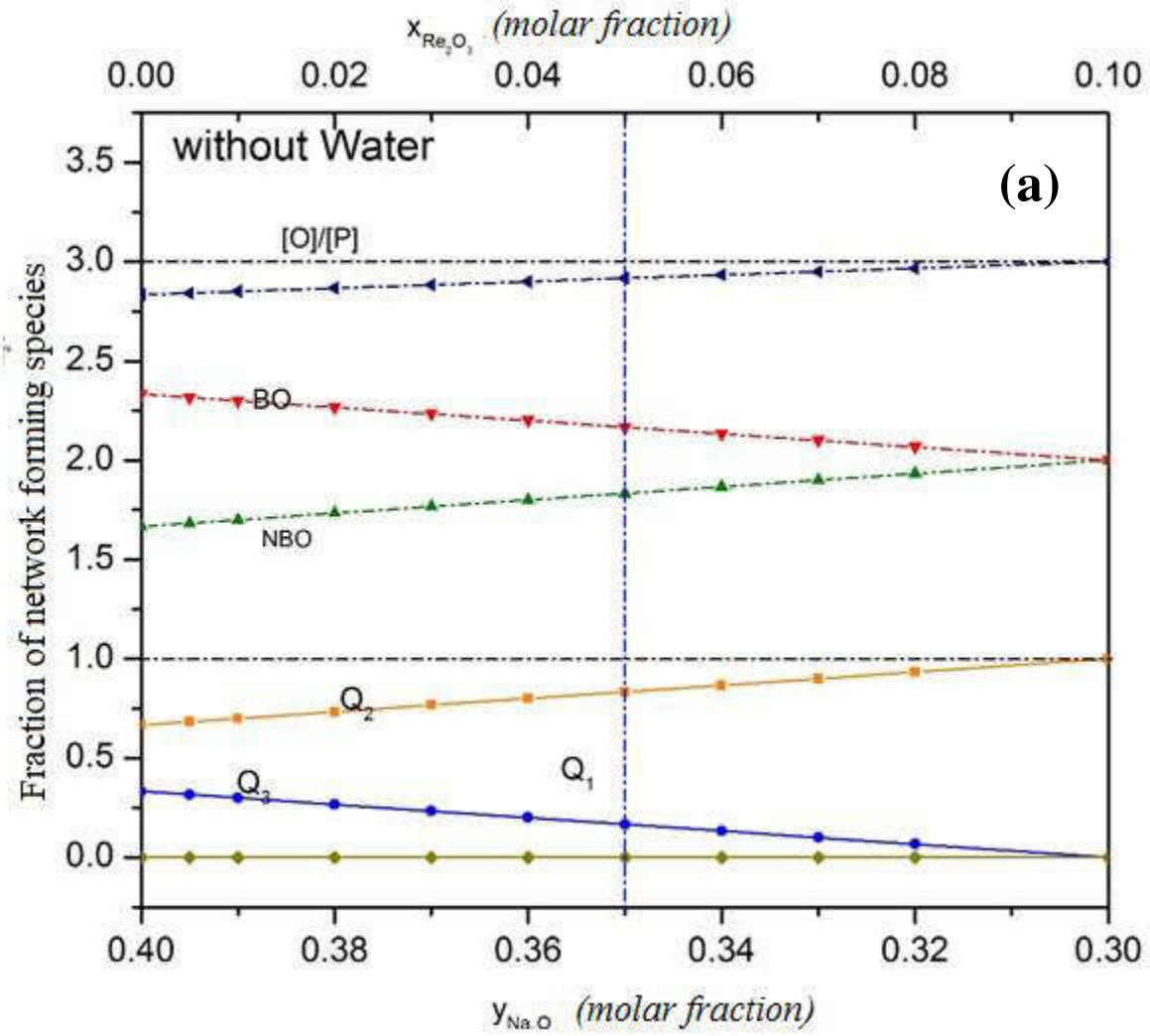

Figure 4.11 (a): Structural calculation of glass samples without water

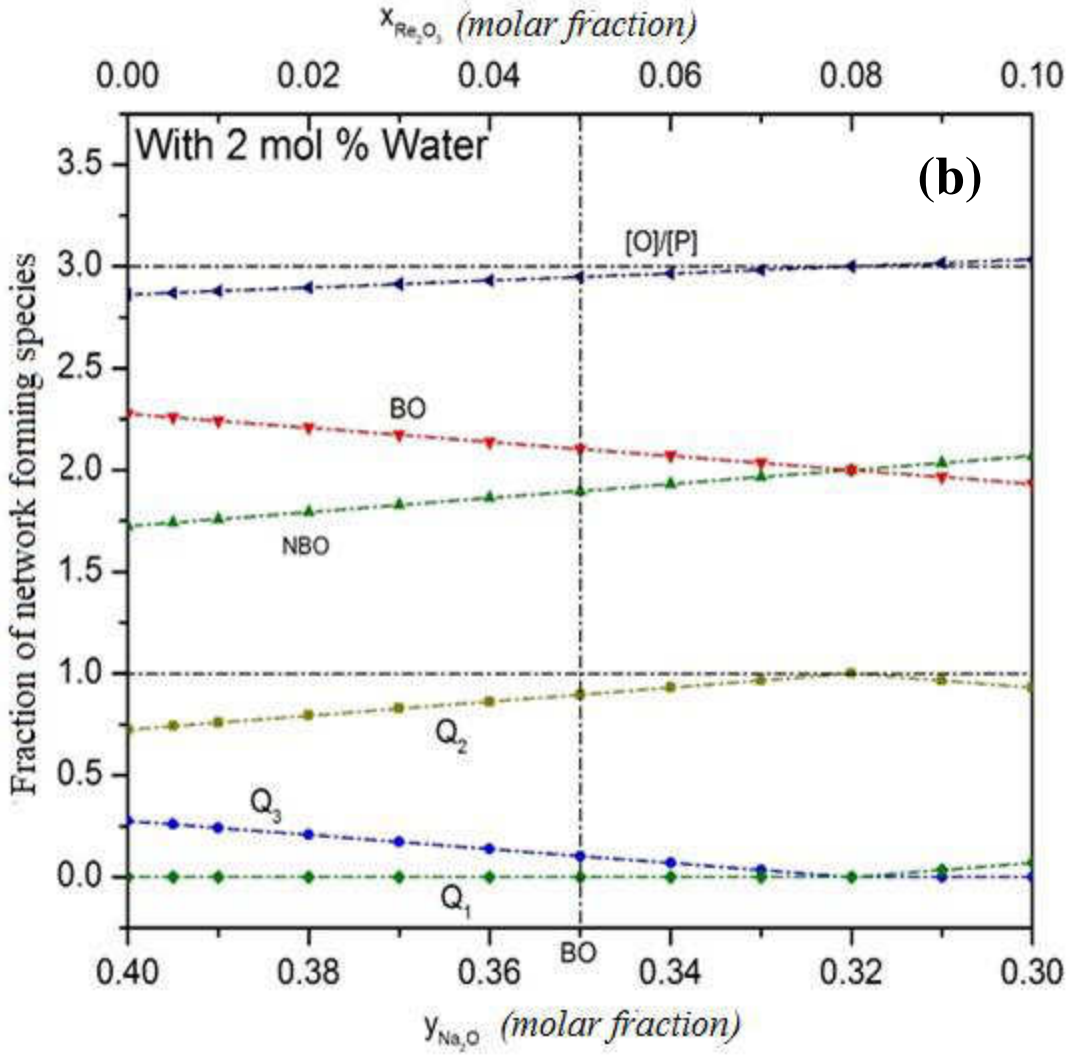

Figure 4. 11: *Structural calculation of glass samples (a) without water and (b) with x = 0.02 of water.*

In Figures 4.11, it is clear from the calculations that the structure of glasses consists of Q^3 and Q^2 tetrahedra network and the glasses are ultraphoshates $\left(\frac{[O]}{[P]} < 3.0\right)$ in the studied range $(0.005 \leq x \leq 0.05)$of compositions.

4.1.3.1 Deconvolution of IR Vibrational Bands

Deconvolution of IR spectra is helpful for determining the parameters of absorption bands [2] [3]. The deconvolution was done in Peak Fit [4] using the same number Gaussian peaks (vibrational bands) for every sample. In Figures 4.12, it is quite evident that IR spectra consists of many broad absorption bands, which represent different phosphate structural groups. These groups are inter-connected in several ways which not only increase the number of allowed vibrational modes but also the absorption bandwidths.

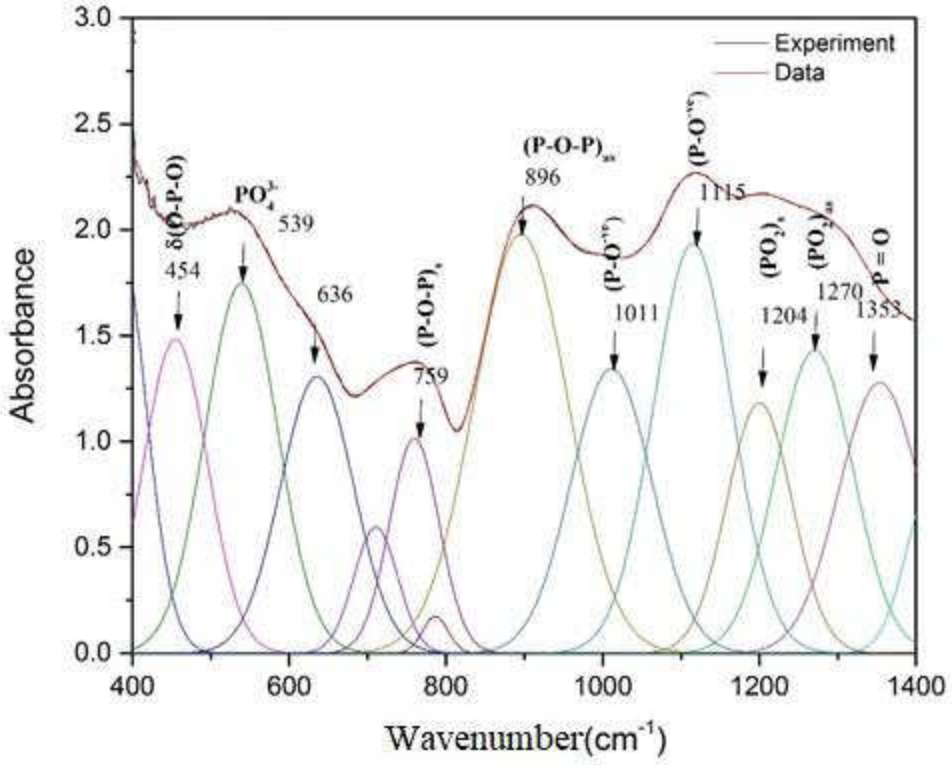

Figure 4. 12: The deconvolution of IR spectra of erbium doped glasses with x = 0.05, y = 0.35.

Figure 4.12 represents an example of peak deconvolution of an IR spectrum. Deconvolution is also very useful for revealing the number of absorption bands related to different vibrational modes of phosphate structural groups. The relative intensity of each has been calculated from $I_n = S_n/S_t$

[2], where I_n is the relative intensity of each n^{th} band, S_n represents the area of each band and S_t is the area under the whole spectrum in the region between $400 - 1400\ cm^{-1}$.

Infrared absorption spectra of vitreous and crystalline phosphate have been used as a basis for the qualitative identification of glass-forming structural units in these glasses [5] [6] [7] [8] [9] [2] It is accepted that the network structure of the phosphate glasses contains a polymeric arrangement of PO_4 tetrahedra as postulated by Van Wazer [10], Martin (112) and Brow et al [113].

The bands arising from the vibrations of the phosphate glass network appear in the range $1400 - 400\ cm^{-1}$. Three main regions can be distinguished in this range; the region between $1400 - 1150\ cm^{-1}$ is characteristic of vibrations of non-bridging PO_2 groups, the region around $1150 - 900\ cm^{-1}$ is characteristic of terminal $P - O$ (and/or PO_3 groups) and the region between 900 and $700\ cm^{-1}$ is characteristic of the vibrations of bridging $P - O - P$ groups. All the symmetric and asymmetric stretching vibrations observed in the spectra are characteristic of Q^3 and Q^2 groups [13]. The first addition of alkali or alkaline earth oxides, such as Na_2O to P_2O_5 glass, result in conversion of three-dimensional network, to linear phosphate chain [14]. the linear chain structure results in cleavage of $P - O - P$ linkages and the creation of non-bridging oxygens (NBOs).

The IR spectra in Figure 4.12 shows a strong broad band near $1200 - 1360\ cm^{-1}$. The vibrational modes at peak center of $1353\ cm^{-1}$ is assigned to the stretching vibration of P = O in the branching group of $Q^3(PO_1O_{\frac{3}{2}})$ [15] [16]. This band exists in most phosphate glass system with at least $60\ mol\%\ P_2O_5$ [17] [18] [19] [20]. Several previous studies [21] [22] [23] have shown that the band corresponding to the stretching vibration of double bonded oxygen could be found in the frequency range $1230–1390\ cm^{-1}$. This band obviously becomes smaller with increasing $RE_2O_3(RE, = Er, Nd)$ concentration. In ultraphosphate glasses, this decrease is due to the

decrease in effective force constant of the ($P = O$) bond. The frequency of $P = O$ is also affected by the presence of water (which is probably taken up during the preparation of pellets for IR measurement) as in Figure 4.10. In all the glass samples measured, the absorption band $P - O - H$ was observed around $1650\ cm^{-1}$ [24] [25] [26], and the stretching mode of $P - O - H$ was also observed at $2700 - 2925\ cm^{-1}$ and $3433\ cm^{-1}$ [24] [26] [27].

The band near $1260 - 1280\ cm^{-1}$ is assigned to out-of-chain (PO_2) asymmetric stretching mode of two non-bridging oxygens bonded to phosphorus in the (middle group) Q^2 tetrahedral site. [28]. The vibrational mode at peak center $1270\ cm^{-1}$ was assign to asymmetric stretch mode of two non-bridging oxygens (NBO) bonded to the phosphorus atom, and at $1204\ cm^{-1}$ is symmetric stretching vibrational mode of the same unit in phosphate tetrahedra [17] [18] [15]. These two bands overlapped to form a broadened band in the spectra. The relative intensity of $P = O$ changes (decreases) with increasing the RE_2O_3 concentration, whereas the PO_2 band intensity increases with increasing the RE_2O_3 concentration. The peak center of $P = O$ band start shifting to high wavenumbers as x changes from 0.005 to 0.05.

. The absorption bands at $1000\ cm^{-1}$ and $1115 cm^{-1}$ are assign to the $P - O^-$ group, which is phosphate-non-bridging oxygen portion of the PO_4 tetrahedra. The absorption band at $1080 - 1120\ cm^{-1}$ of $P - O^-$ group shifts to lower wavenumber 1126 to $1110\ cm^{-1}$ as Er_2O_3 replaces Na_2O [20]. The absorption band at $896\ cm^{-1}$ and at $759\ cm^{-1}$ were assigned to asymmetric and symmetric stretch of $P - O - P$ linkage in the chain, respectively. [29]. The band for $(P - O - P)_{AS}$ shifts to lower wave-number by increasing the RE_2O_3 contents. Similar results for $(P - O - P)_{SS}$ were reported by Moustafa et al [2] at $725\ cm^{-1}$, and they assign this mode to symmetric stretch of $(P - O - P)$ ring, while at $908\ cm^{-1}$ is the $(P - O - P)_{AS}$ group linked

with linear metaphosphate chain [30]. Generally, the structure of $(P-O-P)_{SS}$ band is considered as the most characteristic one in the spectra of meta-phosphate since it appears in the frequency range free from other vibrational frequencies [31] [32]. In addition, $(P-O-P)_{SS}$ is very sensitive to changes in RE_2O_3 concentration, since the frequency strongly depend on the $(P-O-P)$ bond angle in the glass structure [32] [33] [29].

In previous observation [23], the shoulder at about $600\ cm^{-1}$ has been assigned to a covalent bond between non-bridging oxygen and erbium ions as $P-O-Er$ stretching vibration. The band $480-540\ cm^{-1}$ is assigned to deformation mode of PO_4^{3-} group [34] [35] [36] [37].The mode at $454\ cm^{-1}$ is assign to bending vibration of $O-P-\ O$ unit, $\delta(PO_2)$ mode of $(PO_n^-)_n$ chain group [2] [38]. All the symmetric and asymmetric stretching vibrations observed in the spectra are characteristic of Q^3 and Q^2 groups.

4.1.4 High Energy X-ray Diffraction (HEXRD) Measurements

X-ray diffraction experiments were performed on the beam line $11\ IDC$ at the Advance Photon Source (APS) at Argonne National Laboratory, Argonne IL.The incident photon energy was 114.80 keV (radiation wavelength, $0.010783\ nm$). Calibrations were carried out ,before data could be integrated from 2D to 1D [35].The polarization, self-scattering, Compton scattering, dark current and empty container background corrections were applied to measured data [36]. The total scattering function *S(Q)* is obtained by removing self-scattering$f^2(Q)$ and *C(Q)* is the Compton scattering contribution (given by $f^2(Q)+C(Q)$), from the coherent scattered intensity per atom, $I_X(Q)$ and dividing by the average squared atomic scattering factor, $\langle f^2(Q)\rangle^2$ according to [37-38].

$$S_X(Q) - 1 = \frac{I_x(Q) - (\sum_{i=1}^{n} f_i^2(Q) + C(Q))}{\langle f^2(Q)\rangle} \tag{4.1}$$

The average scattering is given by

$$\langle f^2(Q)\rangle = \left[\sum_{i,j=1}^{n} c_i f_i\right]^2 \tag{4.2}$$

where i and j represent the different atomic species in the material. The measured $S_X(Q)$ is expressed using Faber-Ziman formalism [39] as the sum of the X-ray weighted element specific partial structure factor $S_{ij}(Q)$

$$S_x(Q) - 1 = w_{ij}(Q)\left[S_{ij}(Q) - 1\right] \tag{4.3}$$

where $w_{ij}(Q)$ is the weighted functions of atoms i^{th} and j^{th} and follows the relation

$$w_{ij}(Q) = \frac{2c_i c_j f_i(Q) f_j(Q)}{\langle f^2(Q)\rangle} \quad i \neq j \tag{4.4}$$

$$w_{ij}(Q) = \frac{(c_i f_i(Q))^2}{\langle f^2(Q)\rangle} \quad i = j \tag{4.5}$$

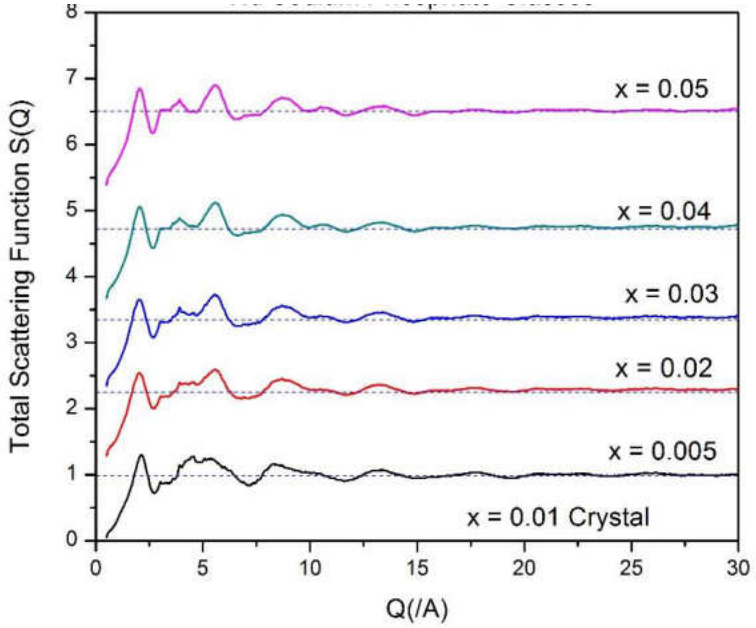

Figure 4.13(a): X-ray structure factors, S(Q) neodymium doped sodium phosphate glasses.

The structure factors, $S_X(Q)$ of $(RE_2O_3)_x(Na_2O)_y(P_2O_5)_{1-x-y}$ glasses $RE = Pr, Nd, Er$ are shown Figure 4.13.

(b)

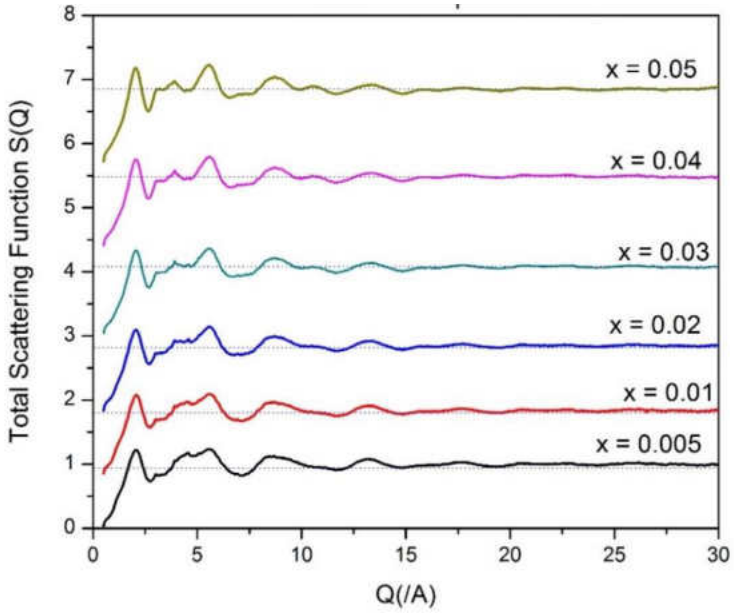

(c)

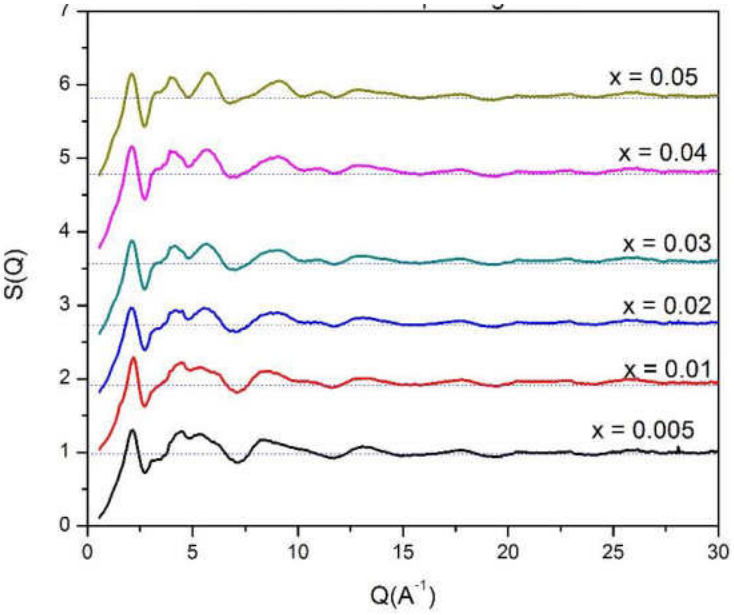

Figure 4. 13: X-ray structure factors, S(Q), of the $(RE_2O_3)_x(Na_2O)_y(P_2O_5)_{1-x-y}$ glasses. Graphs are shifted vertically for clarity. (a) Nd-doped glasses (b) Pr -doped glasses (c) Er-doped glasses. Systematic changes in S(Q) features in indicates structural changes induced by changes in rare earth oxide concentration.

4.1.4.1 Data Analysis and Results

Evaluation of the total pair distribution function $T_X(r$ was done using the Fourier transform,

$$T_x(r) = 2\pi^2 r\rho_0 + \int_{Q_{min}}^{Q_{max}} M(Q)[S(Q)-1]sin(Qr)dQ \tag{4.6}$$

where r is the separation between two given pairs of atoms, ρ_0 is the atomic density, and *M(Q)* is a Lorch window function [40] that suppresses Fourier transform termination effects according to

$$M(Q) = \frac{Sin\left(\frac{\pi Q}{Q_{max}}\right)}{\left(\frac{\pi Q}{Q_{max}}\right)} \tag{4.7}$$

Each atomic correlation was modeled by fitting a reciprocal space version of a Gaussian using an approach by Gaskell [41]

$$p_{ij}(Q) = N_{ij}\left(\frac{w_{ij}(Q)}{c_j}\right)\left(\frac{\sin(QR_{ij})}{QR_{ij}}\right)exp\left(-\frac{Q^2\sigma_{ij}^2}{2}\right) \tag{4.8}$$

Here N_{ij}, R_{ij} and σ_{ij}^2 are the coordination number, atomic seperation and Debye-Waller factors of atom *i* with respect to atom j respectively. c_j is the composition fraction of atom *j*. Initial fitting values of N_{ij}, R_{ij} and σ_{ij}^2 were taken from the those obtained for single rare-earth phosphate glasses. Refinement of the N_{ij}, R_{ij} and σ_{ij}^2 parameters were done using the NXFit program [42]. When using NXFit, it is not usual to fit $T_X(r)$ beyond 4 Å, because the problem of overlapping correlations makes it very difficult to assign features to particular pairs of atoms. The maximum number of iterations to be used in the fitting process can also be specified.Once satisfactory fits to the X-ray data-sets were achieved, the coordination numbers for each sample were altered, and the program was allowed to refit the data. The differences between the final values for the two fits

were then used as an estimate of the error [43]. $T_X(r)$ functions thus obtained (fits) are shown in in Figure 4.14 along with the experimental data. The structural parameters obtained from the X-ray data are given in Table 4.1. Examples of the modeling of the contributions of the individual atomic pair correlations to $T_X(r$ the model is shown in Figure 4.15.

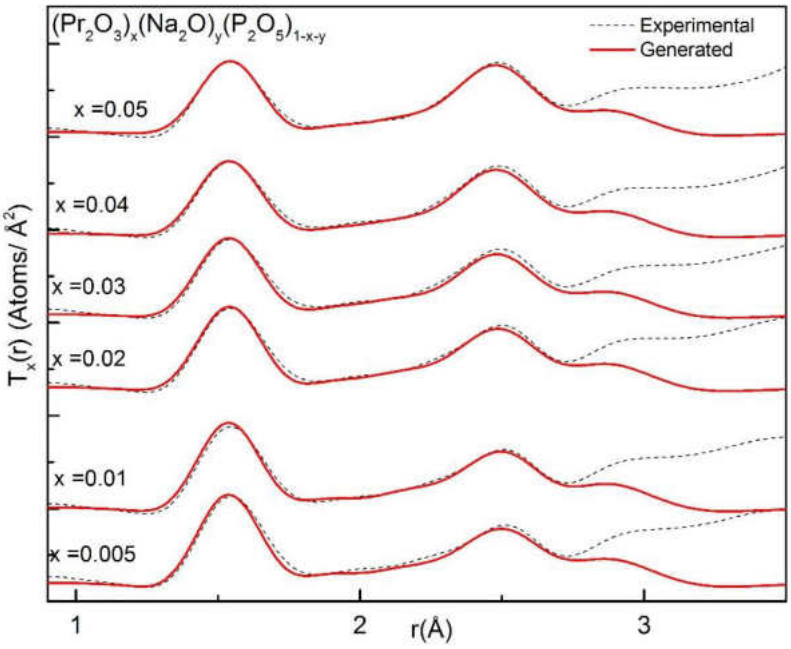

Figure 4.14 (a) : T(r) profile of for $(RE_2O_3)_x(Na_2O)_y(P_2O_5)_{1-x-y}$ *glasses, continue next page.*

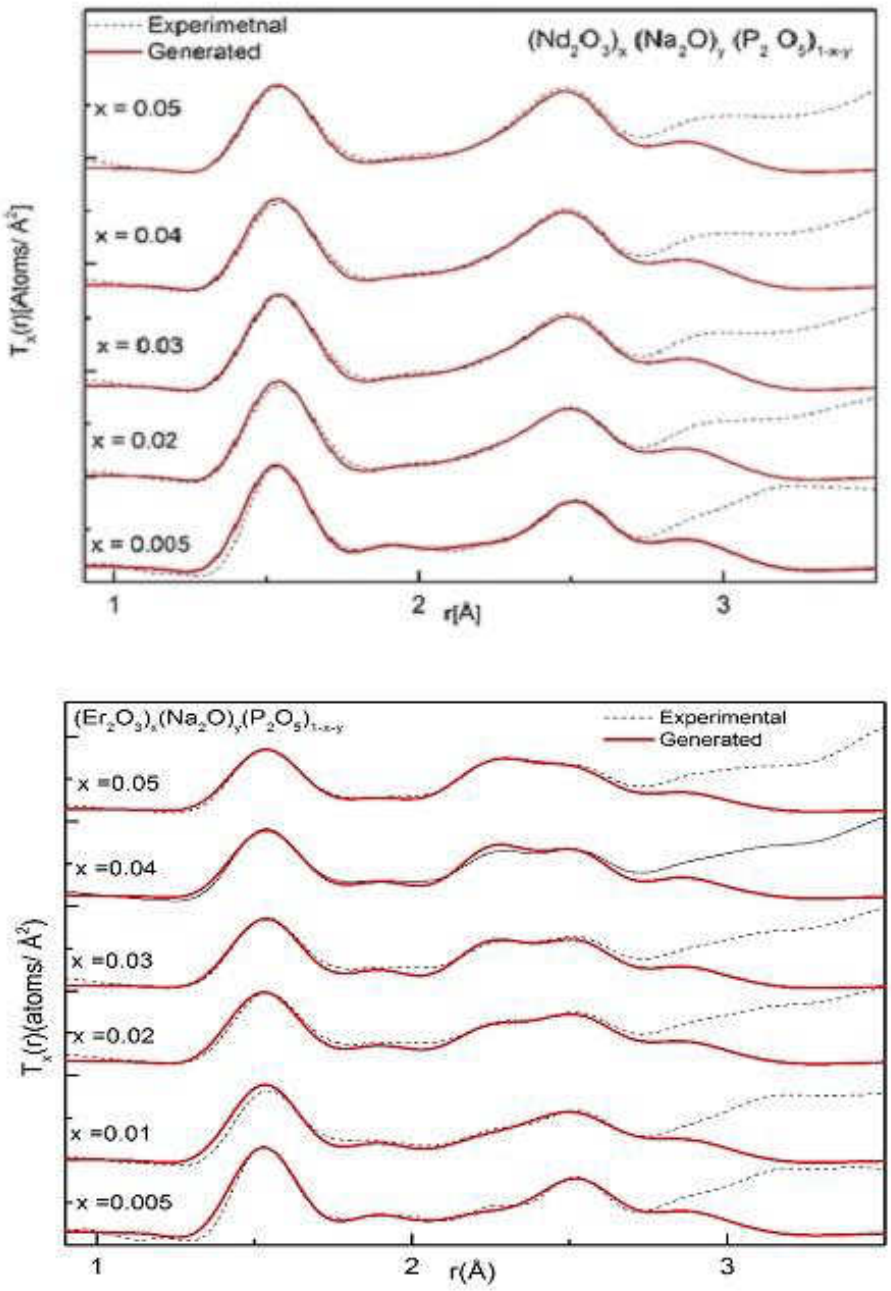

Figure 4. 14: $T_X(r)$ Profiles for $(RE_2O_3)_x(Na_2O)_y(P_2O_5)_{1-x-y}$ glasses, dotedt lines represent the experimental data, solid lines are the corresponding fits. $T_X(r)$ plots have been shifted vertically to avoid stacking.

Table 4. 1: Coordination number N_{ij}, atomic separation $\boldsymbol{R}(\text{Å})$ and Debye-Waller factor $\boldsymbol{\sigma^2}(\text{Å}^2)$ for each of the modeled pair correlation function for $(\boldsymbol{RE_2O_3})_x(\boldsymbol{Na_2O})_y(\boldsymbol{P_2O_5})_{1-x-y}$ glasses (RE = Pr , Nd, Er) where $0.005 \leq x \leq 0.05$ based on x-ray diffraction data. N_{ij}^* and R^* are the total coordination numbers and the mean distances, respectively.

Table 4.1 (a) Pr doped sodium phosphate glasses.

x	y	$P - O_T$			$P - O_B$			$(P-O)^*$		$Al - O$
(molar fraction)		N	$R(\text{Å})$	$\sigma^2(\text{Å}^2)$	N	$R(\text{Å})$	$\sigma^2(\text{Å}^2)$	N	$R(\text{Å})$	$R(\text{Å})$
0.005	0.395	1.90	1.49	0.05	1.94	1.58	0.037	3.83	1.535	1.81
0.01	0.39	1.90	1.49	0.05	1.91	1.58	0.034	3.81	1.535	1.81
0.02	0.38	1.85	1.49	0.055	2.0	1.58	0.039	3.85	1.535	1.81
0.03	0.37	1.90	1.49	0.055	2.0	1.58	0.044	3.90	1.535	1.81
0.04	0.36	1.90	1.49	0.055	2.1	1.58	0.045	4.0	1.535	1.81
0.05	0.35	1.90	1.49	0.055	2.1	1.58	0.03	4.0	1.535	1.81

$Na - O$			$Pr - O$			$O - O$			$P - P$		
N	$R(\text{Å})$	$\sigma^2(\text{Å}^2)$	N	$R(\text{Å})$	$\sigma^2(\text{Å}^2)$	N	$R(\text{Å})$	$\sigma^2(\text{Å}^2)$	N	$R(\text{Å})$	$\sigma^2(\text{Å}^2)$
5.0	2.38	0.165	7.90	2.43	0.092	4.20	2.52	0.088	2.0	2.87	0.13
5.0	2.36	0.17	7.84	2.42	0.11	4.22	2.52	0.08	2.0	2.87	0.13
5.0	2.35	0.17	7.78	2.45	0.099	4.25	2.52	0.093	2.0	2.87	0.12
4.94	2.32	0.22	7.55	2.43	0.102	4.35	2.52	0.088	2.0	2.87	0.13
5.0	2.34	0.18	7.52	2.45	0.11	4.30	2.52	0.094	2.0	2.87	0.12
5.0	2.34	0.18	7.48	2.45	0.11	4.34	2.52	0.093	2.0	2.87	0.11

Table 4.1 (b): Nd doped sodium phosphate glasses.

x	*y* (molar fraction)	$P - O_T$			$P - O_B$			$(P-O)^*$		$Al - O$
		N	$R(\text{Å})$	$\sigma^2(\text{Å}^2)$	N	$R(\text{Å})$	$\sigma^2(\text{Å}^2)$	N	$R(\text{Å})$	$R(\text{Å})$
0.005	*0.395*	*1.90*	*1.49*	*0.045*	*1.90*	*1.58*	*0.04*	*3.80*	*1.535*	*1.81*
0.01	*0.39*	*Crystal*								
0.02	*0.38*	*1.90*	*1.49*	*0.045*	*1.95*	*1.59*	*0.055*	*3.85*	*1.54*	*1.81*
0.03	*0.37*	*1.90*	*1.49*	*0.055*	*1.95*	*1.59*	*0.06*	*3.85*	*1.54*	*1.81*
0.04	*0.36*	*1.90*	*1.49*	*0.05*	*1.90*	*1.59*	*0.064*	*3.80*	*1.54*	*1.81*
0.05	*0.35*	*1.90*	*1.49*	*0.055*	*1.90*	*1.59*	*0.067*	*3.80*	*1.54*	*1.81*

$Na - O$			$Nd - O$			$O - O$			$P - P$		
N	$R(\text{Å})$	$\sigma^2(\text{Å}^2)$	N	$R(\text{Å})$	$\sigma^2(\text{Å}^2)$	N	$R(\text{Å})$	$\sigma^2(\text{Å}^2)$	N	$R(\text{Å})$	$\sigma^2(\text{Å}^2)$
5.0	*2.38*	*0.16*	*7.90*	*2.43*	*0.10*	*4.20*	*2.52*	*0.074*	*2.0*	*2.87*	*0.14*
Crystal											
4.94	*2.36*	*0.11*	*7.83*	*2.41*	*0.13*	*4.20*	*2.52*	*0.071*	*2.0*	*2.87*	*0.14*
4.90	*2.36*	*0.11*	*7.75*	*2.41*	*0.12*	*4.24*	*2.52*	*0.072*	*2.0*	*2.86*	*0.14*
5.0	*2.36*	*0.11*	*7.71*	*2.41*	*0.10*	*4.25*	*2.52*	*0.072*	*2.0*	*2.86*	*0.14*
5.0	*2.36*	*0.11*	*7.51*	*2.42*	*0.088*	*4.35*	*2.52*	*0.072*	*2.0*	*2.86*	*0.14*

Table 4.1(c) : Er doped sodium phosphate glasses.

x	y	$P - O_T$			$P - O_B$			$(P-O)^*$		$Al - O$
(molar fraction)		N	R(Å)	σ^2(Å^2)	N	R(Å)	σ^2(Å^2)	N	R(Å)	R(Å)
0.005	0.395	1.90	1.49	0.021	1.98	1.58	0.037	3.88	1.535	1.82
0.01	0.39	1.90	1.49	0.05	1.91	1.58	0.045	3.8	1.535	1.81
0.02	0.38	1.85	1.49	0.055	1.91	1.58	0.057	3.81	1.535	1.84
0.03	0.37	1.90	1.49	0.055	1..9	1.58	0.044	3.80	1.535	1.81
0.04	0.36	1.90	1.49	0.047	2.1	1.58	0.042	4.0	1.535	1.84
0.05	0.35	1.90	1.49	0.048	1.91	1.58	0.043	3.81	1.535	1.81

$Na - O$			$Er - O$			$O - O$			$P - P$		
N	R(Å)	σ^2(Å^2)	N	R(Å)	σ^2(Å^2)	N	R(Å)	σ^2(Å^2)	N	R(Å)	σ^2(Å^2)
5.0	2.4	0.13	8.0	2.25	0.13	4.20	2.53	0.065	2.0	2.84	0.14
4.83	2.4	0.13	7.85	2.26	0.11	4.20	2.52	0.086	2.0	2.84	0.14
5.0	2.40	0.134	7.72	2.26	0.08	4.21	2.52	0.070	2.0	2.84	0.14
4.80	2.40	0.11	7.45	2.25	0.07	4.35	2.52	0.062	2.0	2.84	0.14
4.89	2.39	0.11	7.25	2.27	0.074	4.25	2.52	0.041	2.0	2.84	0.14
4.89	2.39	0.10	7.0	2.27	0.085	4.25	2.52	0.06	2.0	2.84	0.14

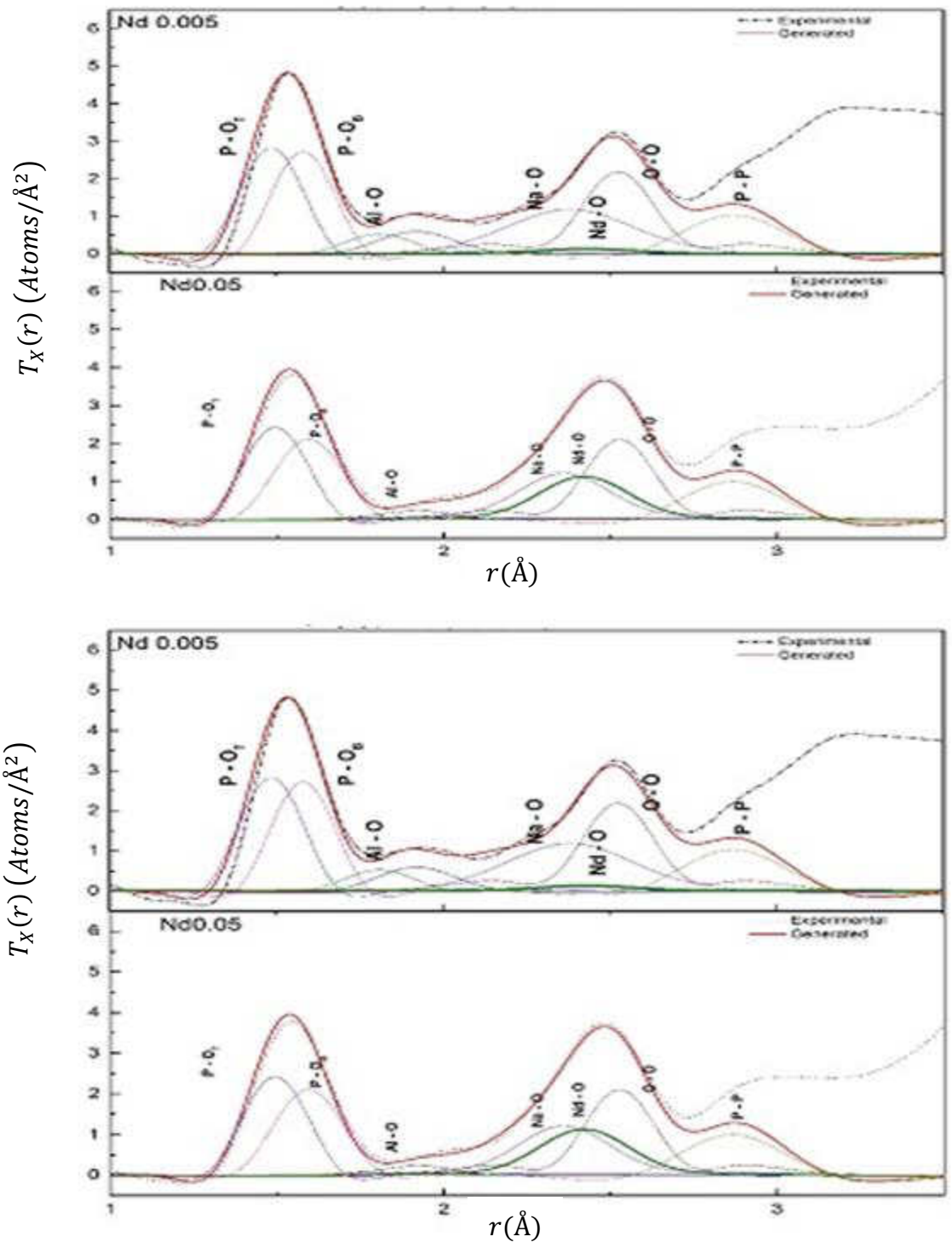

Figure 4. 15: Examples of the modeling of the contributions of the individual atomic pair correlations to the model for (a) Pr (top x = 0.005, bottom x =0.05) and (b) Nd (top = 0.005, bottom x =0.05) doped glasses.

4.1.5 Optical Properties

4.1.5.1 Absorption Properties

The optical absorption spectra of $(x = 0.01)$ $Er^{3+}$and Nd^{3+}-doped sodium phosphate glasses measured in the UV-visible (VIS) and NIR region, are shown in Figures 4.16 - 4.18.

4.1.5.1.1 Erbium Doped Sodium Phosphate Glasses

A total of 13 absorption bands, corresponding to transitions from the ground state, $^4I_{15/2}$ to various excited states, were identified and assigned. The assignments were made by comparison with energy levels of Er^{3+}Aqueous ion [39], and reported Er^{3+} in Glass System [40] [41] [42] [43] [44]. The peak positions (bary-centers) of the absorption bands (in nanometer) and, their experimental (f_{exp})) and calculated (f_{cal}) oscillator strengths were obtained using well-known expressions [45] [46].

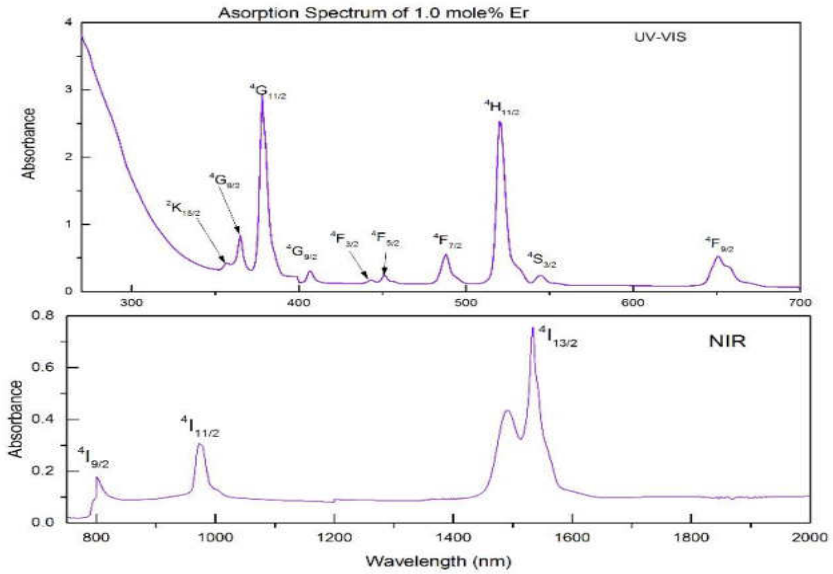

Figure 4. 16 : Absorption spectra of (x = 0.01) Er^{3+} -doped sodium Phosphate glass (a) UV-VIS (top) and (b) NIR regions (bottom). The band assignments are transitions from the ground state $^4I_{15/2}$.

The absorption bands $^4I_{15/2} \rightarrow {}^4G_{11/2}$ and $^4I_{15/2} \rightarrow {}^4H_{11/2}$ located at $377\ nm$ and $520\ nm$, respectively are most intense and are called hypersensitive transitions (HSTs) [47] [48]. The HSTs are sensitive to small changes of environment around RE^{3+} ions [137] and follow the selection rules $|\Delta S| = 0, |\Delta L| \leq 2\ and\ |\Delta J| \leq 2$ [48].

The Absorbance coefficient $\alpha(\lambda)$ was calculated using the Beer- Lambert's Law given by

$$\alpha(cm^{-1}) = \frac{2.303}{L} \times A \qquad (4.9)$$

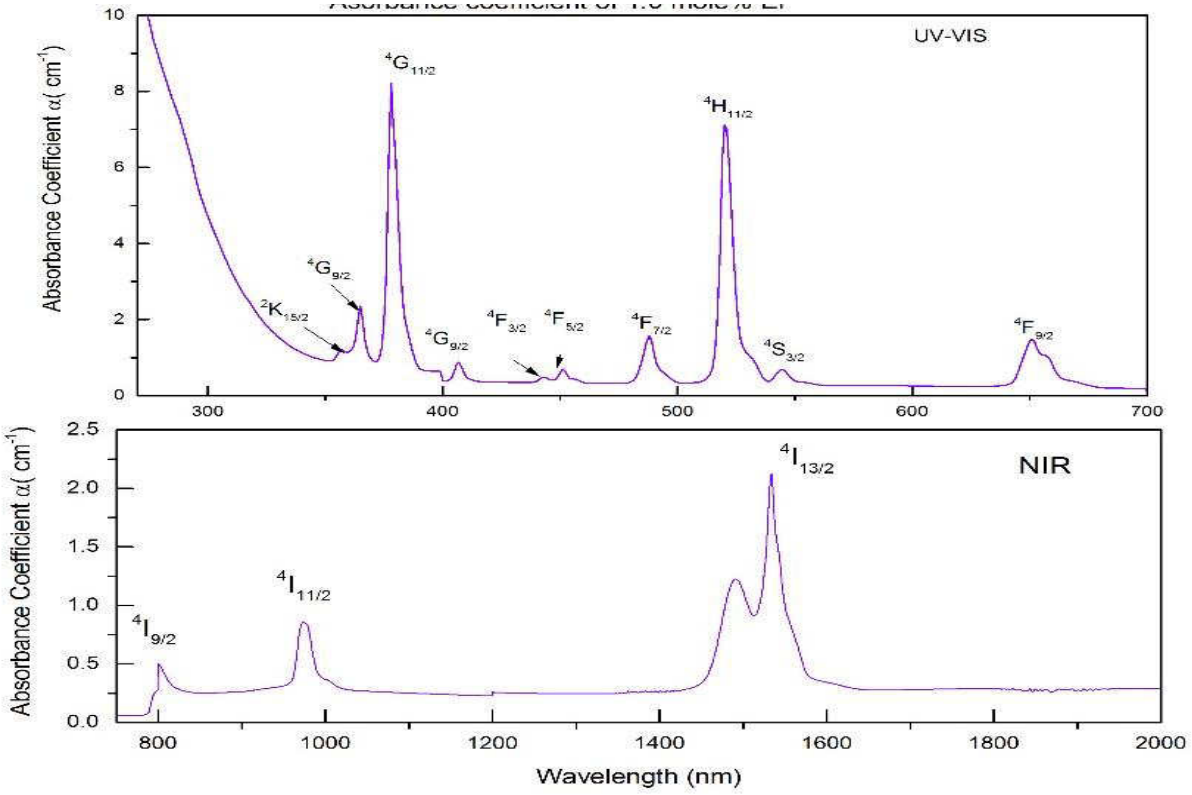

Figure 4. 17 : Absorbance coefficient of (x =0.01) Er^{3+} -doped sodium phosphate glass (a) UV-VIS region (top) and (b) NIR regions (bottom). The thickness of the sample is 0.8 cm.

The Absorbance cross-section of Er^{3+} was calculated using the relation [49]

$$\sigma(\lambda) = \frac{\alpha(\lambda)}{N} \tag{4.10}$$

where N is the concentration of Er^{3+} ions in the sample.

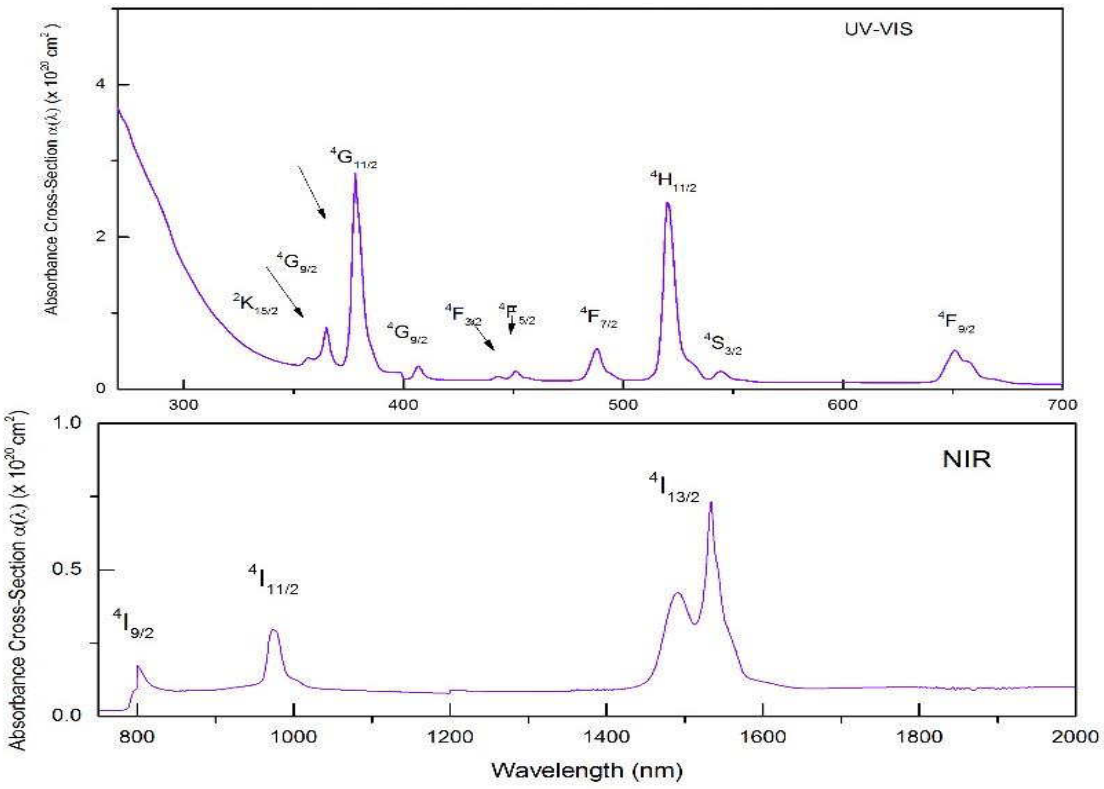

Figure 4. 18 : Absorbance cross-section of (x =0.01) Er^{3+} -doped sodium phosphate glass with (a) UV-VIS(top) and (b) NIR regions(bottom). The concentration of Er^{3+} ions in the sample is $N = 2.90 \times 10^{20} \frac{ions}{cm^3}$.

4.1.5.2 Calculations of Judd-Ofelt Parameters

The Judd-Ofelt (JO) theory [45] [46] is based on the static, free-ion and single configuration approximation. In this static model, the central ion is affected by the surrounding host ions via a static

electric field, referred to as ligand or crystal field, and is treated as a perturbation on the free-ion Hamiltonian. The schematic diagram of JO analysis is shown in Figure 4.19.

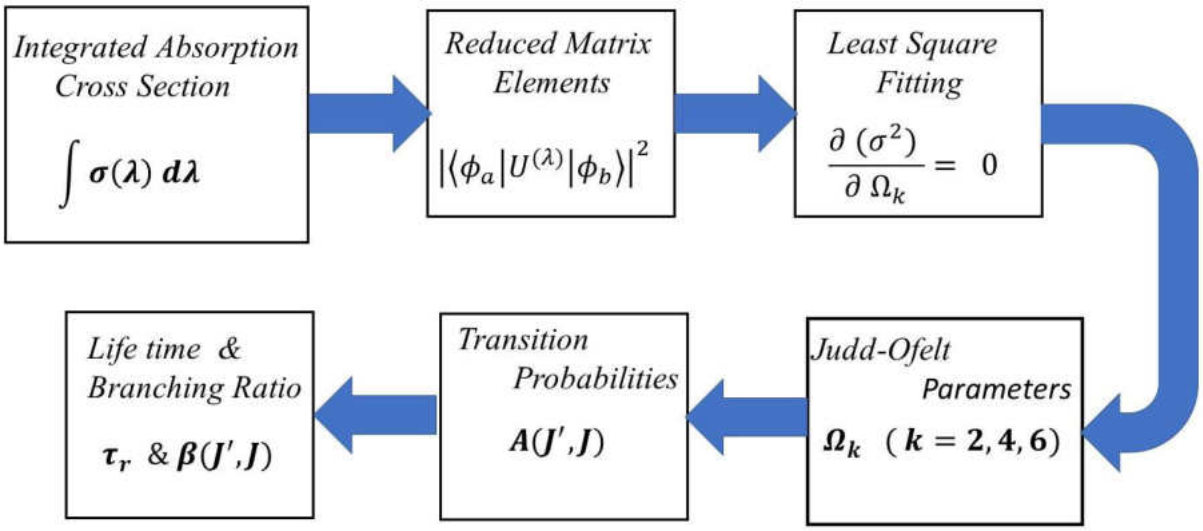

Figure 4. 19 : Schematic diagram for JO program analysis.

JO theory describes the intensities of lanthanide and actinide transitions in solid and solutions. The utility of the JO theory is that it provides a theoretical expression for the line strength.

$$S_{ED} = \sum_{t=2,4,6} \Omega_t |\langle f^n[SL]J||U^t||f^n[S'L']J'\rangle|^2 \qquad (4.11)$$

$$S_{cal}(J \rightarrow J') = \Omega_2 |U^2|^2 + \Omega_4 |U^4|^2 + \Omega_6 |U^6|^2 \qquad (4.12)$$

Here Ω_t are the Judd-Ofelt parameters. The terms in brackets are doubly reduced matrix elements for intermediate coupling [48]. Intermediate coupling refers to a situation where the mutual repulsion interaction between $4f$ electrons is of the same order of magnitude as the spin-orbit coupling. This effect can be incorporated by expanding the wave-function of the $4f$ states in a linear combination of Russel - Saunders or $LS - coupled$ states. The U^t are the irreducible tensor forms of the dipole

operator, the data for Er^{3+} and $Nd^{3+}$are from reference [6]. A Judd-Ofelt analysis relies on accurate absorption measurements, specifically the integrated absorption cross-section over the wavelength range of several manifolds. From the integrated absorption cross-section, the so-called line strength $S_{measured}$ can be expressed as

$$S_{mea} = \frac{3ch}{8\pi^3 e^2 \bar{\lambda}} \ (2J+1)n \left(\frac{3}{n^2+2}\right)^2 \int \sigma(\lambda) d\lambda \qquad (4.13)$$

where J is the total angular momentum of the initial ground manifold, found from the $^{2S+1}L_J$ designation. $\sigma(\lambda)$ is the absorption cross-section as a function of wavelength. The factor $(\frac{3}{n^2+2})^2$represents the local field correction for electric dipole transition for the effective field for the ion in the dielectric host medium of isotropic refractive index n. The wavelength -dependent index of refraction was determined from Sellmeier's dispersion equation and plotted in Figure 4.20 [50] .

$$n^2(\lambda) = 1 + \frac{S\,\lambda^2}{\lambda^2 - \lambda_0^2} = A + \frac{B\,\lambda^2}{\lambda^2 - C} \qquad (4.14)$$

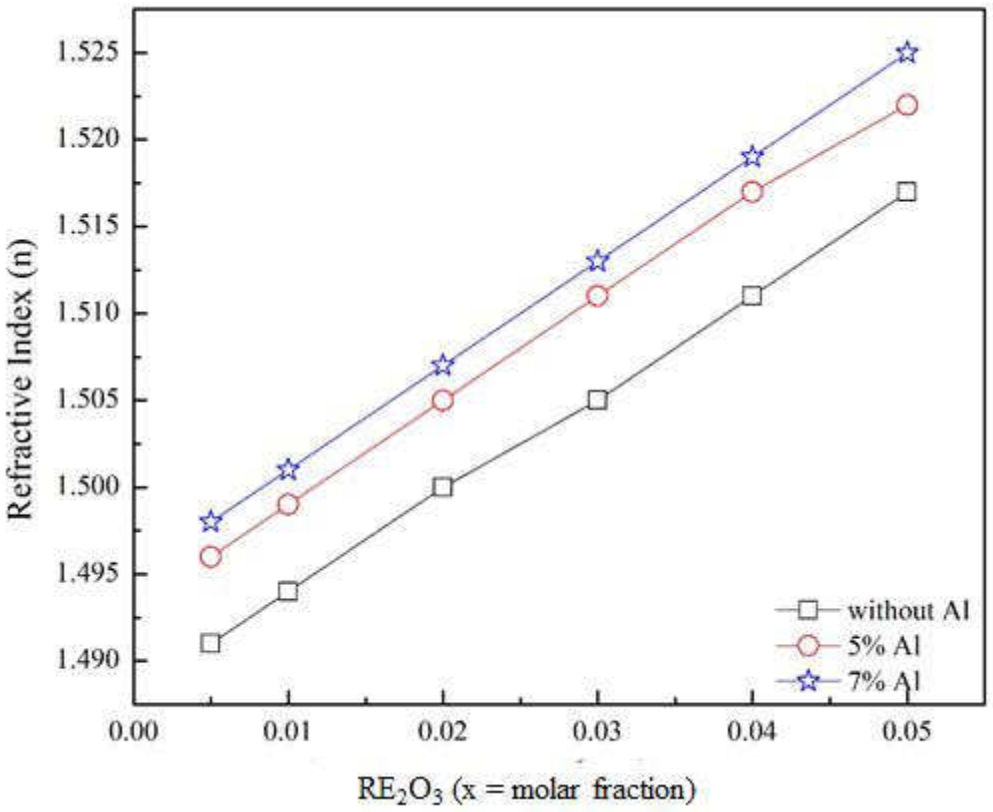

Figure 4. 20: Refractive index of erbium sodium phosphate samples calculated using Sellmeier's relationship and sciglass software data [51]*, estimated values of Sellimeier coefficients A = 1, B = 1.28400, C = 0.01016 for n = 1.513.* [52]

The mean wavelength $\bar{\lambda}$ and bandsum can be found from the absorption cross section data using relationship shown in Equations 4.15 and 4.16 (see below) and are given in Table :4.1 for Er^{3+} doped sodium phosphate glasses

$$\bar{\lambda} = \frac{\sum \lambda\, \sigma(\lambda)}{\sum \sigma(\lambda)} \tag{4.15}$$

$$bandsum\ (cm^2 - nm) = \frac{\int_{manifold} \sigma(\lambda) d\lambda}{1 \times 10^{20}} \tag{4.16}$$

Table 4. 2 : Bandsum and mean wavelength for (x = 0.01) erbium from absorption cross section shown in Figure 4.18.

No	*Transition from* $^4I_{15/2}$	*Bandsum* (cm^2 *-nm /1* $\times 10^{20}$)	$\bar{\lambda}$ *(nm)*
1	$^4I_{13/2}$	*40.71*	*1529*
2	$^4I_{11/2}$	*10.63*	*988.4*
3	$^4I_{9/2}$	*2.07*	*814.70*
4	$^4F_{9/2}$	*9.09*	*656.7*
5	$^4S_{3/2}$	*2.52*	*551.4*
6	$^2H_{11/2}$	*20.34*	*522.1*
7	$^4F_{7/2}$	*4.56*	*488.5*
8	$^4F_{5/2}$	*2.27*	*451.3*
9	$^4F_{3/2}$	*0.385*	*443.48*
10	$^2G_{9/2}$	*1.70*	*409.7*
11	$^2G_{11/2}$	*16.30*	*378*
12	$^4G_{9/2}$	*2.95*	*364.7*
13	$^2K_{15/2}$	*0.78*	*356*

4.1.5.3 Absorption Spectra of Neodymium Doped Sodium Phosphate Glasses

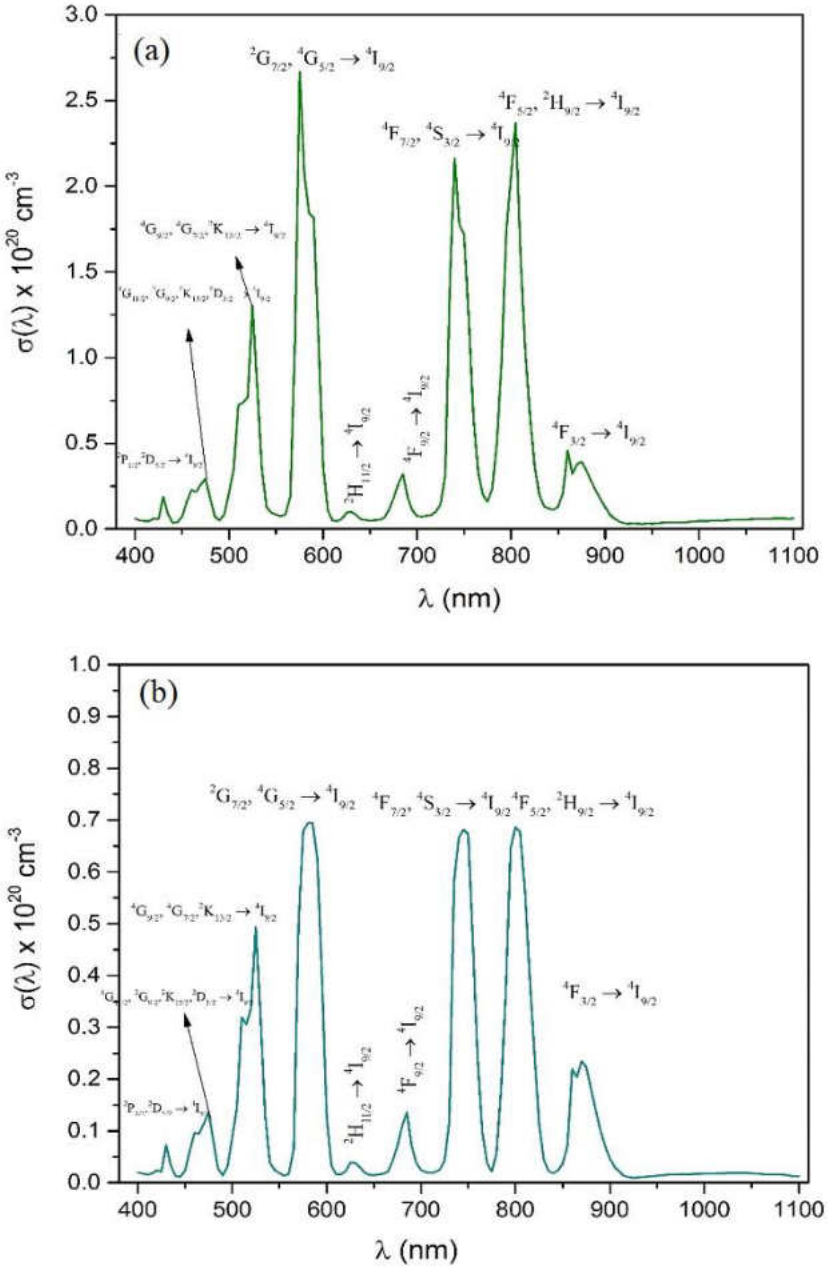

Figure 4. 21 : Absorption Cross Section of N d^{3+} -doped sodium phosphate glasses (a) x =0.092 molar fraction with concentration of Nd^{3+} $N = is\ 2.90 \times 10^{20} \frac{ions}{cm^3}$ (b) x = 0.03 molar fraction with concentration of Nd^{3+} $N = 4.08 \times 10^{20} \frac{ions}{cm^3}$.

4.1.5.4 Life-time Measurements

4.1.5.4.1 Erbium Doped Sodium Phosphate Glasses

Luminescence decay measurements were performed at University of South Dakota (USD), Vermilion, SD, for Er^{3+} and Nd^{3+}doped sodium phosphate glasses. For erbium doped samples were excited with a 522 nm laser, which excite Er^{3+} ions to state $^4S_{3/2}$ level. The luminescence decay of Er^{3+} ions from $^4I_{13/2} \rightarrow {}^4I_{15/2}$ transition at 1530 nm was observed. The Diekes diagram [53] of these transitions are shown in Figure 4.22.

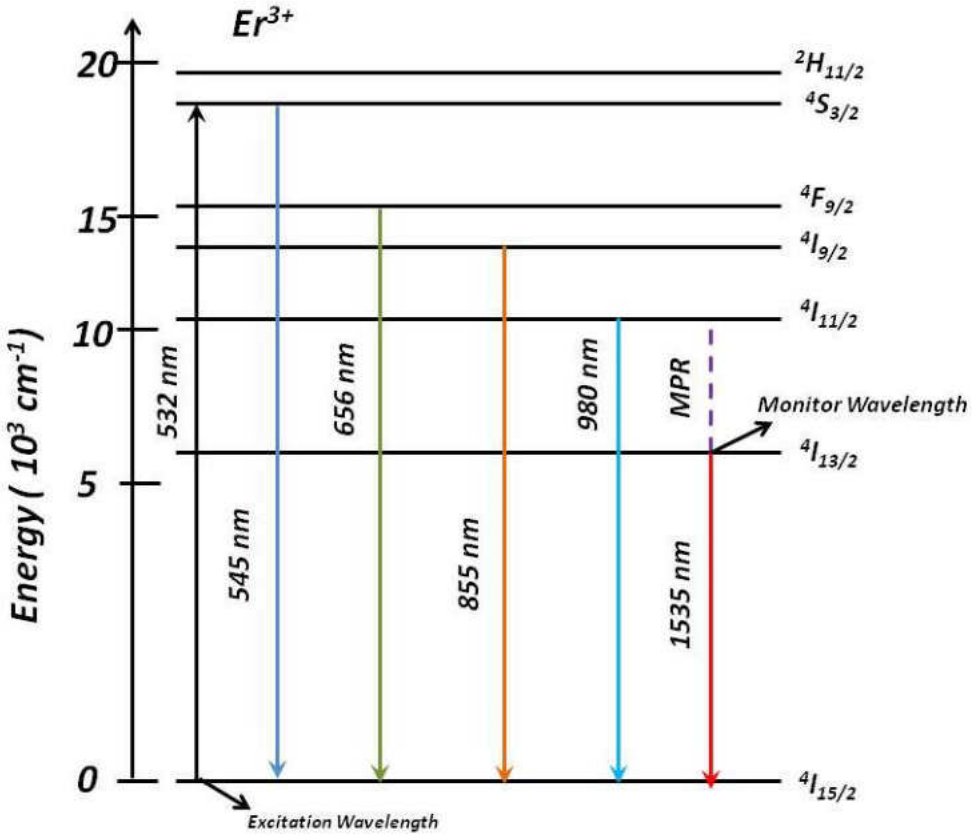

Figure 4. 22: Dieke diagram of Er ion energy level in glasses excited with 522 nm excitation laser.

The decay curve of level ${}^4I_{13/2}$ for all the erbium samples were exponential and they were fitted with the following expression [54]

$$I = I_0 \exp\left(-\frac{t}{\tau}\right) \tag{4.17}$$

where I_0 is the intensity at $t = 0$. The lifetime $\tau = (\Gamma + k_{nr})^{-1}$ contains the emissive rate Γ and non-radiative decay rate k_{nr} as shown in Figure 4.23.

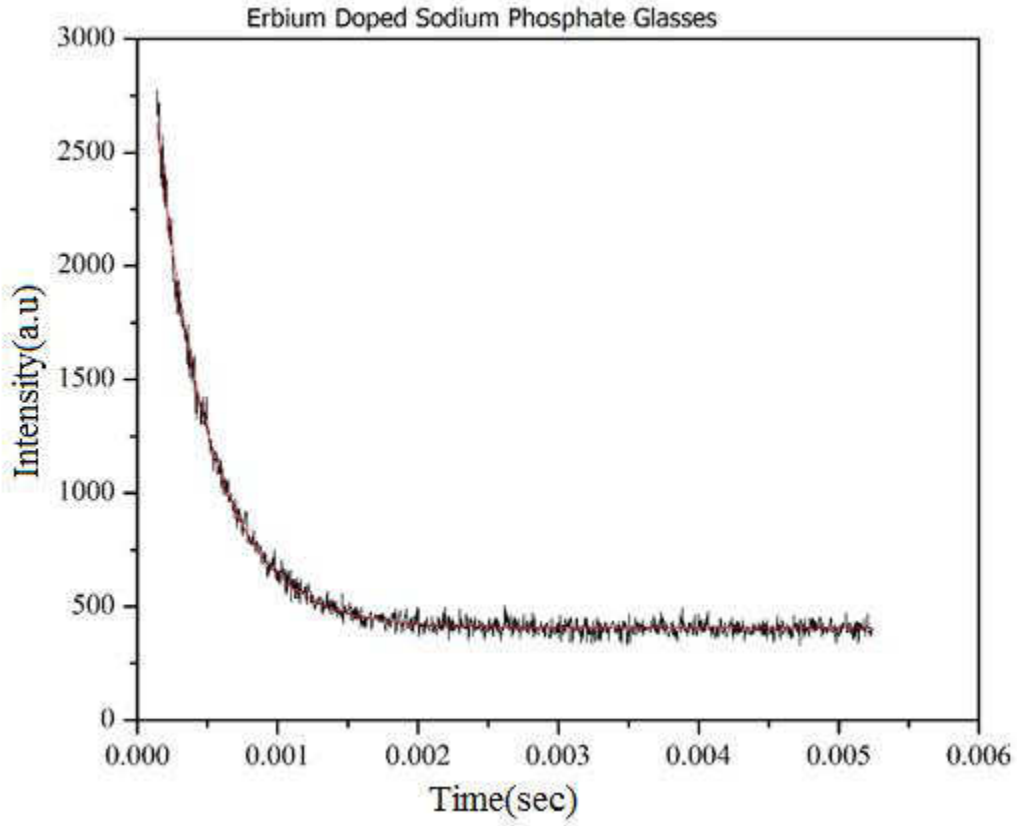

Figure 4. 23: Exponential decay curve of ${}^4S_{3/2}$ level monitored at ${}^4I_{13/2} \rightarrow {}^4I_{15/2}$ for erbium doped sodium phosphate glass.

From these decay curves, the effective decay time τ_{eff}, which is considered as the experimental lifetime τ_{exp} have been determined by the following expression [55].

$$\tau_{exp} = \frac{\int t\, I(t) dt}{\int I(t) dt} \tag{4.18}$$

The concentration of the rare-earth ions is an important parameter, which effects the laser gain of the host material. The number density N of the laser-active ion i.e. the number of ions per cubic centimeter can be evaluated using the relation [56] [57]

$$N\left(\frac{ions}{cm^3}\right) = \frac{(Mole\ fraction\ of\ Re) N_A\, \rho}{(Glass\ Avderage\ molecular\ Weight)} = \frac{x\, \rho N_A}{M} \tag{4.19}$$

where ρ is the density of glass samples, N_A is the Avogadro's number, x is the mole fraction of the rare-earth oxide and M is the average molecular weight of the sample. The measured lifetime of the samples is shown in Figures 4.24 and 4.25 as a function of Er^{3+} ion concentration and molar fraction of Er_2O_3 respectively.

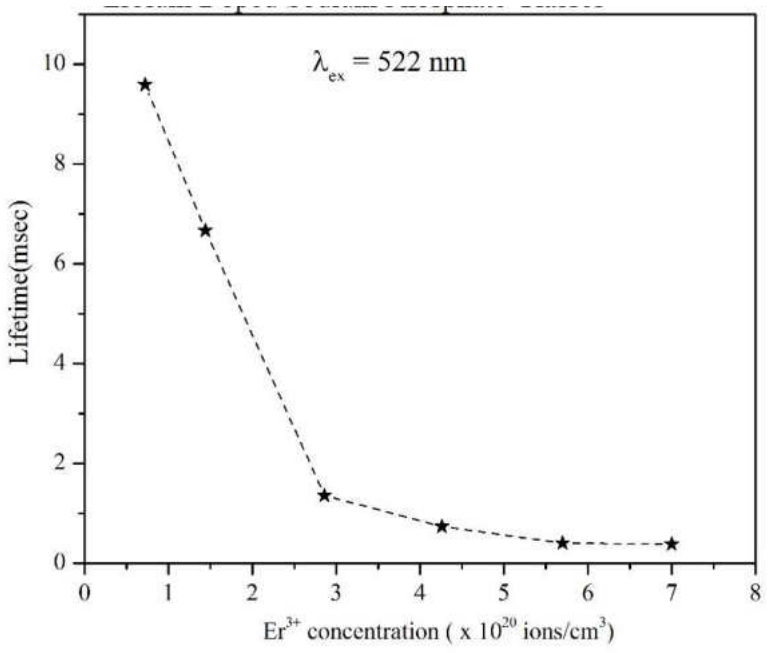

Figure 4. 24: Dependence of $^4I_{13/2}$ state lifetime on the Er^{3+} concentration.

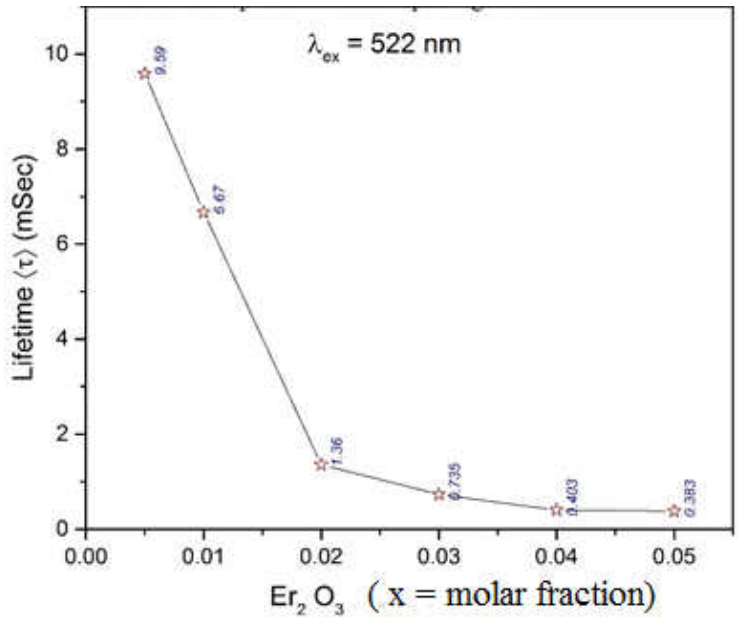

Figure 4. 25: Dependence of $^4I_{13/2}$ state lifetime on the molar fraction of Er_2O_3.

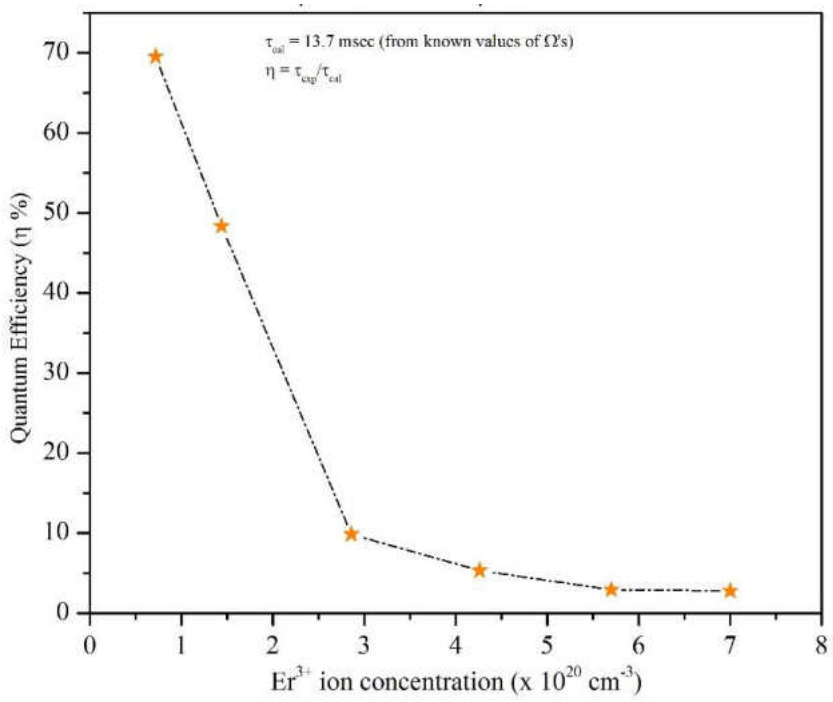

Figure 4. 26: Quantum efficiency with $\tau_r = 13.79\ msec$ of at $^4I_{13/2} \rightarrow {}^4I_{15/2}$transitions for various Er^{3+} concentration in sodium phosphate glasses.

The luminescence quantum efficiency η is defined as the ratio of the number of photons emitted to the number of photons absorbed. For rare earth ion systems, η is equal to the ratio of the measured lifetime to the predicted radiative lifetime for respective levels given by [58]

$$\eta = \left(\frac{\tau_{exp}}{\tau_r}\right) \times 100 \qquad (4.20)$$

Quantum efficiency of the $^4I_{13/2}$ level of erbium doped glasses in these shown in Figure 4.26.

4.1.5.4.2 Neodymium Doped Sodium Phosphate Glasses

Neodymium doped samples were also excited with 532 nm laser, which excite Nd^{3+} ions to state $^4G_{7/2}$level. The luminescence decay of Nd^{3+} ions from $^4F_{5/2} \rightarrow {}^4I_{11/2}$ transition at 1064 nm was observed. The Dieke diagram [53] of these transitions are shown in Figure 4.27.

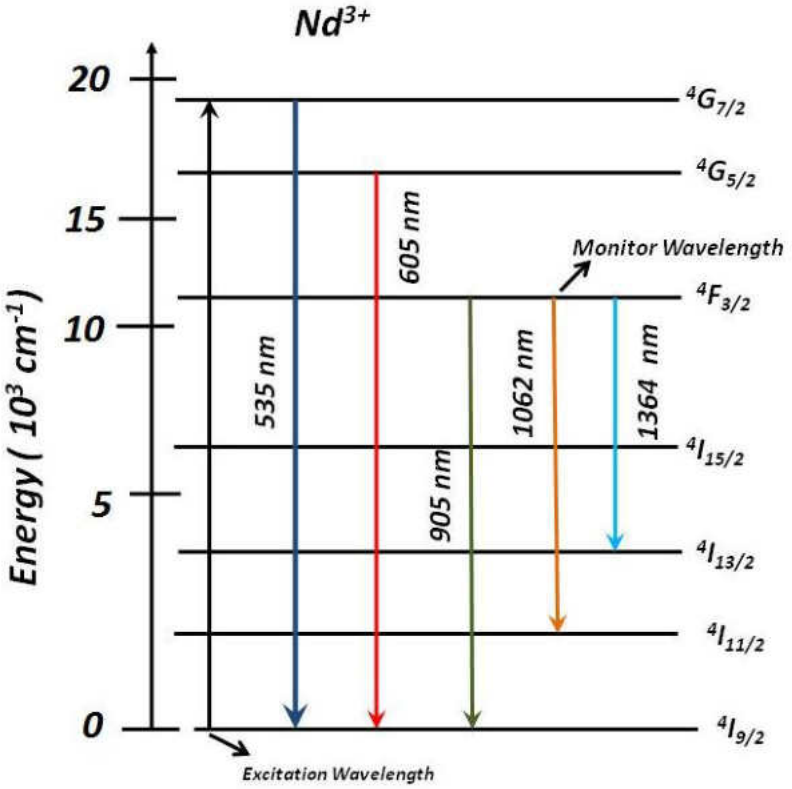

Figure 4. 27 : Energy level diagram of neodymium ion in sodium phosphate glasses.

The measured lifetime of the samples is shown in Figure 4.28 and 4.29 as a function of Nd^{3+} ion concentration and molar fraction of Nd_2O_3, respectively.

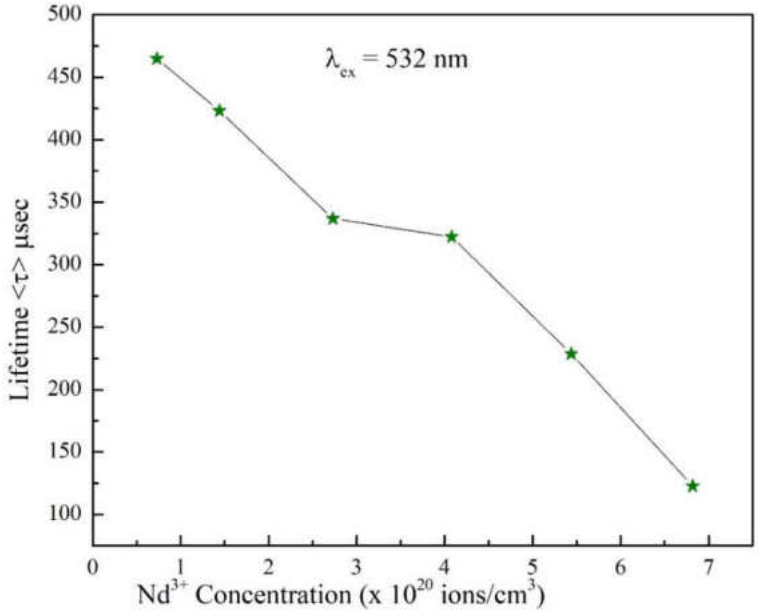

Figure 4. 28: Dependence of $^4F_{3/2}$ state lifetime on the Nd^{3+} concentration.

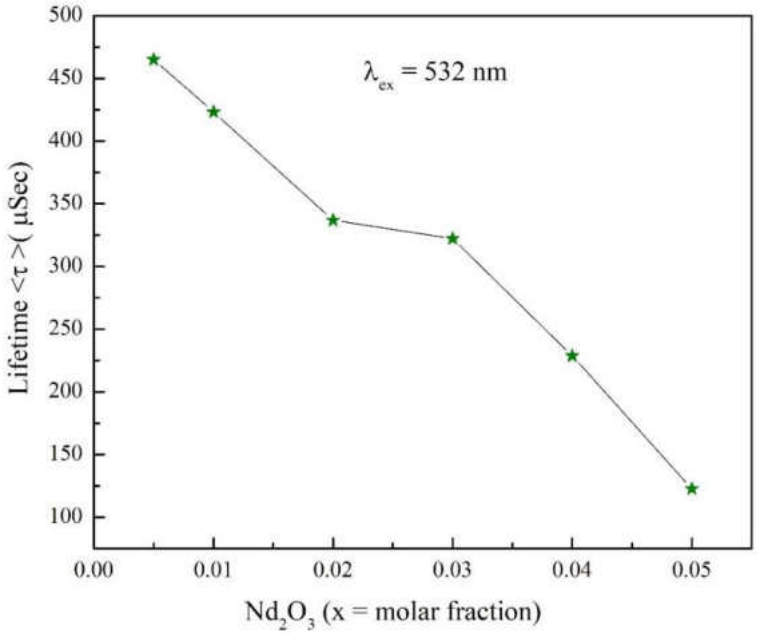

Figure 4. 29 : Dependence of $^4F_{3/2}$ state lifetime on the molar fraction Nd_2O_3 .

4.1.5.5 Emission Properties

4.1.5.5.1 Erbium Doped Sodium Phosphate glasses

For the evaluation of emission spectra with different Er^{3+} ion concentration, the emission was measured by exciting the glass samples with $522\ nm$ ($^4S_{3/2} \rightarrow {}^4I_{15/2}$) and $1064\ nm$ ($^4I_{11/2} \rightarrow {}^4I_{15/2}$) and monitoring the emission of $^4I_{13/2} \rightarrow {}^4I_{15/2}$ transition state. Among different Er^{3+} emission lines, the emission band at $1.53\ \mu m$ arising from $^4I_{13/2} \rightarrow {}^4I_{15/2}$transition is the most important one as it is useful for optical communication and Infrared (IR) laser applications [59]. The recorded emission spectra are shown in Figure 4.31.

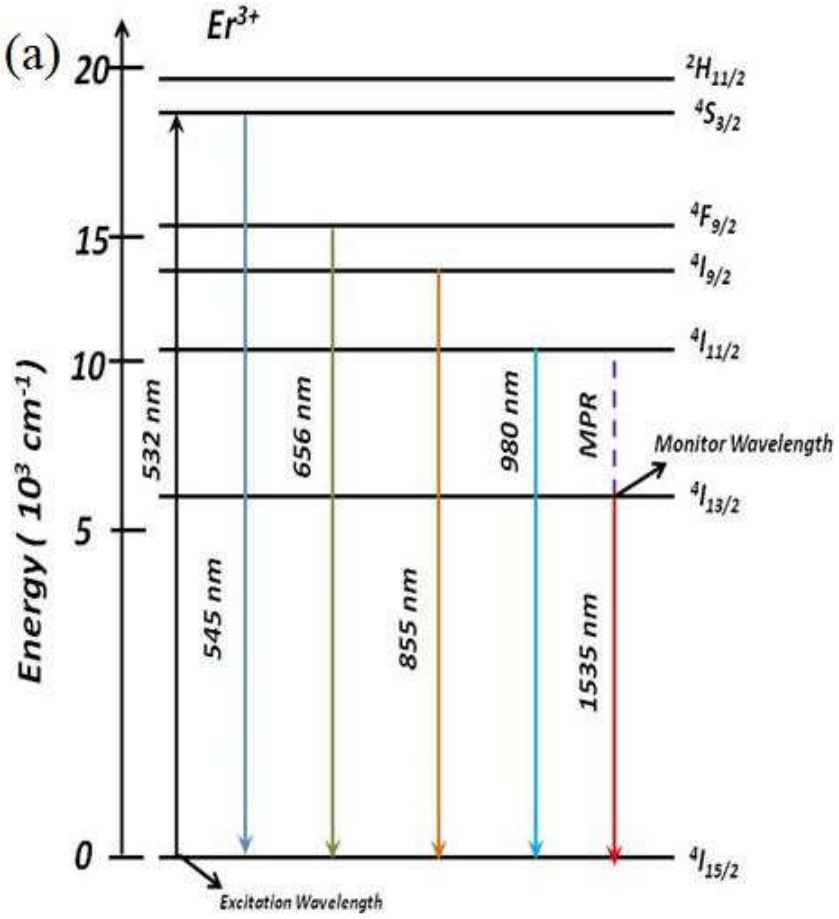

Figure 4. 30: Energy level diagram of Er^{3+} ion.

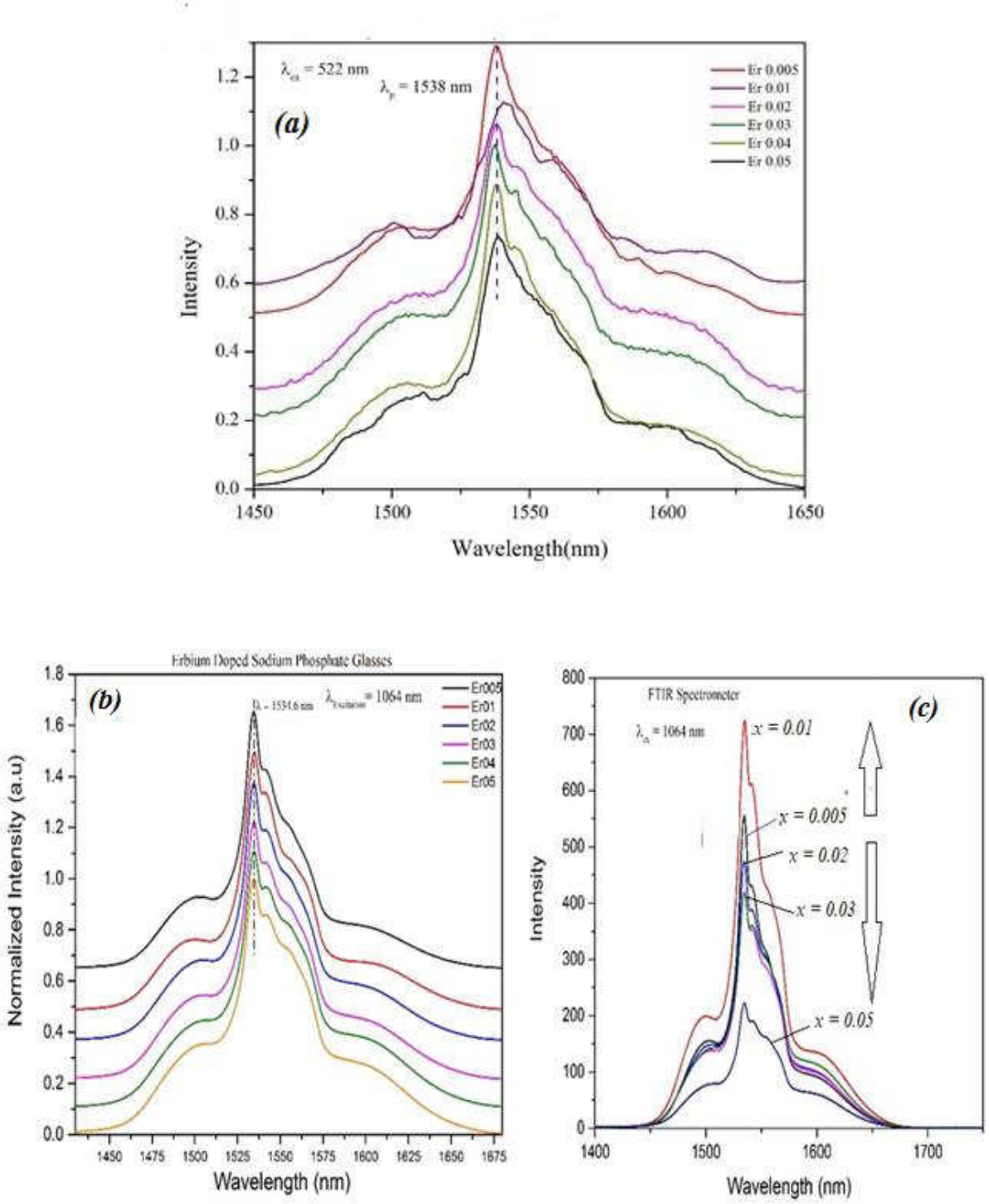

Figure 4. 31: Emission spectra of erbium doped samples (a) 522 nm excitation source (b) 1064 nm excitation and monitoring 1530 nm emission, plots are shifted for clarity (c) Dependence of intensity on concentration

4.1.5.5.2 Neodymium Doped Sodium Phosphate Glasses

The emission of Nd^{3+}ion was monitored at $1064\ nm\ (^4F_{3/2} \rightarrow {}^4I_{11/2})$ and $1325\ nm(^4F_{3/2} \rightarrow {}^4I_{13/2})$, by exciting the Nd^{3+} ions using $532\ nm\ (^4I_{9/2} \rightarrow {}^4G_{7/2})$ and $1064\ nm\ (^4I_{11/2} \rightarrow {}^4F_{3/2})$ lasers. The Recorded emission spectra of Nd^{3+} ions is shown in Figure 4.33.

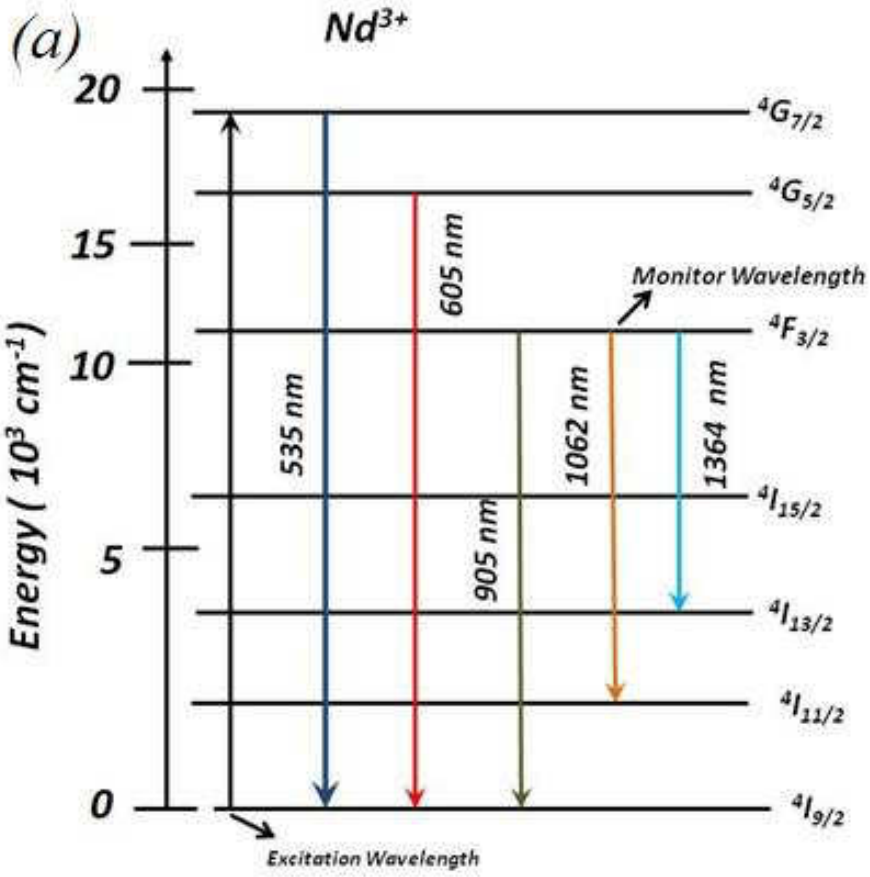

Figure 4. 32: Energy level diagram of Nd^{3+} ion.

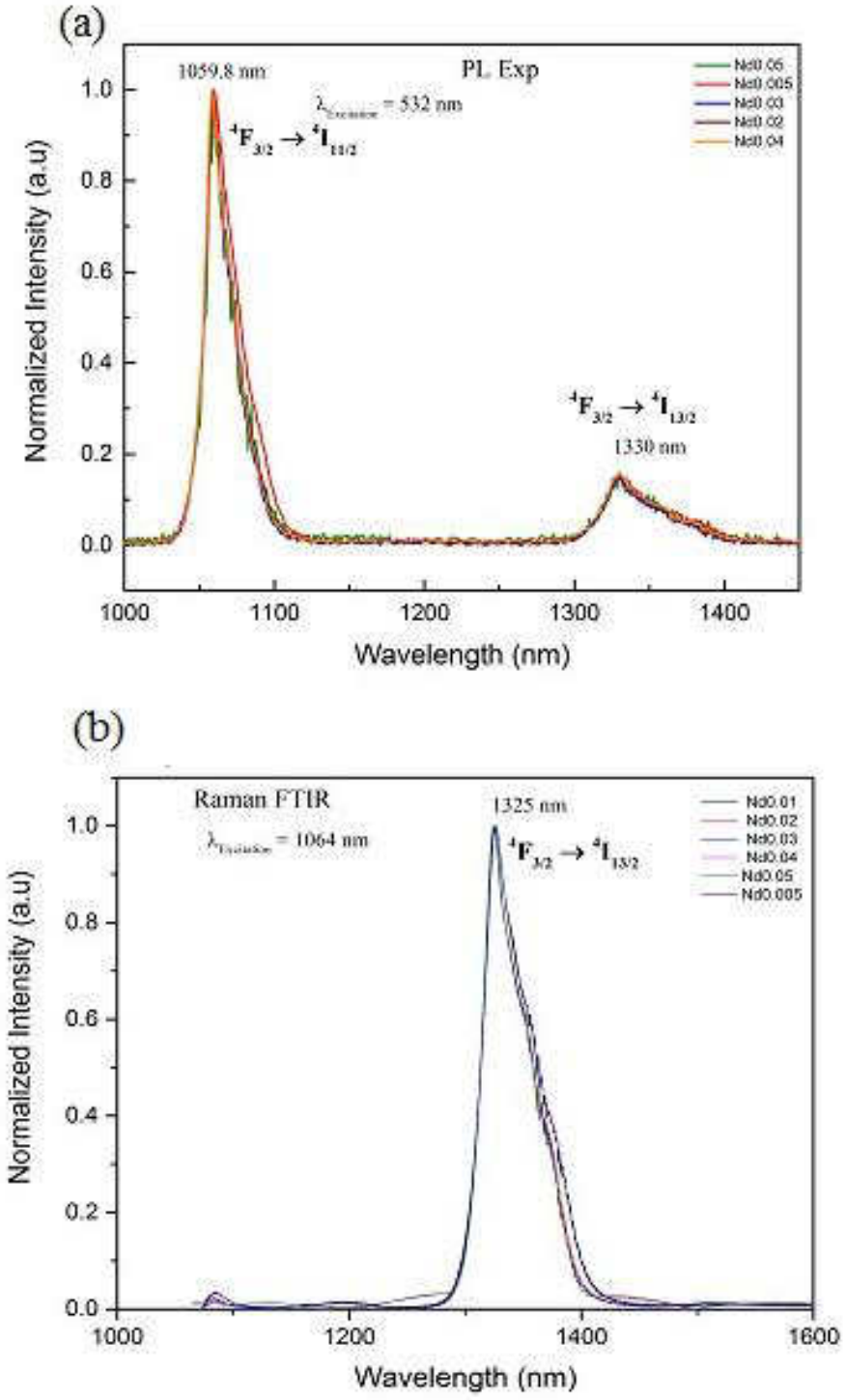

Figure 4. 33: Emission spectra of neodymium doped samples (a) 532 nm excitation source (b) 1064 nm excitation and monitoring 1064 nm and 1325 nm emission.

4.1.5.5.3 Praseodymium Doped Sodium Phosphate Glasses

The emission of Pr^{3+}ion was monitored at 640 nm ($^3P_0 \rightarrow {}^3H_6$) and 1330 nm($^1G_4 \rightarrow {}^3H_5$) , by exciting the Nd^{3+} ions using 444 nm ($^3H_4 \rightarrow {}^3P_2$) [60] and 1064 nm ($^3H_4 \rightarrow {}^1G_4$) lasers. The recorded emission spectra are shown in Figure 4.35.

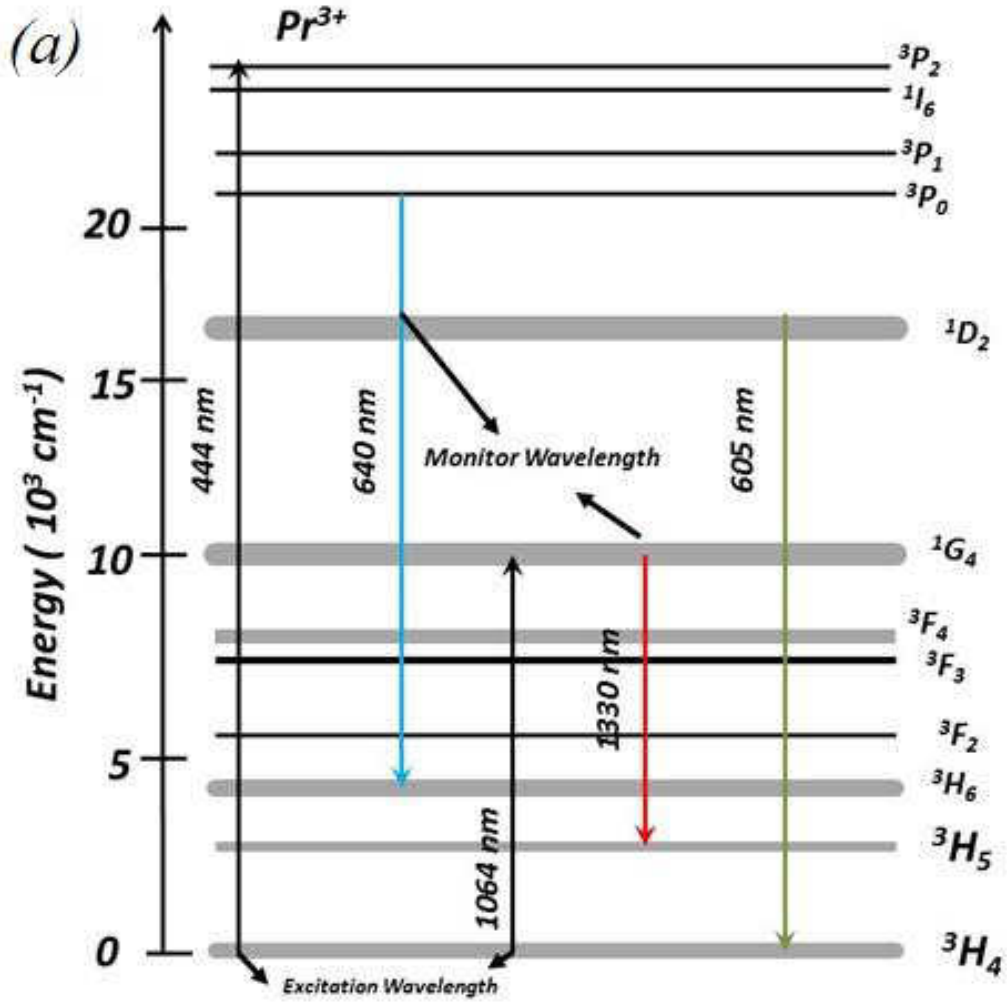

Figure 4. 34: Energy level diagram of Pr^{3+} ion.

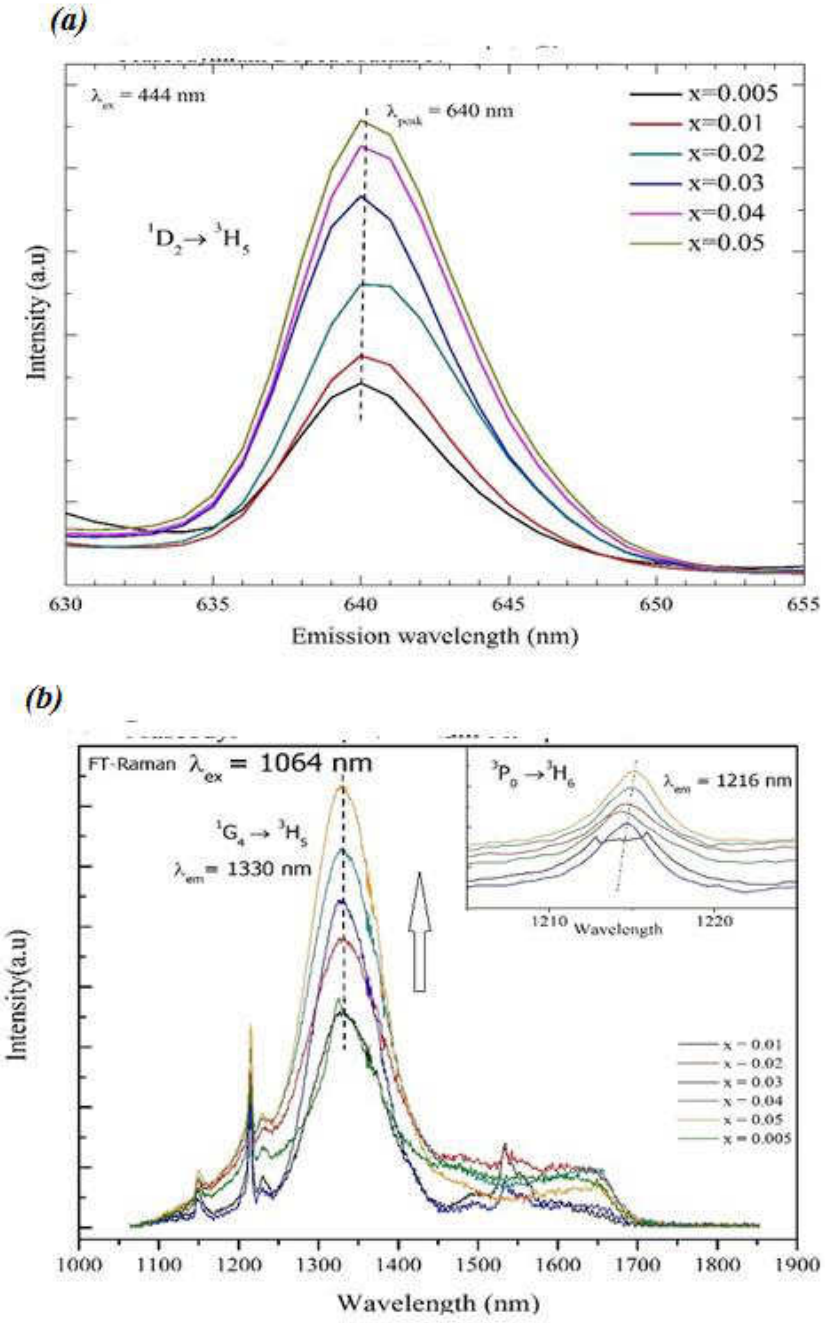

Figure 4. 35 : Emission spectra of praseodymium doped samples (a) 444 nm excitation source (b) 1064 nm excitation and monitoring 640 nm and 1330 nm emission, inset is for Pr^{3+} ion emission at 1216 nm..

4.2 Discussion of the Results

4.2.1 Physical Properties

Density is one of the effective indicator of the degree of structural compactness. Density of a glass is mainly influenced by the molecular weight of glass components, the integration and the compactness of the glass network. Density and molar- volume of a glass depend upon many factors such as structure, coordination number, cross-link density, and dimensionality of interstitial spaces [61] [62] [63].

As shown Figures 4.1 and 4.2, both density and molar volume of glasses increases with increasing the RE_2O_3 concentrations. That is, as the RE^{3+} concentration is increased, two competing factors contribute to density. First is the replacement of a lighter atom (Na) by a heavier one (RE^{3+}) favoring an increase in density. The other is the increase in molar volume which favors a decrease in density. Observed increase in density (Figure 4.1) implies that the first factor mentioned above dominates over the second [1]. The density of the *Nd*-doped glass with x =0.01 is higher than that of all other Nd glasses. This deviation from the trend is due to partial crystallization of the samples during the cooling process [61].

The molar volume, however may be the better quantity for evaluating the compactness of the structural unit. The increase in the molar volume of glasses with increasing RE^{3+} concentration indicates that the replacement Na^+ with RE^{3+} appears to make the glass network looser by expanding the structure to accommodates the larger cation at the interstitial sites. The addition of cation to the glass network also depolymerizes the network by opening the $\left(O_1O_{\frac{2}{2}}P\right) - O - (PO_1O_{\frac{2}{2}})$ $(Q^2\ unit)$ linkages between the phosphate chains. The increase in the molar volume also

indicate the change in the stoichiometry of the glasses by converting the bridging oxygens (BO) to the non-bridging oxygen (NBO).

4.2.2 Thermal Properties

Prior to discussing thermal properties, it is prudent to revisit some of the known features of the atomic level of phosphate glasses.

4.2.2.1 Phosphate Glass Network

The original 3D network of $v - P_2O_5$, where each phosphorus is involved in three $P - O - P$ linkages is degraded by the addition of glass modifier. A glass modifier such as Na^+ disrupts this covalent network by forming $P - O^- - Na^+$ bonds. Thus, the addition of glass modifier reduces the cross-linkage density in the glass network. The breakdown of the network structure then allows the rearrangement to a 1D chain structure at the metaphosphate composition $\left(\frac{O}{P} = 3.0\right)$ where long chains and rings are formed [61]. The addition of alkali cations such as Na^+also decreases the T_g of a glass [64], due to decrease in the cross-links between the different phosphate chains. When Na^+ ($r_{Na+} = 1$ Å$, CN = 5$) is replaced with a cations such as Pr^{3+} $\left(r_{Pr} = 0.99 - 1.126 \text{ Å}, CN = 6 - 8\right)$ or $Er^{3+}\left(r_{Er} = 0.89 - 1.004 \text{ Å}, CN = 6 - 8\right)$. It can increase the T_g by cross linking two phosphate chains. Furthermore, the incorporation of RE^{3+} also decreases the relative fraction of BOs and increases *NBOs* as shown in Figure 4.36.

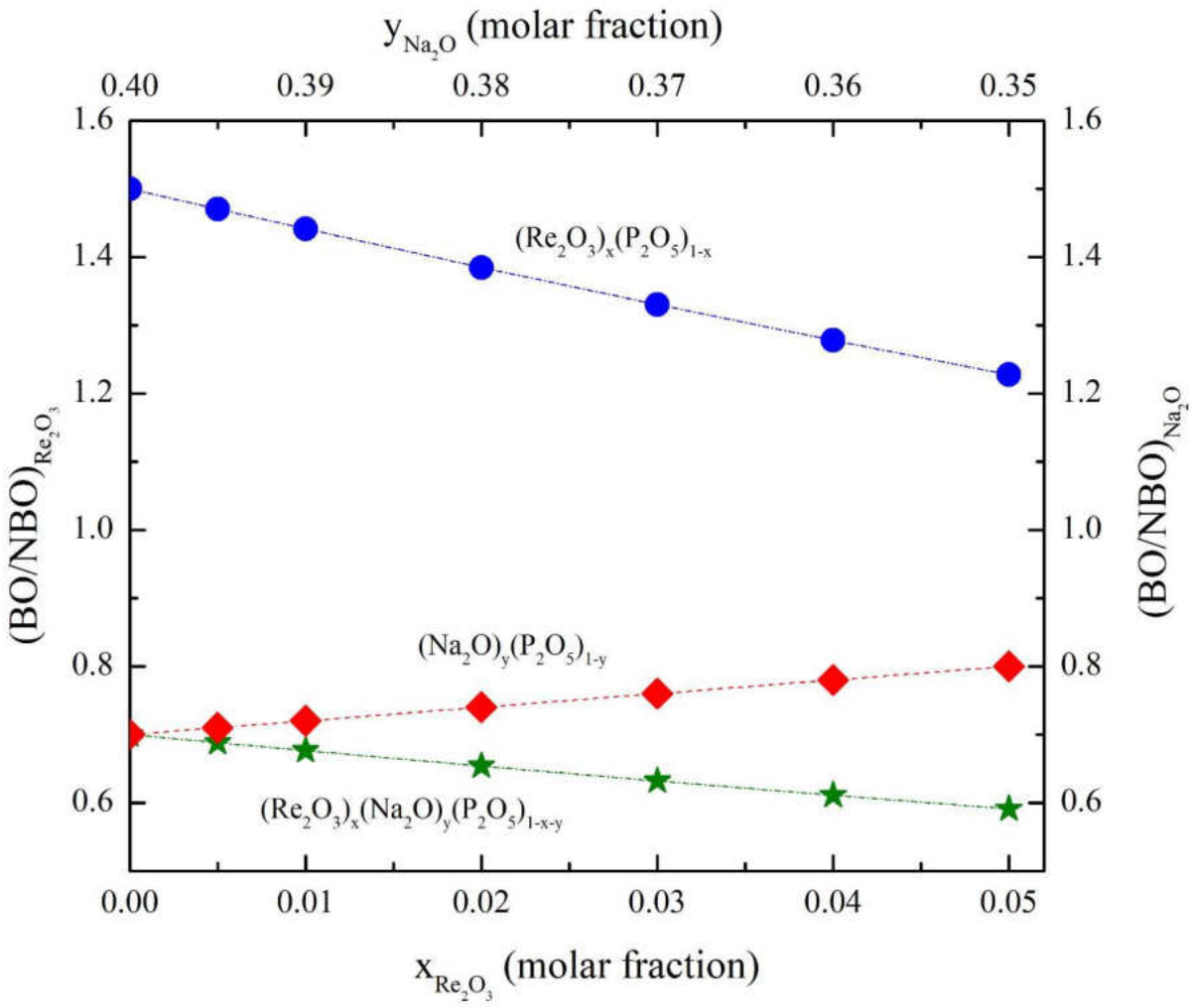

Figure 4. 36: Ratio of BO/NBO for ternary glasses compare with binary phosphate glasses.

In figure 4.36, the decrease in the ratio of BO/NBO after the incorporation of RE_2O_3 $(RE = Pr, Er)$ indicates that RE_2O_3 $(RE = Pr, Er)$ acts as network modifier, and the effect of RE_2O_3 $(RE = Pr, Er)$ is three times of Na_2O [65].

4.2.2.2 Close to Glass Transition Temperature

At the glass transition temperature, the internal energy of the system must be enough to loosen the cross-linking of the network, so that the segments become mobile. The transformation temperature

mainly depends on the strength of the bonds between oxygens and network atoms, the degree of the cross-linking density (chain entanglement) (CLD) $CLD = NC - 2$, and also on the nature of the cations [64] [66] [67].

As shown in Figure 4.6, the glass transition temperature of both Pr and Er doped samples increases with increasing the rare-earth oxide contents. The increase in T_g indicates that the incorporation of rare-earth strengthen the glass network, which is mainly attributed to increase in CLD and bonding strength of $P - O^- - RE^{3+}$. Substitution of RE_2O_3 $(RE = Pr, Er)$ or Na_2O does not change the phosphate chain as the substitution of Re^{3+} for Na^+, three $P - O^- - RE^{3+}$ replaces one of the $P - O^- - Na^+$ linkages and one unstable $(O_1O_{2/2}P) - O - (PO_1O_{2/2})$ linkages between the phosphate chain [65].

4.2.2.3 Effect of Cation Field Strength (CFS)

In figure 4.6, the difference in the slopes of T_g is mainly due to the difference between the ionic radius and cation field strength (CFS) $CFS = Z/r_{ionic}^2$ [68]. The CFS is inversely proportional to the square of the ionic radii of the elements and directly proportional to the valence of the cation. Ionic radius at the given valence state depend upon the coordination number which was reported by Shannon [69]. Because $r_{Er}\,(1.004\,\text{Å}) <\ r_{Pr}(\,1.126\,\text{Å})$, $CFS_{Er}\,(\,2.83) >\ CFS_{Pr}(2.36)$. Furthermore, the smaller radius of erbium ion exerts a stronger electrostatic force on the network and increases the work required to overcome interionic forces and allow the network segments to rearrange at the glass transition [70] [71] . For high field cations with greater electronegativity (*Er* (1.24), *Pr* (1.13), *Na* (0.93)) , covalent $M - O_{nb}$ bonds formed, thus reducing the average covalency of the $P - O_{nb}$ bond [72] [73] [74]. The formation of stronger $M - O_{nb}$ bonds is in accordance with increasing glass transition temperature (T_g) and better chemical durability [75].

For different rare-earth ions, the T_g varies linearly with the ionic radius of the RE^{3+} [76]. Another important factor contributing to the increasing of T_g is increasing the number of ionic cross-linking interactions per mole as the ratio of $\frac{RE^{3+}}{P}$ increases, which makes the chain more stiffer and shorter.

4.2.3 Vibrational Properties

IR spectra also offer some structural information about the bonding characteristic of RE^{3+} ions in glass network. The absorption band $P-O^-$ near $1110\ cm^{-1}$ shifts towards lower wavenumber with increasing RE_2O_3 contents from $0.005\ to\ 0.05$. This shifting suggests that Na_2O in the glass network is replace with RE_2O_3. It is assumed that this shift is due to increase in the number of $P-O^--RE^{3+}$ linkages at the expense of $P-O^--Na^+$linkages [1].

The bands for $(P-O-P)_{as}$ shifts toward lower frequency with increasing RE_2O_3 concentration. The same has been observed in studies of lithium and sodium ultraphosphate glasses with increasing the contents of the modifier [64]. This shift in $(P-O-P)_{as}$ is attributed to the change in chain lengths and the in-chain $(P-O-P)$ bond angle [29] [32] [72]. The presence of RE^{3+} opens the structure and distort the phosphate chain $\left(O_1\ O_{\frac{2}{2}}\ P\right)-O-(PO_{\frac{2}{2}}O_1)$ linkage. This distortion results in large in-chain $P-O-P$ angles. The opening of the structure lead to a conversion of Q^3 to Q^2 group.

The modification in the metaphosphate ($O_{2/2}PO_2^-$) structure resulting from increasing RE_2O_3 concentration can be explained in term of the change in the charge density of anionic site [77] [78]. It is assumed that on increasing the contents of RE_2O_3 some of the ring structures opens and form a smaller structure such as short chains and terminal structures. Thus, the charge density at the ring site may decreases as compare to the charge density at the chain structures and terminal

sites may increases by the addition of RE_2O_3 contents. it is also expected that the interaction between RE^{3+} ions and rings make metaphosphate site become weaker while between RE^{3+} ions and chain or terminal links make metaphosphate site become stronger. This is confirmed by the shifting towards lower frequencies for the band responsible for $P-O-\ P$ ($896\ cm^{-1}$) with ring structure and shifts in position of bands corresponding to chain and terminal metaphosphate. It is suggested that the change in compactness of the glass matrix upon addition of RE_2O_3 is due to the increase of the cross-linked density of Rare-earth ions either by disrupting the bonds connecting the neighboring PO_4 groups or by conversion of meta-phosphate rings into chains and terminal ones.

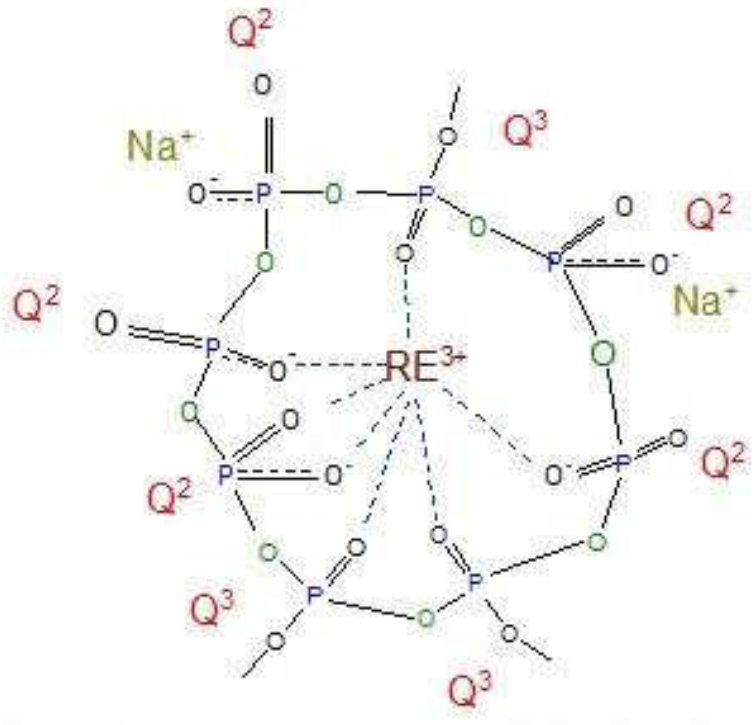

Figure 4. 37 : The proposed structure of rare-earth doped sodium phosphate glasses in view of IR vibrational spectra.

The field strength of RE^{3+} is higher than that of Na^{+}, thus offering stronger ionic bonding between phosphate chains. Moreover, as one RE^{3+} incorporates into the glass network, three $P - O^{-} - RE^{3+}$ linkages will form between phosphate chains. Thus, the increase of cross-links between the phosphate chains will retard the entrance of H_2O molecules (incorporation of OH^{-}), and lead to improved chemical durability of the rare-earth -doped glasses. The proposed structure of the glasses is shown in Figure 4.37.

4.2.4 HEXRD Data

4.2.4.1 Phosphate Network

The $P-O$ peak is fitted with two Gaussians, one for the $P - O_T$ and other for $P - O_B$. Table 4.1 shows non of the bridging and terminal $P - O$ bonds parameters vary as the RE_2O_3 content change x = 0.005 to 0.05. This agrees with several previous studies [17] [32]. The coordination number for the terminal and bridging oxygen are estimated from the relations [42].

$$n_{P-NBO} = 2\,\frac{N_O}{N_p} - 4 \tag{4.21}$$

$$n_{P-BO} = 8 - 2\frac{N_O}{N_p} \tag{4.22}$$

$P-O$ coordination numbers, N_{PO}, obtained herein 3.8 Å are slightly lower than the expected result of 4 .

4.2.4.2 Al-O peak

A small aluminum contamination results in a small addition to *T(r)* at an atomic seperation of $1.8 - 2.0$ Å which cannot be accounted for by considering any *RE, Na, P* and *O* correlation.

This *Al-O* correlation arises from the Al_2O_3 contamination from the crucible. The presence of *Al* small (1-2 wt % Al_2O_3)) [1] or relatively large (17 wt % Al_2O_3) [14] , amounts of Al does not compromise to the immediate rare-earth environment. Therefore, *Al -O* correlation was added to the models. However, the presence of a *Al-O* correlation peak in the vicinity of *P-O* peak might affect the CN of *P-O. Re-O, Na-O* and *O-O* correlations which are represented by three peaks close to each other. The O-O peak was fixed for all fits with parameter $r_{OO} = 2.52$ Å and FWHM $\Delta r_{OO} = 0.2$ Å [17]. This *O-O* distance for the edge of a PO_4 tetrahedron. The number of the edges seen from a given oxygen atom is three or six for O_T or O_B. The mean value $N_{OO} = \frac{24}{5+y}$ [32] where $y = 2\frac{N_O}{N_P} - 5$ [44], therefore N_{OO} in term of $\frac{N_O}{N_P}$ is

$$N_{OO} = 12\left(\frac{N_O}{N_p}\right) \tag{4.23}$$

4.2.4.3 Na-O and RE-O peak

The calculated *O-O* correlations do not fill the peak at2.52 Å, the remaining areas in this ange $(2.1 - 2.5$ Å$)$ are attributed to *RE-O* and *Na-O* correlations. Table 4.1 shows that average *RE-O* distance for the x $(0.005 - 0.05)$ range decreases going from *Pr* to *Er*. . This decrease in inter-atomic distance has been observed by several authors [1,32,24]. The *RE-O* CN in all of these glasses was observed to decrease from ≈ 8 (ultra-phosphate composition) to ≈ 7 for composition close to meta-phosphate glasses as in Figure 4.35. The decrease in CN for *Pr* and *Nd* is ≈ 0.5 when rare-earth concentration changes from 0.005 to 0.05, whereas that is ≈ 0.8 for *Er* for the same range. The average interatomic distance for *Er*-O is approximately 2.26 Å and this inter-atomic

distance increases for large rare-earth ion (*Pr, Nd*) to approximately 2.45 Å for *Pr* and 2.41 Å for *Nd* in Figure 4.36(a). This change in interatomic distance is attributed to lanthanide contraction effect (Figure 4.36 bottom) and the variation of distance going from *Pr* to *Er* is 0.2 Å .

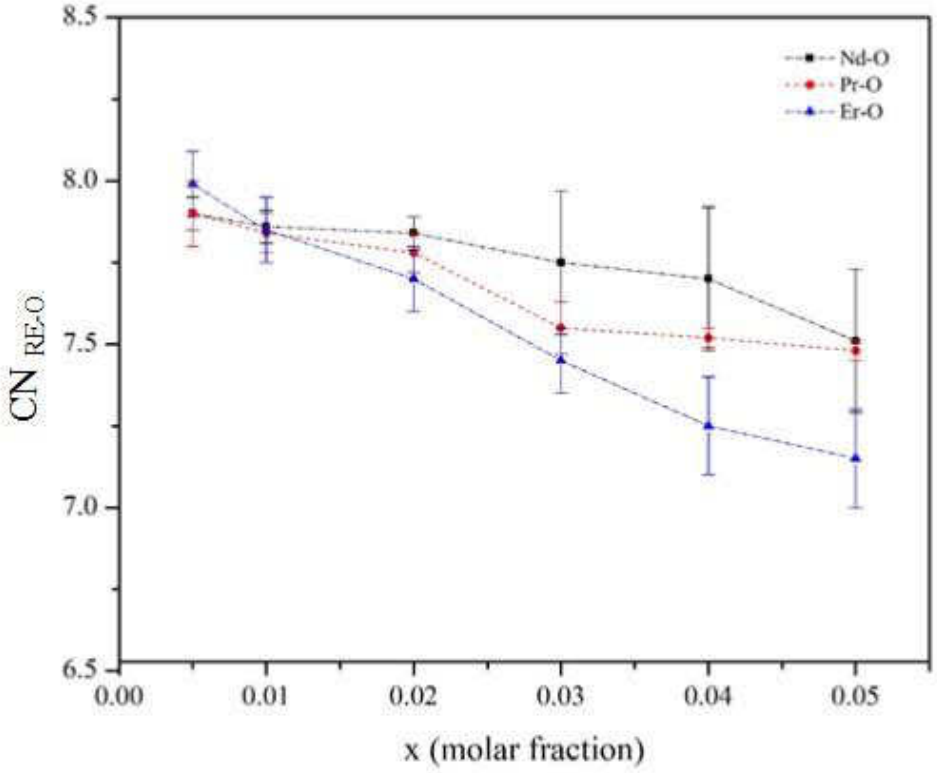

Figure 4. 38: Coordination number (CN) of rare-earth in $(RE_2O_3)_x(Na_2O)_y(P_2O_5)_{1-x-y}$ *glasses, the error in CN were calculated by NXFit program.*

It is evident from Table 4.1 that the change of CN for *Na-O* independent of rare-earth concnetration. By comparing the modeled data with experimental data in Figure 4.15, it is also clear that only affect of changing concentration is on the peak area of *RE-O* going from 0.005 to 0.05. The overlapping and asymmetric Gaussian peaks makes it difficult to have better fit (than the one shown) between the experimental and modeled data, but the residual difference between two curves is less than 5 % .

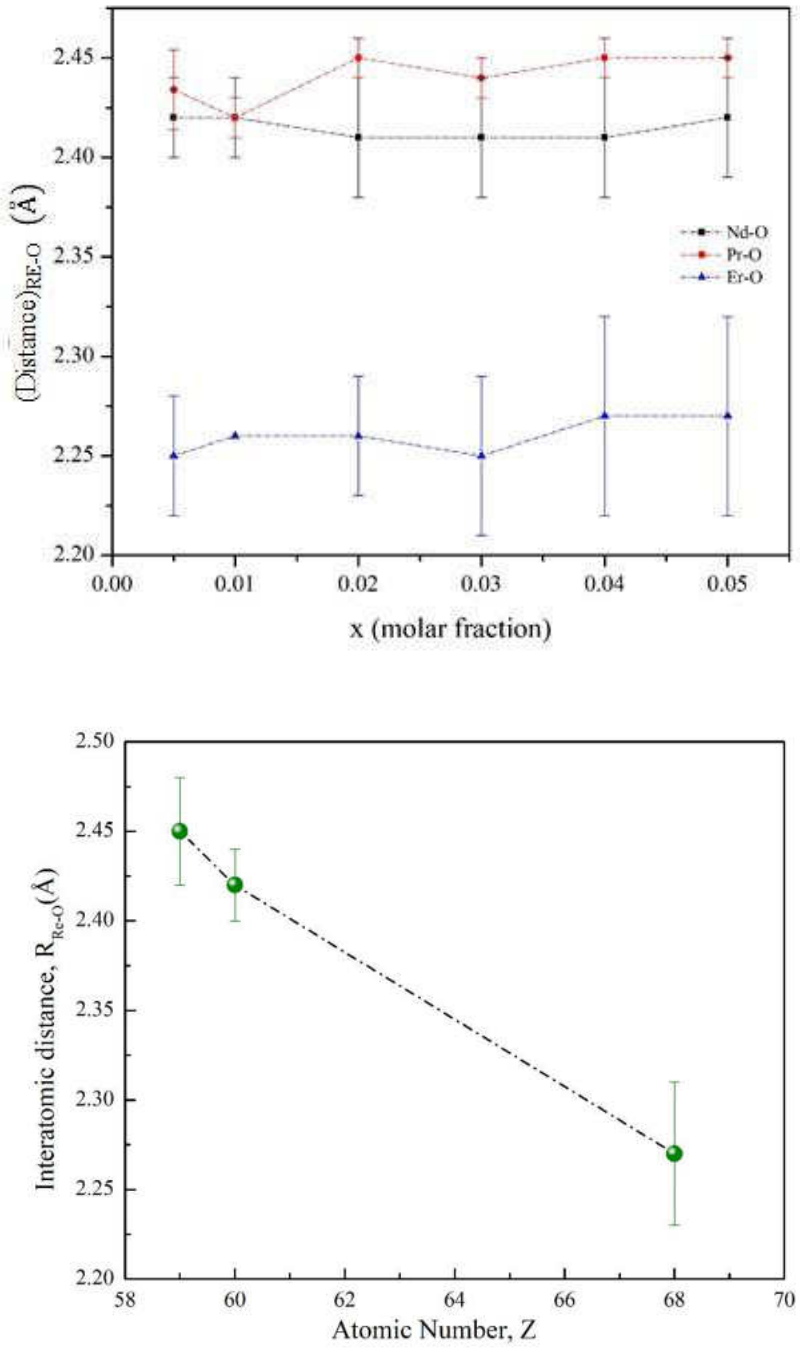

Figure 4. 39: (top) RE-O distances of rare-earth in $(RE_2O_3)_x(Na_2O)_y(P_2O_5)_{1-x-y}$ *glasses (bottom) dependence of RE-O distances* (R_{RE-O}) *on the atomic number of rare-earth atom. The data is for samples with silimar* RE_2O_3 *concentration* $(x \sim 0.05)$.

Therefore, it is useful to consider the ratio of NBO per Me^{y+} cation, M_{NBO} which is given by [32] in term of N_O and N_P as

$$M_{NBO} = \frac{N_{NBO}}{N_{Me}} = \frac{\nu(y+1)}{y} = \frac{\nu\left(2\frac{N_O}{N_p}-4\right)}{\left(\frac{N_O}{N_p}-5\right)} \quad (4.1)$$

where N_{NBO} and N_{Me} are the number of NBOs and cations, respectively. In these glasses where rare-earth and sodium both are acting a glass modifier, M_{NBO} for Na^+ is ≈ 2.50 when x =0.005 and ≈ 2.2 at x =0.05. On the other hand M_{NBO} for RE^{3+} is ≈ 7.40 when x =0.005 and ≈ 6.6 at x =0.05. The CN of *Na-O* is approximately 5, implying that two ions must shared each Na^+ ions and the NaO polyhedra must share edges leading to a *Na-Na* correlation across these edges. For RE^{3+} ions the CN change from 8 to 7.2, as the concnetration increases from $x = 0.005$ to 0.05 . This means that most of the RE^{3+} ions can be presented in isolated polyhedra. The $RE - O$ distances were calculated for coordination 6,7 and 8 oxygens using ionic radii from Shannon [69] , and they were compared with the CN and distances of obtained from HEXRD and EXFAS measurements [79] [80]. The discrepency between the CN deduced from the calculated $RE - O$ (Figure 4.40 & 4.41) and those determined from HEXRD data fall within the uncertainiteis with the fitting data. Another controibuting factors to these uncertainites is the systemic error in HEXRD data.

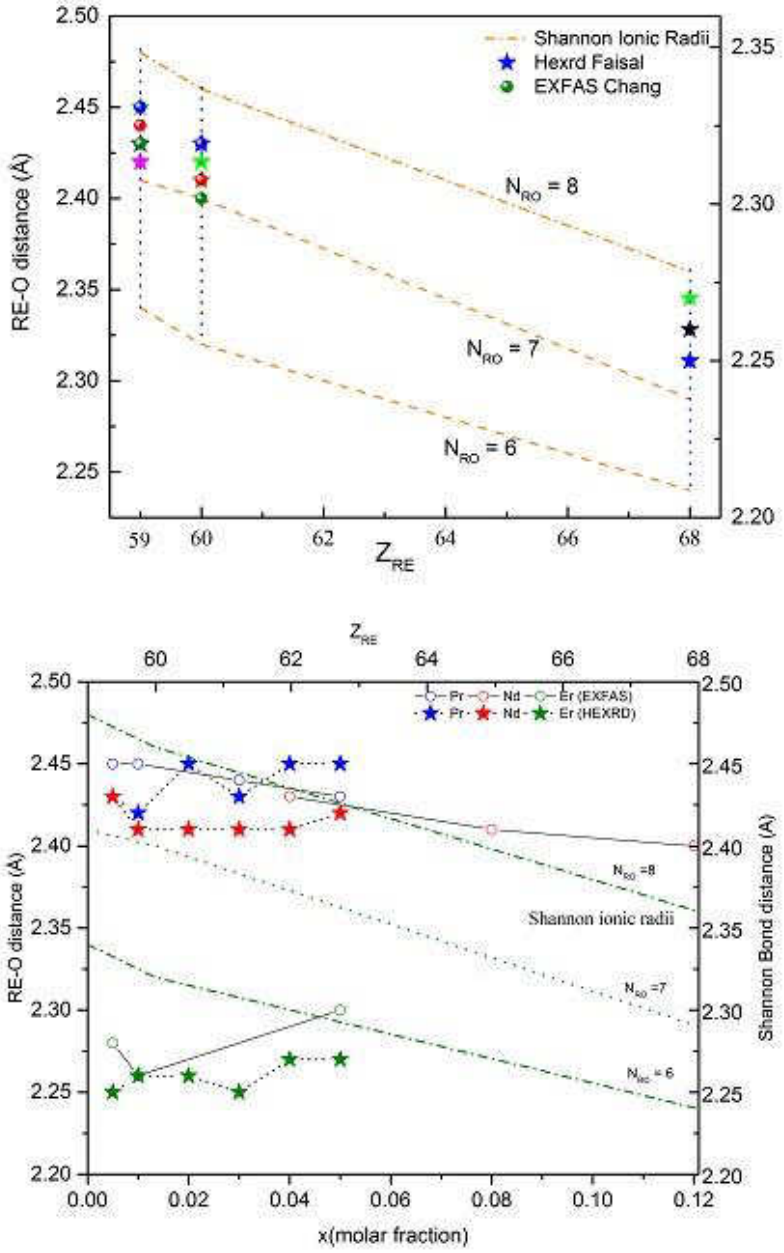

Figure 4. 40: (a) RE-O distance with Shannon radii, (b) Comparison of HEXRD results with EXFAS and Shannon radii The dotted line are Shannon radii for CN =8 and CN =6.

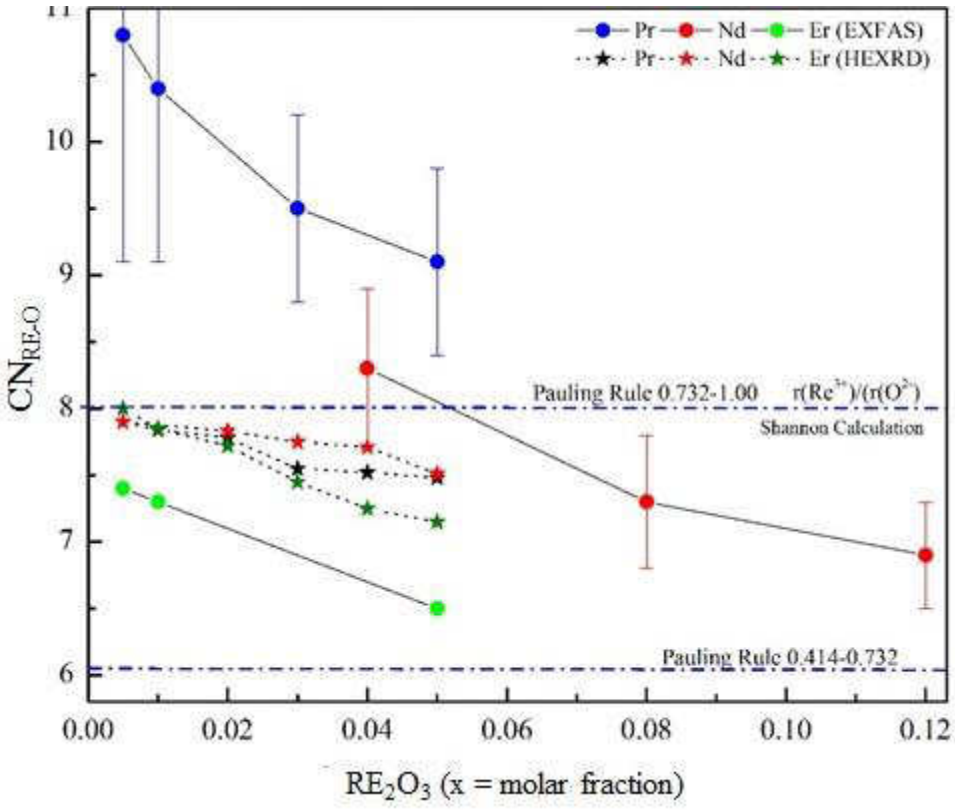

Figure 4. 41: Comparison of HEXRD CN and EXFAS CN. The dotted lines for CN =8 and CN =6 obtained from Shannon radii.

4.2.4.4 P-P peak

The *P-P* coordination number is close to 2 for all rare-earth glasses, but the bond length is slightly shorter (by 0.03 Å) in *Er* doped glasses than in *Pr* and *Nd* doped glass. From the Table 4.1, it is also clear that *P-P* correlation is not effect by the change of composition of rare-earth.

4.2.5 Absorption Properties

4.2.5.1 Judd-Ofelt Analysis

The Judd-Ofelt Theory is applied to the ground state absorption (GSA) spectrum to calculate the manifold-to manifold transition probabilities, from which the radiative lifetimes and branching ratios of emission are determined.

The measured line strengths $S_{measured}$ (Table 4.3) of each absorption band are determined using Equation. (4.5) and the mean wavelength $\bar{\lambda}$, the refractive indexes, and integrated absorption cross-sections also listed in Table 4.2. The values of the doubly reduced matrix elements U_t (t = 2, 4, 6) present in the Equation (2.27) for the calculated line strengths S_{Calc} are given in Table 4.2. The calculated values of JO parameters ($\Omega_t, t = 2,4,6$) are given in Table 4.3.

Table 4. 3 : The measured and calculated line-strength of Nd samples for five transitions.

Transition	$Nd\ (x = 0.02)$ $\times 10^{-20} cm^2$		$x = 0.03$ $\times 10^{-20} cm^2$		$x = 0.04$ $\times 10^{-20} cm^2$		$x = 0.05$ $\times 10^{-20} cm^2$	
	S_{mea}	S_{cal}	S_{mea}	S_{cal}	S_{mea}	S_{cal}	S_{mea}	S_{cal}
$^4F_{3/2}$	*1.2824*	*1.2907*	*1.2309*	*1.1891*	*1.3597*	*1.2504*	*1.1879*	*1.1343*
$^2H_{9/2} + {}^4F_{5/2}$	*4.0020*	*3.9934*	*3.8429*	*3.8903*	*3.9270*	*4.0550*	*3.5533*	*3.6176*
$^2S_{3/2} + {}^4F_{7/2}$	*3.9356*	*3.9429*	*3.9628*	*3.9325*	*4.1652*	*4.0901*	*3.6606*	*3.6264*
$^4F_{9/2}$	*0.3005*	*0.2792*	*0.3225*	*0.2755*	*0.5423*	*0.2866*	*0.4324*	*0.25547*
$^2H_{11/2} + {}^4G_{5/2} + {}^4G_{7/2}$	*6.4523*	*6.4524*	*6.0671*	*6.0667*	*5.9387*	*5.9377*	*5.1684*	*5.1679*
RMS	*0.0181*		*0.0597*		*0.2227*		*0.1410*	

Table 4. 4: Calculated values of JO parameters for Nd doped sodium phosphate glasses.

Sample	Ω_2 ($\times 10^{-20}\ cm^2$)	Ω_4 ($\times 10^{-20}\ cm^2$)	Ω_6 ($\times 10^{-20}\ cm^2$)	$QF = \frac{\Omega_4}{\Omega_6}$
Er x =0.01	*3.87*	*1.25*	*1.14*	
Nd x =0.02	*3.56*	*4.27*	*5.68*	*0.75*
Nd x =0.03	*3.43*	*3.82*	*5.70*	*0.67*
Nd x = 0.04	*3.15*	*4.04*	*5.92*	*0.74*
Nd x = 0.05	*2.63*	*3.69*	*5.24*	*0.70*
Nd x =0.08	*2.28*	*3.64*	*5.06*	*0.72*

The parameters thus obtained are such that, $\Omega_6 > \Omega_4 > \Omega_2$. Ω_2 decreases with increasing of Nd^{3+} concentration. In general, the observed Ω_2 is related to the covalency and asymmetry at the rare-earth sites. The weaker values of Ω_2 suggest that the more centro-symmetrical the ion site and the more ionic the chemical bond with the ligand [81].

The other parameters Ω_4 and Ω_6 are mostly dependent on the bulk properties.Ω_6 is more affected by the radial integral between $4f$ and $5d$ states of the rare-earth ions. The decrease in the Ω_6 is related with the decrease of the $\sigma - bond$ between the ligand and rare-earth ion. The decrease in Ω_6 is also accompanied by an increase in the electron density donated from the ligands, and a decrease in the Coloumbic interaction between the rare-earth ion and the ligands [82].

The spectroscopic quality factor is important in predicting the emission of the laser active medium. The decay rate for the transition ${}^4F_{3/2} \rightarrow {}^4I_J$ ($J = 9/2,11/2,13/2,15/2$) depends only on the

intensity parameters of Ω_4 and Ω_6 , because the second rank matrix element, for transitions between these states is equal to zero. Therefore, the branching ratio $\beta_{JJ'}$ given in Equation (4.17) and plotted in Figure 4.42 can only be expressed in term of one parameter QF

$$\beta_{JJ'} = \frac{\frac{1}{\lambda_{J'}^3}[QF|\langle f^n[SL]J||U^4||f^n[S'L']J'\rangle|^2 + |\langle f^n[SL]J||U^6||f^n[S'L']J'\rangle|^2]}{\sum\frac{1}{\lambda_{J'}^3}[|\langle f^n[SL]J||U^4||f^n[S'L']J'\rangle|^2 + |\langle f^n[SL]J||U^6||f^n[S'L']J'\rangle|^2]} \quad (4.2)$$

In the above equation, the sum is over all the final lower-lying ${}^4I_{J'}$ states. The reduced matrix elements of Nd^{3+} for transitions from ${}^4F_{3/2}$ excited sates to ${}^4I_{J'}$ is given in table 4.5.

Table 4. 5: The reduced matrix elements of $\boldsymbol{Nd^{3+}}$ *for transitions from* $\boldsymbol{{}^4F_{3/2}}$ *excited sates to* $\boldsymbol{{}^4I_{J'}}$

From ${}^4F_{3/2}$	$Energy\ (cm^{-1})$	$\bar{\lambda}\ (nm)$	$\|U^2\|^2$	$\|U^4\|^2$	$\|U^6\|^2$
${}^4I_{15/2}$	*5400*	*1852*	*0*	*0*	*0.0288*
${}^4I_{13/2}$	*7500*	*1333*	*0*	*0*	*0.2085*
${}^4I_{11/2}$	*9500*	*1053*	*0*	*0.1136*	*0.4104*
${}^4I_{9/2}$	*11350*	*881*	*0*	*0.2293*	*0.0548*

Figure 4.42. indicates that to achieve stimulated emission from ${}^4F_{3/2} \rightarrow {}^4I_J$ ($J = 9/2,11/2,13/2,15/2$), transitions of Nd^{3+} it is necessary to have a laser active medium with low value of $QF(\Omega_6 \gg \Omega_4)$ [83].

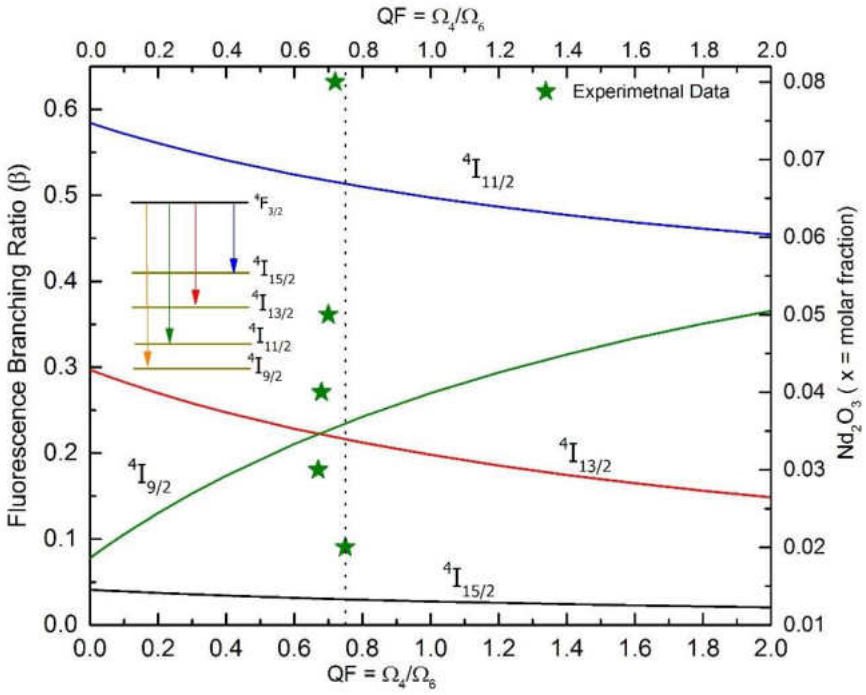

Figure 4. 42: Fluorescence branching ratio for Nd versus the spectroscopic quality factor.

But for the stimulated emission ${}^4F_{3/2} \rightarrow {}^4I_{9/2}$transitions materials with large $QF(\Omega_4 \gg \Omega_6)$. is required. The branching ratio β is the relative contribution of one transition to the total radiative decay. The transition with $\beta >$ 0.5 is potential candidate for laser action [84].

4.2.6 Lifetime Measurements

4.2.6.1 Erbium Doped Sodium Phosphate Glasses

Measured quantum efficiency(η) are slightly lower than those obtained for other commercial phosphate glass (Kigre. Inc., = 80%) [85]. The decrease in lifetimes and η with increasing Er^{3+} ion concentration (Fig. 4.25) is mostly due to an increase of energy transfer between neighboring Er^{3+} ions and energy transfer from Er^{3+} ions to quenching centers like OH^-groups [86].

Specially, the free OH^- $groups$ in the glass are regarded as effective quenchers of the IR radiation in Er^{3+}-doped phosphate glasses [87]. The energy difference between ${}^4I_{13/2} and\ {}^4I_{15/2}$levels Er^{3+} ions ($\sim 6500\ cm^{-1}$) and the OH^- vibrational frequency is about $3429\ cm^{-1}$ in the sodium phosphate glasses (FTIR spectra, Fig. 4.8). Hence only two phonons are required for non-radiative deexcitation of the infrared radiation from ${}^4I_{13/2}$ of Er^{3+} ions as shown in Figure 4.43.

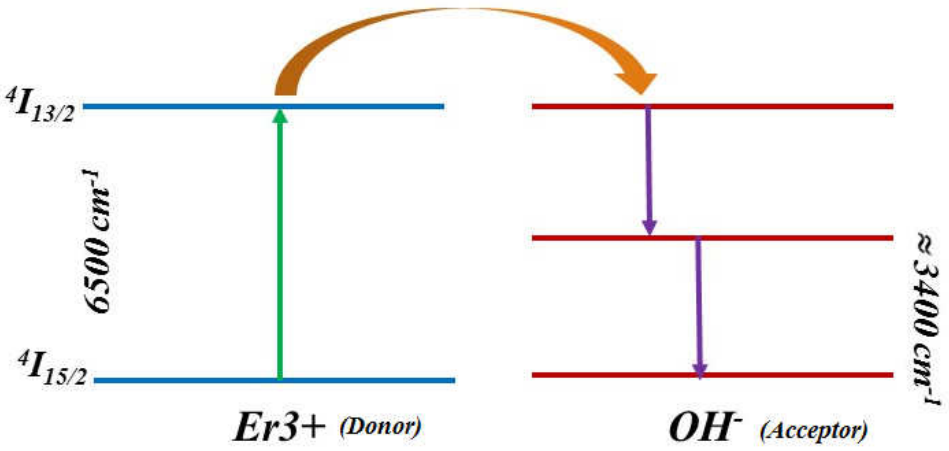

Figure 4. 43: Effect of OH group on ${}^4I_{13/2} \rightarrow {}^4I_{15/2}$transition in erbium doped glasses.

4.2.6.2 Lifetime of Erbium Doped Sodium Phosphate Glasses

The measured lifetime of ${}^4I_{13/2}$level is comparable to the other phosphate glasses containing Al_2O_3 [55] and also Te_2O glasses [88] [89]. From Figure 4.24, it is also clear that lifetime of Er doped glasses decreases as the concentration of Er^{3+} increases.

In general, the lifetime of ${}^4I_{13/2}$ level of Er^{3+} ion is strongly governed by radiative and non-radiative processes. The lifetime τ_{rad} of sample with $x = 0.01$ was calculated using Judd-Ofelt analysis and using known parameters for oscillator strengths (Ω_2 = 3.25, Ω_4 = 0.54, Ω_6 = 0.55) $\times 10^{20} cm^2$ [55] to be $13.79 msec$. The quantum efficiencies calculated using above lifetime for

erbium-doped samples decreases with increasing Er^{3+} concnetration increases as shown in Figure 4.26.

4.2.6.2.1 Effect of Concentration Quenching

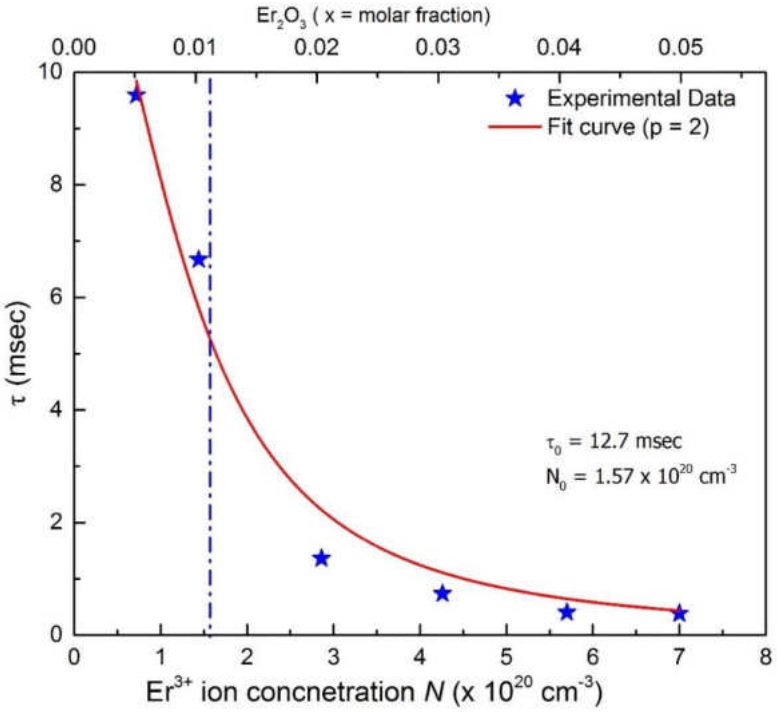

Figure 4. 44: Effect of concentration quenching on the lifetime of erbium ion in sodium phosphate glasses.

The fluorescence lifetime experimental data were fitted with empirical formula shown in equation (4.18) proposed by Auzel et al [90] [91] for the case of limited diffusion as shown in Figure 4.44. Here, the energy transfer from Er^{3+} to nearby defects or trapping centers, also known as quenching traps is assumed to be the main mechanism responsible for the increase in the quenching process.

$$\tau(N) = \frac{\tau_0}{1 + \frac{9}{2\pi}\left(\frac{N}{N_0}\right)^2} \tag{4.3}$$

In the above equation τ is the measured lifetime at a given Er^{3+} ion concentration N, τ_0 is the lifetime in the limit of zero concentration i.e the radiative lifetime, and N_0 is the quenching concentration.

There is good agreement (R = 0.95) between the fit and the calculated values as seen in Figure 4.44. In addition, the values of $\tau_0 = 12.7\ msec$ and $N_0 = 1.57 \times 10^{20}\ ions/cm^3$ obtained from the fit agrees weel with those calculated from data. Another empirical law proposed by Miniscalo [92] relates τ_{exp} with Er^{3+} concentration

$$\tau_{exp} = \frac{\tau_1}{1 + \left(\frac{N_d}{Q}\right)^p} \tag{4.4}$$

where τ_1 is the intrinsic lifetime, Q is a critical quenching concentration, and the exponent p is an adjustable parameter which relates to the number of ions in the interaction process. The published experimental value of p is approximately two [92] [91].

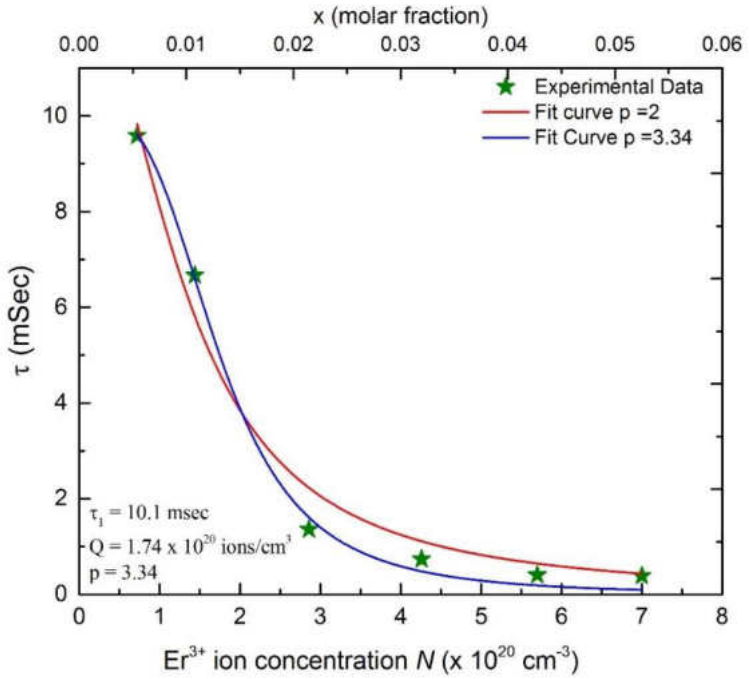

Figure 4. 45 : Effect of concentration quenching and presence of energy transfer via dipole-quadrupole interactions.

The red line in Figure 4.45 is the plot of equation (4.19) with the blue line for $p = 2$. The value of p obtained from the fit to data (blue line Figure 4.45) is 3.34 instead. According to Ref. [93], the deviation from $p = 2$ can be explained by the presence of electric dipole-quadrupole and quadrupole-quadrupole interactions or, alternatively, energy-transfer processes involving more than two particles [94]. The corresponding fit to the experimental lifetime data (blue line in Fig. 4.45, extrapolated to zero concentration, results in an intrinsic lifetime of the first excited level of $\tau_1 = 10.1\, msec$.

4.2.6.3 Neodymium Doped Sodium Phosphate Glasses

The effect of concentration quenching on the Nd^{3+} is shown in Figure 4.46

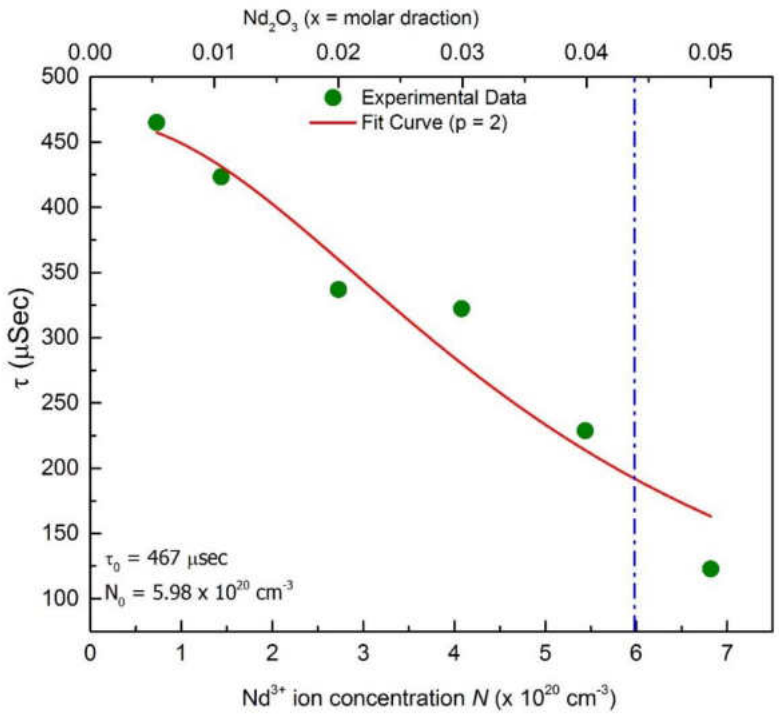

Figure 4. 46: Effect of concentration quenching on the lifetime of neodymium ion in sodium phosphate glasses.

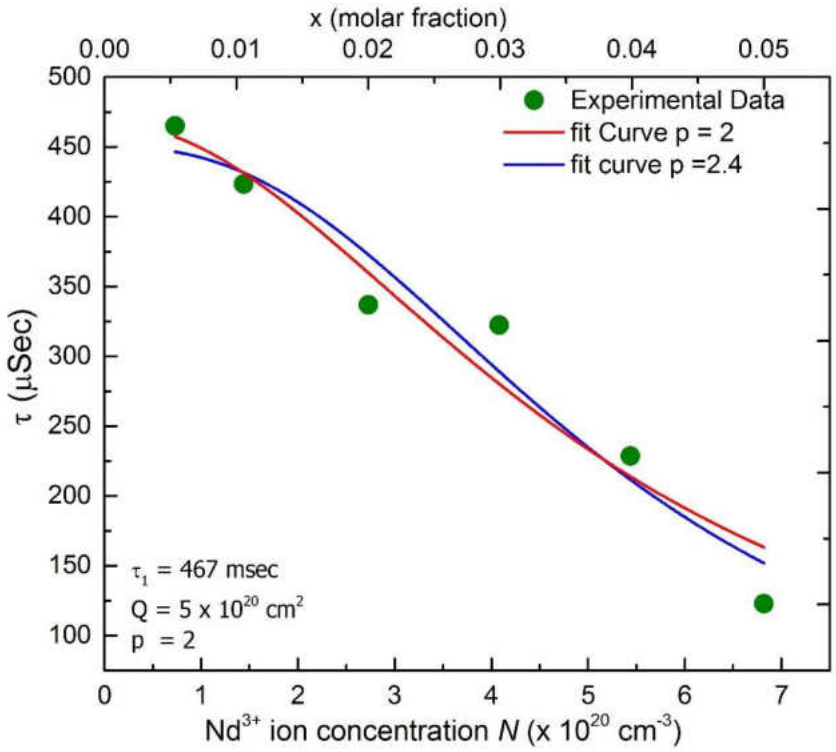

Figure 4. 47 : Effect of concentration quenching and presence of cross relaxation.

There is good agreement (R = 0.98) between the fit and the calculated values as seen in Figure 4.46. In addition, the values of $\tau_0 = 467\ \mu sec$ and $N_0 = 5.98 \times 10^{20}\ 1/cm^3$ obtained from the fit agrees well with those of calculated from data. The red line in figure 4.47 is the plot of equation (4.19) with $p = 2$ and the blue line for $p = 2.24$The best fit value of p obtained from the fit to data (red line in Figure 4.45) is 2 [95] [96], which indicates that two ions participate for the quenching process [95].

By fitting the fluorescence decay curves, $I(t) vs\ t$ using the frame work of the Inokuti-Hirayama (IH) [97]. One can examine the dominant interaction mechanism. According to this model, the decay of fluorescence intensity follows the equation

$$I(t) = I_0 \, exp\left(-\left(\frac{t}{\tau_0}\right) - Q\left(\frac{t}{\tau_0}\right)^{3/S}\right) \tag{4.5}$$

where t is the time after pulsed excitation and τ_0 is the intrinsic decay time of the donors in the absence of acceptors. The value $S = 6{,}8 \; or \; 10$ depends on whether the dominant mechanism of interaction is dipole-dipole, dipole-quadrupole or quadrupole-quadrupole respectively. The energy transfer parameter Q is define as

$$Q = \frac{4\pi}{3} \, \Gamma\left(1 - \frac{3}{S}\right) N_0 R_0^3 \tag{4.6}$$

where the $\Gamma\left(1 - \frac{3}{S}\right)$ is equal to 1.77 in the case of dipole-dipole interaction (S =6), 1.43 for dipole-quadrupole interaction (S =8) and 1.3 for quadrupole-quadrupole interactions (S =10). N_0 is the concentration of acceptors, which is in practice equal to the concentration of RE^{3+} ions and R_0 is the critical distance define as the donor-acceptor separation for which the rate of energy-transfer to the acceptors is equal to the rate of intrinsic decay of the donors. The value of parameter Q can be derived in the fitting process of decay data as shown in Figure 4.48.

The τ_0 values used in the equation 4.20 corresponds to the case of isolated donors, where no energy transfer takes place and the exponential decay curves exhibit perfect single exponential nature. The donor-acceptor energy-transfer parameter (dipole-dipole interaction parameter) $C_{DA}$is related to R_0 by the formula

$$C_{DA} = R_0^S \tau_0^{-1} \tag{4.7}$$

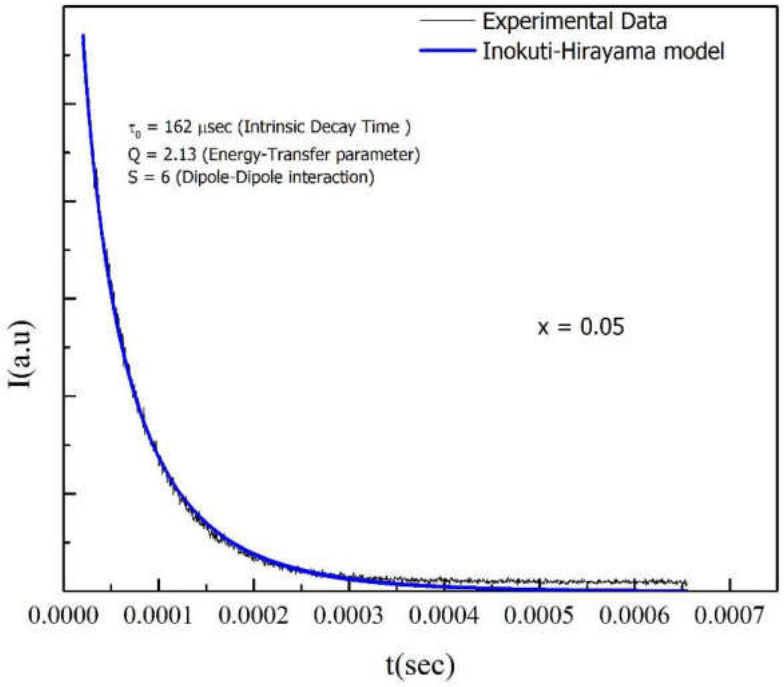

Figure 4. 48 : The Inokuti-Hirayama(IH) model fit for the Nd doped sample with molar fraction x = 0.05.

The values of spectroscopic parameters obtained from decay curve analysis of Nd^{3+} doped glasses are given in Table 4.6.

Table 4. 6: The values of parameters derived by fitting the IH model to non-exponential decay curve of the neodymium doped glasses.

Sample	*molar fraction (x)*	$N_0 \times 10^{20}$ *ions* $/cm^{-3}$	$\tau_0\ (\mu Sec)$	Q	$R_0(nm)$	C_{DA} $(\frac{10^{-40}cm^6}{\text{sec}})$
	0.005	*0.73*	*441*	*0.35*	*0.86*	*9.17*
	0.05	*6.82*	*162*	*2.13*	*0.75*	*10.98*

The non-exponential nature of the decay curves (Figure 4.48) is well fitted to IH model for $S = 6$, indicating that the dominant interaction for energy-transfer through cross-relaxation (CR) between

Nd^{3+} ions is of dipole-dipole type [98]. The energy -transfer parameter Q is increased whereas the donor (excited Nd^{3+}) -acceptor (non -excited Nd^{3+}) separation (R_0) and dipole-dipole interaction parameter (C_{DA}) are decreased with increase in concentration. The increase in the Q value with the increasing concentration is due to the increase of effective density of donors and acceptors. The values obtained for these glasses samples are found to be relatively higher than those values derived for $Nd:YAG$ [99]and $Nd^{3+}:YAlO_3$ [100].

4.2.7 Emission Properties

4.2.7.1 Erbium Doped Samples

As seen in Figure 4.31(d), the intensity of peak at $1530\ nm$ increases as the doped erbium ion concentration increases. The fluorescence intensity reaches a maximum at an Er^{3+} concentration of about x =0.01.

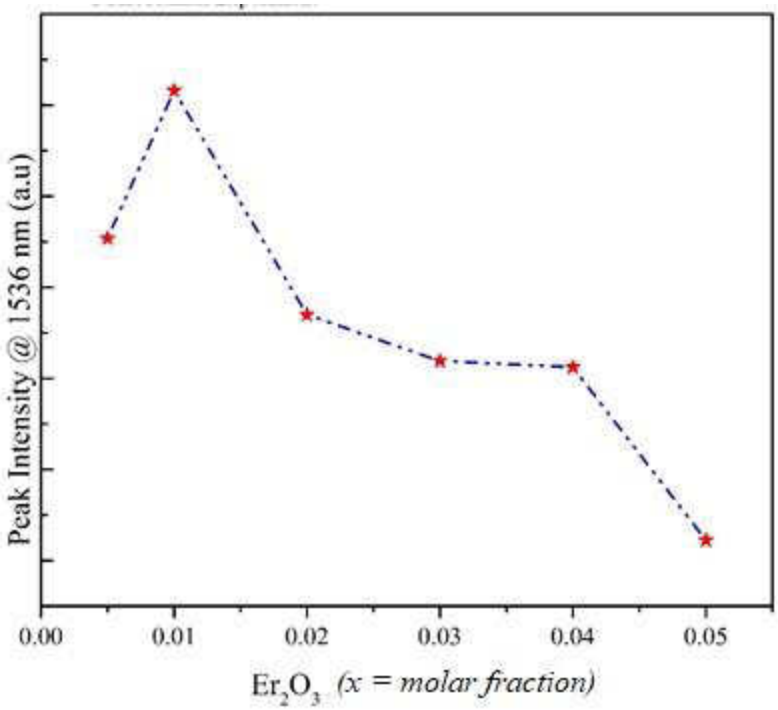

Figure 4. 49 : The relationship between fluorescence intensity and erbium ion concentration.

Over this doping concentration, the fluorescence intensity decreases, due to the doped concentration quenching as the doped erbium ion concentration further increases [101]. The relationship between the peak value of fluorescence and Er^{3+}concentration is shown in Figure 4.49.

The decrease in fluorescence intensity is attributed to the energy transfer of excited erbium ion to the nearby ions or the presence of water in the samples [102].

The other important parameter for the evaluation of emission properties is the emission effective band width of emission spectra defined as $\Delta\lambda_{eff} = \frac{1}{I_p}\int I(\lambda)d\lambda$ [52] [103]and plotted in Figure 4.50.

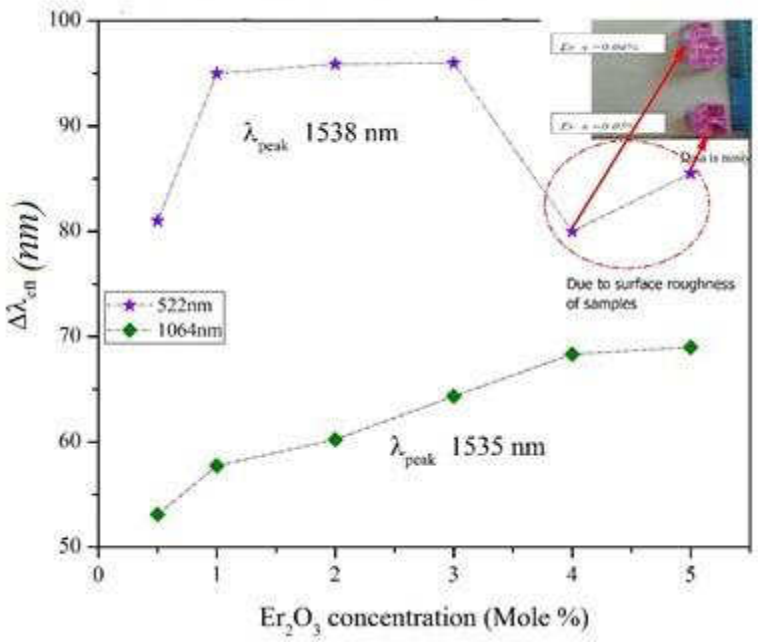

Figure 4. 50: Comparison of effective bandwidth of emission spectra at 522 nm and 1064 nm excitation sources.

Though no peak shift $\left(\lambda_{peak} = 1538\, nm\right)$ has been observed, the broadness of the emission spectra does increase considerably (FWHM 50–70 nm, 80- 92 nm) with the increase of Er^{3+}ion concentration at two different excitation wavelengths.

$\Delta\lambda_{eff}$ increases linearly with erbium ion concentration for $1064\, nm$ source but for $522\, nm$ source, it increases first up to *(x= 0.01)* and the increase in very small up-to $(x = 0.03)$.The decrease of $\Delta\lambda_{eff}$ for $(x = 0.04)$ and $(x = 0.05)$ sample is attributed to the sample cracks as shown in inset of figure 4.50. The emission broadening with the increasing of Er^{3+} concentration could be due to occupation of active ions in various sites of microscopic environment, and the coordination number [104] . which results in more inhomogeneous broadening. However, observed broadness can also arise from self-absorption and radiation trapping processes [105].

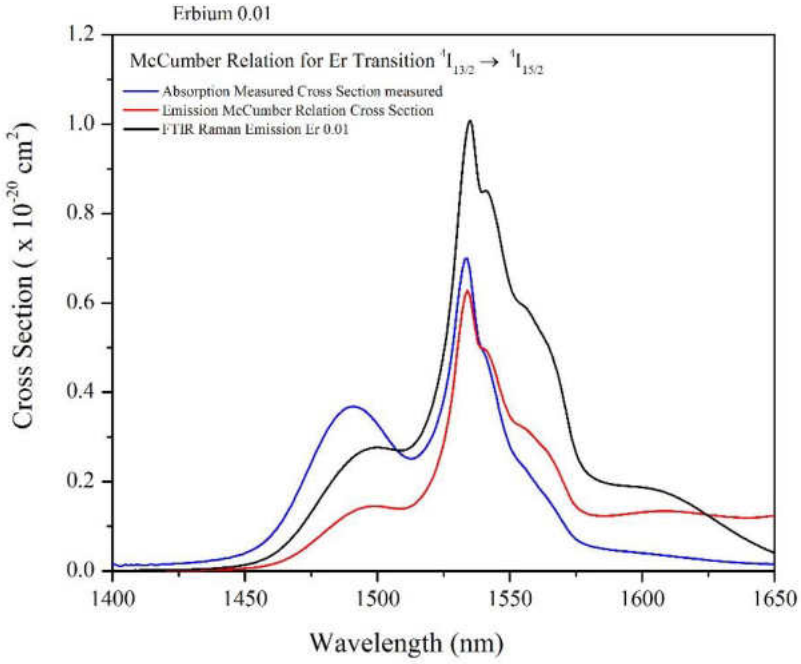

Figure 4. 51 : Absorption and emission cross-section of the transition for (x= 0.01) of erbium-doped glass.

The addition of more Er^{3+} ions also modifies the structure with greater variety of dopant sites. The local crystal field generated in the higher concentration samples seems to be mainly responsible for the larger broadening of the IR emission. The theory of McCumber [106] provides simple relations that uniquely relate absorption and emission cross-sections of glasses in Figure 4.51.

4.2.7.2 Neodymium Doped Sodium Phosphate Glasses.

The peak intensity (I_{peak}) and $\Delta\lambda_{eff}$ for the Nd doped glasses are shown in Figure 4.52 and 4.54.

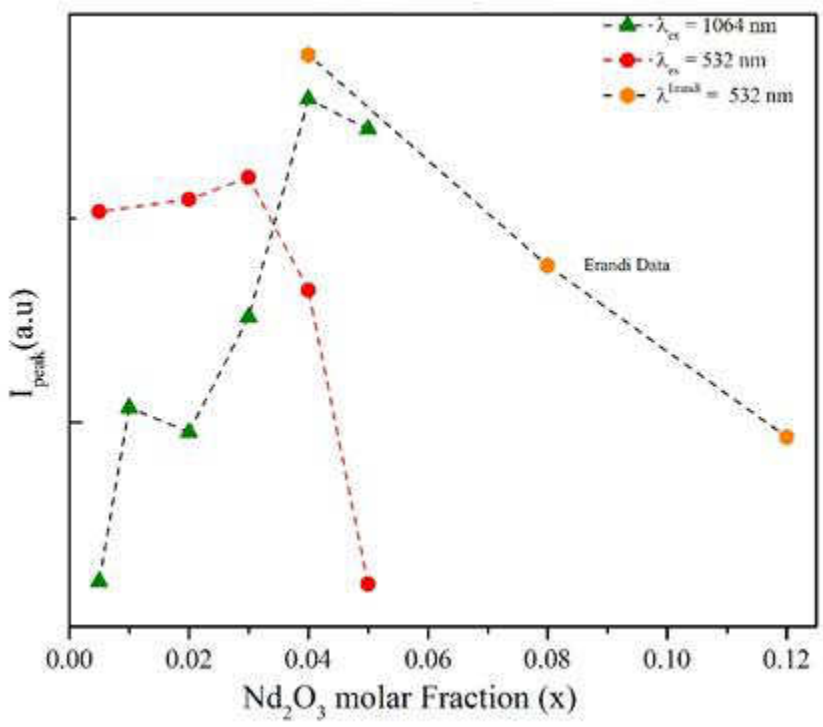

Figure 4. 52 : Peak intensity of Nd doped samples at different excitation sources.

As shown in Figure 4.33(b) , the excitation at by a $532\ nm$ laser gives emission transitions at $1064\ nm$ and $1330\ nm$. The peak intensity of the emission at $1064\ nm$ increases with the Nd^{3+} ion concentration up-to $3\ mole\ \%$, but decreases as the Nd^{3+} concentration further increases,

when excited with $532\,nm$. This decreases in the intensity is attributed to the concentration quenching and presence of OH^-[107], which results in cross energy transfer [108]. The schematic diagram of the relaxation processes is shown in Figure 4.53 [109].

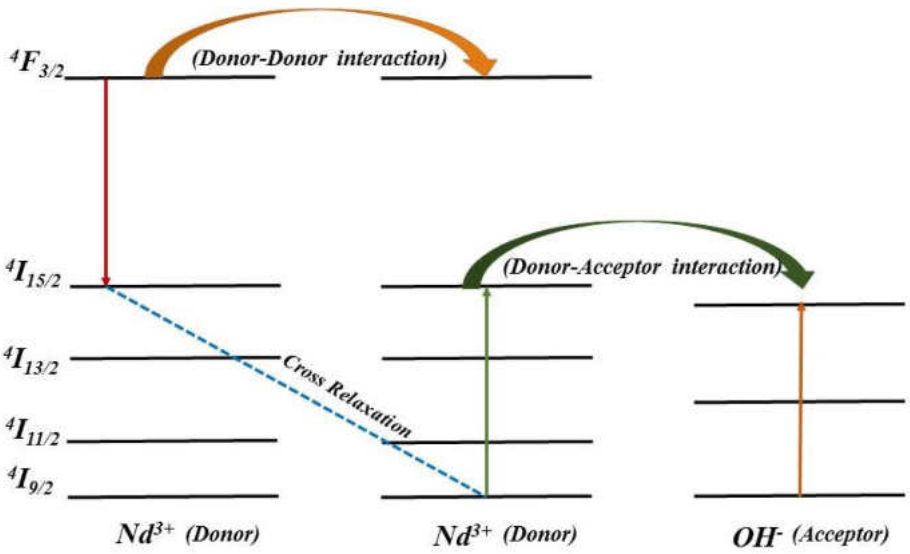

Figure 4. 53: Schematic diagram of the relaxation processes dominating the depopulation of the $^4F_{3/2}$ level of excited Nd^{3+} ions.

The intensity of the emission line at $1330\,nm$, see Figure 4.33(c), increases as the Nd^{3+} ion concentration increases, when excited with a $1064\,nm$ laser source. However, intensity of this transition is small for $532\,nm$ laser excitation as compare to $1064\,nm$ laser. Furthermore, the change in $\Delta\lambda_{eff}$ for these transitions are very small.

4.2.7.3 Praseodymium Doped Sodium Phosphate Glasses

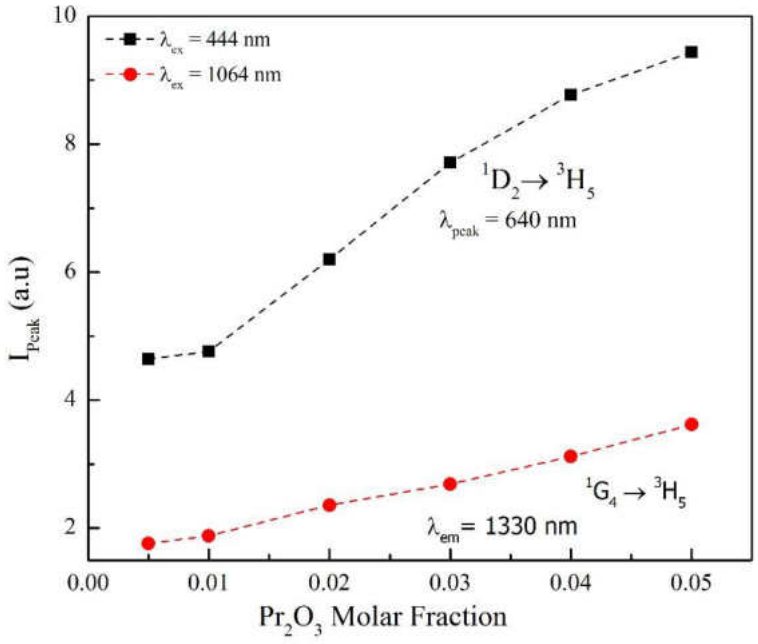

Figure 4. 54 : Peak intensity of praseodymium doped glasses at 444 nm and 1064 nm laser wavelengths.

The emission spectra of Pr doped glasses increase linearly with Pr^{3+} ion concentration for both the excitations at $444\ nm$ and $1064\ nm$ laser sources. However, the peak emission for $444\ nm$ laser is at $640\ nm$ and for $1064\ nm$ laser, it is at $1330\ nm$.

References

[1] P. Y. Shih, "Thermal, chemical and structural characteristics of erbium-doped sodium phosphate glasses," *Materials Chemistry and Physics ,* vol. 84 , p. 151–156, 2004.

[2] Y. Moustafa and K. El-Egili,, "Infrared spectra of sodium phosphate glasses," *Journal of Non-Crystalline Solids,* vol. 240, no. 13, pp. 144-153, 1998.

[3] Y. Moustafa, H. Doweidar and G. El-Damrawi, "Utilization of infrared spectroscopy to determine the fraction of the four coordinated borons in borate glasses," *Physics and Chemistry of Glasses,* vol. 35, no. 2, pp. 104-106, 1994.

[4] SPSS, Incorporated, *PeakFit 4.0 for Windows User's Manual.,* SPSS, Incorporated, 2000.

[5] G. T. Stranford, R. A. Condrate Sr and B. C. Cornilsen, "The Raman spectrum of α-zinc pyrophosphate," *Journal of Molecular structure,* vol. 73, no. 1, pp. 231-234, 1981.

[6] B. Bridge and N. Patel, "Composition dependence of the infrared absorption spectra of molybdenum phosphate glasses and some crystalline analogues," *Journal of Non-Crystalline solids,* vol. 91, no. 1, pp. 27-42, 1987.

[7] P. Znasik and M. Jamnicky, "Preparation, infrared spectra and structure of glasses in the system cucl/cu2o-(p2o5 + moo3),"," *Journal of Non-Crystalline Solids,* vol. 146, pp. 74 - 80 , 1992.

[8] M. Jamnick, P. Znik, D. Tunega and M. D. Ingram, "Glass formation and structure in the system cu2o-p2o5-moo3," *Journal of Non-Crystalline Solids,* vol. 185, no. 12, pp. 151-158, 1995.

[9] E. Metwalli, M. Karabulut, D. Sidebottom, M. Morsi and R. Brow, "Properties and structure of copper ultraphosphate glasses,"," *Journal of Non-Crystalline Solids,* vol. 344, no. 3, pp. 128-134, 2004.

[10] J. R. Wazer, "Structure and properties of the condensed phosphates. ii. a theory of the molecular structure of sodium phosphate glasses1," *Journal of the American Chemical Society,* vol. 72, no. 2, pp. 644-647, 1950.

[11] S. W. Martin, "Review of the structures of phosphate glasses," *European Journal of Solid State Inorganic Chemistry,* vol. 28, pp. 163-205, 1991.

[12] R. Brow, C. Click and T. Alam, "Modifier coordination and phosphate network," *Journal of Non-Crystalline Solids,* vol. 274, no. 13, pp. 9-16, 2000.

[13] R. Hussin, "Vibrational Studies of Calcium Magnesium Ultraphosphate Glasses," *Journal of Fundamental Science,* vol. 5, pp. 41-53, 2009.

[14] B. Bunker, G. Arnold and J. Wilder, "Phosphate glass dissolution in aqueous solutions," *Journal of Non-Crystalline Solids,* vol. 64, no. 3, pp. 291-316, 1984.

[15] K. Meyer, "Characterization of the structure of binary zinc ultraphosphate glasses by infrared and raman spectroscopy," *Journal of Non-Crystalline Solids,* vol. 209, no. 3, pp. 227 -239, 1997.

[16] R. K. Brow, D. R. Tallant, J. J. Hudgens and S. W. Martin, "The short-range structure of sodium ultraphosphate glasses," *Journal of Non-Crystalline solids,* vol. 177, pp. 221-228, 1994.

[17] R. K. Brow, D. R. Tallant, S. T. Myers and C. C. Phifer, "The short-range structure of zinc polyphosphate glass," *Journal of Non-Crystalline solids,* vol. 191, no. 12, pp. 45 - 55, 1995.

[18] J. j. Hudgens and S. W. Martin, "Glass transition and infrared spectra of low-alkali, anhydrous lithium phosphate glasses," *Journal of the American Ceramic Society,* vol. 76, no. 7, pp. 1691-1696, 1993.

[19] M. Salim, G. G. Khattak and M. Hussain, "X-ray photoelectron spectroscopy, fourier transform infrared spectroscopy and electrical conductivity studies of copper phosphate glasses," *Journal of Non-Crystalline Solids,* vol. 185, no. 12, pp. 101-195, 1995.

[20] P. Y. Shih, "Thermal, chemical and structural characteristics of erbium-doped sodium phosphate glasses," *Materials Chemistry and Physics,* vol. 84, no. 1, pp. 151-156, 2004.

[21] T. Jermoumi, S. Hassan and m. Hafid, "Structural investigation of vitreous barium zinc mixed metaphosphate," *Vibrational Spectroscopy,* vol. 32, no. 2, p. 207–213, 2003.

[22] E. Metwallia, M. Karabulutc, D. L. Sidebotto and R. K. Brow, "Properties and structure of copper ultraphosphate glasses," *Journal of Non-Crystalline solids,* vol. 344, no. 3, p. 128–134, 2004.

[23] H. Doweidar, Y. M. Moustafa, K. El-Egili and I. Abba, "Infrared spectra of Fe2O3–PbO–P2O5 glasses," *Vibrational spectroscopy,* vol. 37, no. 1, p. 91–96, 2005.

[24] F. H. ElBatal, M. A. Ouis, R. M. Morsi and S. Y. Marzouk, "\Interaction of gamma rays with some sodium phosphate glasses containing cobalt," *Journal of Non-Crystalline Solids,* vol. 356, no. 1, pp. 46 - 55, 2010.

[25] F. ElBatal, Y. Hamdy and S. Marzouk, "Gamma ray interactions with v2o5-doped sodium phosphate glasses," *Materials Chemistry and Physics,* vol. 112, no. 3, pp. 991-1000, 2008.

[26] H. Liu, T. Chin and S. Yung, "FTIR and XPS studies of low-melting pbo-zno-p2o2 glasses," *Materials Chemistry and Physics,* vol. 50, no. 1, pp. 1-10, 1997.

[27] S. Abo-Naf, M. El-Amiry and A. Abdel-Khalek, "Ftir and uvvis optical absorption spectra of ?-irradiated calcium phosphate glasses doped with cr2o3, fV2O5g and fe2o3," *Optical Materials,* vol. 30, no. 6, pp. 900 - 909, 2008.

[28] M. R. Sahar, A. Wahab , M. A. Hussein and R. Hussin, "Structural characteristic of Na2Osingle bondP2O5single bondGeO2 glass systems," *Journal of Non-Crystalline solids,* vol. 353, no. 11-12, p. 1134–1140, 2007.

[29] J. O. Byun, B. H. Kim, , K. S. Hong and H. J. Jung, "Properties and structure of RO| |Na2O| |Al2O3| |P2O5 (R = Mg, Ca, Sr, Ba) glasses," *Journal of Non-Crystalline Solids,* vol. 190, no. 3, p. 288–295, 1995.

[30] W. P. Griffth, "Vibrational spectra of metaphosphates meta-arsenates and metavanadates," *journal of Chemical Society A,* pp. 905-908, 1967.

[31] M. S. Rohani, A. A. Rasid, M. R. Sahar and A. Kassim, "Spectroscopic properties of er3+ doped Phosphate Glasses," *AIP Conference Proceedings,* vol. 4217, no. 1, 2010.

[32] J. Koo, B. S. Bae and H. K. Na, "Raman spectroscopy of copper phosphate glasses," *Journal of Non-Crystalline Solids,* vol. 212, no. 23, pp. 173 - 179, 1997.

[33] G. B. Rouse Jr., P. J. Philip J Miller and w. M. Risen, "Mixed alkali glass spectra and structure," *Journal of Non-Crystalline Solids,* vol. 28, no. 2, p. 193–207, 1978.

[34] L. Montagne, G. Palavit and G. Mairesse, "31P MAS NMR and FT IR analysis of (50-x/2)Na2O.xBi2O2.(50-x/2)P2O 2 glasses," *Physics,Chemistry of Glasses,* vol. 37, no. 5, pp. 206-211, 1994.

[35] D. E. Corbridge, "Infrared analysis of phosphorus compounds," *Journal of applied Chemistry,* vol. 6, pp. 456-465, 1956.

[36] Y. Ratnakaram and A. V. Reddy, "Electronic spectra and optical band gap studies in neodymium chlorophosphate glasses," *Journal of Non-Crystalline Solids,* vol. 277, no. 23, pp. 142 - 154, 2000.

[37] B. Karmakar, P. Kundu and R. Dwivedi, "IR spectra and their application for evaluating physical properties of flourophosphate glasses," *Journal of Non-Crystalline solids,* vol. 289, no. 13, pp. 155 -162, 2001.

[38] N. Machida, M. Chusho and T. Minami, "Preparation of cuprous ion-conducting glasses in the system cui-cu2o-moo3," *Journal of Non-Crystalline Solids,* vol. 101, no. 1, pp. 70 - 74, 1988.

[39] W. T. Carnall, P. R. Fields and K. Rajnak, "Electronic energy levels in the trivalent lanthanide aquo ions. i. pr3+, nd3+, pm3+, sm3+, dy3+, ho3+, er3+, and tm3+," *Journal of chemical physics,* vol. 49, no. 10, 1968.

[40] H. Lin, K. Liu, E. Pun, T. Ma, X. Peng, Q. An, , "Infrared and visible fluorescence in Er doped Gallium Tellurite glasses," *Chemical Physics Letters,* vol. 398, no. 13, pp. 146-150,, 2004.

[41] P. Babu, H. J. Seo, K. H. Jang, R. Balakrishnaiah,, *J. Opt. Soc. Am. B,* vol. 24, pp. 2218-2228, 2007.

[42] D. K. Sardar, J. B. Gruber, B. Zandi, J. A. Hutchi, "Judd Ofelt Analysis of the er3+(4f11) absorption intensities in phosphate glass: Er3+,yb3+,"," *Journal of Applied Physics ,* vol. 93, no. 4, 2003.

[43] M. Jayasimhadri, L. R. Moorthy, K. Kojima, K. Yama, "Er3+ -doped telluroflurophospahte glasses for laser and optical amplifiers," *Journal of Physics: Condensed Matter,,* vol. 17, no. 48, p. 7705, 2005.

[44] W. A. Pisarski, "Spectroscopic analysis of praseodymium and erbium ions in heavy metal fluoride and oxide glasses," *MOLECULAR SPECTROSCOPY AND MOLECULAR STRUCTURE,* vol. 744747, pp. 473- 479, 2005.

[45] B. R. Judd, "Optical absorption intensities of rare-earth ions," *Phys. Rev,* vol. 127, pp. 750 - 761, 1962.

[46] G. S. Ofelt, "\Intensities of crystal spectra of rare-earth ions," *The Journal of Chemical Physics,,* vol. 37, no. 3, 1962.

[47] M. Jayasimhadri, L. R. Moorthy, K. Kojima, K. Yama, "Er -doped tellurfluorophosphate glasses for lasers and amplifiers," *journal of physics condensed matters,* vol. 17, no. 48, pp. 7705,, 2005.

[48] B. M. Walsh, "Advances in Spectroscopy for Lasers and Sensing,," in *ch. Judd-Ofelt theory: principlesand practices*, Dordrecht: Springer Netherlands, 2006, 2006, pp. 403-433.

[49] G. C. Righini, M. Ferrari, G. C. Righini, and M. F, "Photoluminescence of rare-earthdoped glasses," *RIVISTA DEL NUOVO CIMENTO,* vol. 28, no. 12, 2005.

[50] D. K. Sardar, J. B. Gruber, B. Zandi, J. A. Hutchi, "Judd ofelt analysis of the er3+(4f11) absorption intensities in phosphate glass," *Journal of Applied physics ,* vol. 93, no. 4, 2003.

[51] *SciGlass - Glass Property Information System,* EPAM Systems, 2014.

[52] A. A. Reddy, S. S. Babu, K. Pradesssh, C. J. Otton and G. v. Prakash, "Optical properties of higly Er doped sodium aluminium phosphate glasses for broadband 1.5 micron emission," *Journal of Alloys and compounds,* vol. 509, pp. 4047 - 4052, 2011.

[53] Z. Luo, Y. Huang and X. Chen, Spectroscopy of Solid-state Laser and Luminescent Material, Nova Science Pub Inc, 2006.

[54] J. Lakowicz, Principles of Fluorescence Spectroscopy, Springer US, 2007.

[55] A. A. Reddya, S. S. Babub, K. Pradeesh, C. J. Ottonc and G. V. Prakasha, "Optical Properties of highly Er doped sodium aluminium phosphate glasses for broadband 1.5 micron emission," *Journal of Alloys and Compounds,* vol. 509, p. 4047–4052, 2011.

[56] A. Rao, Y. Ahammed, R. Reddy and T. Rao, "Spectroscopic studies of nd3+-doped alkali flouroborophosphate glasses," *Optical Materials,* vol. 10, no. 4, pp. 245-252, 1998.

[57] T. Som,, S. Singh and B. Karmakar, "Chapter 9 - plasmonic antimony and bismuth oxide glass nanocomposites: Synthesis and enhanced photoluminescence," in *Glass Nanocomposites*, Boston, William Andrew Publishing, 2016, p. 215 { 238.

[58] A. A. Reddy , M. C. Sekhar, K. Pradeesh , S. S. Babu and G. V. Prakash, "Optical properties of Dy3+-doped sodium–aluminum–phosphate glasses," *J Mater Sci,* vol. 46, pp. 2018-2023, 2011.

[59] P. Babu, H. J. Seo, K. H. Jang, R. Balakrishnaiah and C. K. Jayasankar, *Journal of Optical society America B,* vol. 24, pp. 2218 - 2228, 2007.

[60] K. Zhang, "A high energy x-ray diffraction investigation of sodium phosphate glasses doped with less than 5 mol% praseodymium oxides," University of North Dakota, Grand Forks, 2012.

[61] J. E. Shelby, Introduction to glass science and Technology, Royal Society of Chemistry, 2005.

[62] U. Hoppe, "Behavior of the packing densities of alkali germanate glasses," *Journal of Non-Crystalline Solids,* vol. 248, pp. 11-18, 1999.

[63] A. Mandlule, F. Döhler, L. . v. Wüllen, T. Kasuga and D. S. Brauer, "Changes in structure and thermal properties with phosphate content of ternary calcium sodium phosphate glasses," *Journal of Non-Crystalline Solids,* vol. 392–393, p. 31–38, 2014.

[64] J. J. Hudgens' and S. W. Martin, "Glass Transition and Infrared Spectra of Low-Alkali, Anhydrous Lithium Phosphate Glasses," *Journal of American Ceramic Society,* vol. 76, no. 7, pp. 1691-96 , 1993.

[65] P. Y. Shih, "Thermal, chemical and structural characteristics of erbium-doped sodium phosphate glasses," *Materials Chemistry and Physic,* vol. 84, pp. 151-156, 2004.

[66] N. H. Ray, "The Relationship between Crosslink Density and Transformation Temperature in Phosphate Glasses," *Journal of Polymer Science,* vol. 11, pp. 2169-2177, 1973.

[67] A. Mandlule, F. Döhler, L. v. Wüllen, T. Kasuga and D. S. Brauer, "Changes in structure and thermal properties with phosphate content of ternary calcium sodium phosphate glasses," *Journal of Non-Crystalline solids,* Vols. 392-393, pp. 31-38, 2014.

[68] A. K. Varshneya , Fundamental of Inorganic Glasses, Academic Press, 1993.

[69] R. D. Shannon, "Revised effective ionic radii and systematic studies of interatomic distances in halides and chalcogenides," *Acta Cryst A,* vol. 32, pp. 751-767, 1976.

[70] K. Sun, and W. M. Risen Jr., "Rare earth phosphate glasses," *Solid State Communications,* vol. 60, no. 9, pp. 697-700, 1986.

[71] G. J. Exarhos, P. J. Miller and W. M. Risen Jr, "Interionic vibrations and glass transitions in ionic oxide metaphosphate glasses," *Journal of chemical Physics,* vol. 60, no. 11, p. 4145, 1974.

[72] G. B. Rouse Jr, P. J. Miller and W. M. Risen Jr., "Mixed alkali glass spectra and structure," *Journal of Non-Crystallline solids,* vol. 28, no. 2, pp. 193-200, 1978.

[73] B. N. Nelson and G. J. Exarhos, ""Vibrational spectroscopy of cation-site interactions in phosphate glasses," *journal of chemical Physics,* vol. 71, no. 7, pp. 2739-2747, 1979.

[74] L. N. Ma, "Dissolution behavior of phosphate glasses," 2014.

[75] P. Y. Shih, S. W. yung and T. S. Chin, "Thermal and corrosion behavior of P2O5-Na2O-CuO glasses," *Journal of Non-Crystalline Solids,* vol. 224, no. 2, pp. 143-152, 1998.

[76] J. E. James E. Shelby and J. T. Kohl, "Rare-Earth Aluminosilicate Glasses," *Journal of American Ceramic society,* vol. 73, no. 1, pp. 39-42, 1990.

[77] F. Baucke a and J. Duffy, "Oxidation states of metal ions in glass melts," *Physics and Chemistry of Glasses,* vol. 35, no. 1, pp. 17-21, 1994.

[78] E. I. Kamitsos,, "Infrared study of agi- containing superionic glasse," *Physics and Chemistry of Glasses,* vol. 36, no. 3, pp. 141-149, 1995.

[79] M. Karabulut, E. Metwalli, A. K. wittenauer, R. K. Brow, G. K. Marasinghe, C. H. Booth, J. J. Bucher and D. K. Shuh, "An EXFAS investigation of rare-earth local environment in ultraphosphate glasses," *Journal of non-crystalline solids,* vol. 351, pp. 795 - 801, 2005.

[80] C. Yoo, "X-ray absorption spectroscopy studies of the atomic structure of zirconium-doped lithium silicate glasses and glass-ceramic, zirconium-doped lithium borate glasses and vitreous rare-earth phosphates," University of North Dakota, Grand Forks, 2016.

[81] M. Ajroud, M. Haouari , O. Ben, H. Maaref, A. Brenier and C. Garapon, "Investigation of the spectroscopic properties of Nd3+-doped phosphate glasses," *Journal of Physics : condensed Matters,* vol. 12, no. 13, p. 3181, 2000.

[82] H. Ebendorff-Heidepriem and D. Ehrt, "Optical spectroscopy of rare-earth ions in glasses," *Glastech Ber : Glasses Sci Tech,* vol. 71, no. 10, p. 289, 1998.

[83] V. Mehta, G. Aka, A. L. Dawar and a. Mansingh, "Optical properties and spectroscopic parameters of Nd doped phosphate and borate glasses," *Optical Materials,* vol. 12, pp. 53-63, 1999.

[84] M. P. Hehlen, M. G. Brik and K. W. Kramer, "50th anniversary of the Judd-ofelt theory: An experimental's view of the formalism and its application," *Journal of Luminescence ,* vol. 136, pp. 221-239, 2013.

[85] D. K. Sardar, J. B. Gruber , B. Zandi , J. A. Hutchinson and C. W. Trussel, "Judd–Ofelt analysis of the Er3+(4f11)Er3+(4f11) absorption intensities in phosphate glass: Er3+,Er3+,," *Journal of Applied Physics,* vol. 93, no. 4, pp. 2041-2046, 2003.

[86] Y. Yan, A. J. Faber and H. De Waal, "Luminescence quenching by OH groups in highly Er-doped phosphate glasses," *Journal of Non-Crystalline solids,* vol. 181, no. 3, pp. 283-290, 1995.

[87] X. Feng, S. Tanabe and T. Hanada, "Hydroxyl grops in erbium doped germanotellurite glasse," *Journal of non-crystalline solids,* vol. 281, pp. 48-54, 2001.

[88] S. Dai, C. Yu, G. Zhou, J. Zhang, G. Wang and L. Hu, "Concnetration quenching in erbium doped tellurite glasses," *Journal of Luminescence,* vol. 117, pp. 39-45, 2006.

[89] Z. Jiang, J. Yang and S. Dai, "Optical spectroscopy and gain properties of Nd3+-doped oxide glasses," *J.opt Soc Am B,* vol. 21, pp. 739-743, 2004.

[90] F. Auzel, F. Bonfigli and S. Gagliari, "The interplay of self-trapping and self-quenching for resonant transitions in solids; role of a cavity," *Journal of Luminescence,* vol. 94 & 95, pp. 293-297, 2001.

[91] F. Auzel, G. Balacchini, L. Laversenne and G. Boulon, "Radiation trapping and self-quenching analysis in Yb3+, Er3+, and Ho3+ doped Y2O3," *Optical Material,* vol. 24, no. 1-2, pp. 103-109, 2003.

[92] W. J. Miniscalco, "Erbium doped glasses for Fiber amplifer at 1500 nm," *Journal of Lightwave technology ,* vol. 9, no. 2, pp. 234-250, 1991.

[93] T. Kushida, "Energy transfer and cooperative optical transitions in rare-earth doped inorganic materials. III. Dominant transfer mechanism," *J. Phys. Soc. Jpn.,* vol. 34, pp. 1334-1337 , 1973.

[94] L. Agazzi, "Spectroscopic Excitation and Quenching Processes in Rare-Earth-Ion-Doped Al2O3 and their Impact on Amplifier and Laser Performance," 2012.

[95] V. M. Martin, D. N. Messias, N. O. Dantas and A. M. Neto, "Concentration dependence fluorescence quantum efficiency of Neodymium doped phosphate glass matrix," *Journal of Luminescence,* vol. 130, pp. 2491 - 2494, 2010.

[96] A. A. Andrade, V. Pilla, S. A. Lourenco, A. C. Silva and N. O. Dantas, "Flourescence quantum efficiency dependent on the concentration of Nd doped phosphate glasses," *chemical Physics letters,* vol. 547, pp. 38-41, 2012.

[97] R. Balakrishnaiah, P. Babu, C. K. Jayasankar, A. S. Joshi, A. Speghini and M. Bettinelli, "Optical and Luminescence properties of Nd ions in K-Ba-Al phosphate and fluorophosphate glasses," *Journal of Physics: Condensed Matter,* vol. 18, pp. 165 -179, 2006.

[98] H. Ebendorff-Heidepriem, W. Seeber and D. Ehrt, "Spectroscopic properties of Nd3+ ion inphosphate glasses," *journal of non-crystalline solids,* vol. 183, pp. 191-200, 1995.

[99] V. Lupei, A. Lupei and S. Georgescu, "Effects of energy transfer on quanYAG:Nd," *Journal of applied Physics,* vol. 66, no. 8, p. 3792, 1989.

[100] A. Lupei, V. Lupei and S. Geoorgescu, "High-resolution spectroscopyof Nd^3+ in YALO3," *Journal of physics : condensed matter,* vol. 4, no. 12, p. L221, 1992.

[101] Y. L. Lu, Y. Q. Lu and N. B. Ming, "Fluroescence and attenuation propertie sof ER doped phospahte glasses fibers and efficinet infrared to visible up conversion," *Applied physics B,* vol. 62, pp. 287 - 291, 1996.

[102] Y. Yan, a. J. Faber and H. D. Wall, "Luminescence quenching by OH group in highly Er-doped Phospahte glasses," *Journal of Non-crystalline Solids,* vol. 181, pp. 283-290, 1995.

[103] A. A. Reddy, S. S. Babu and G. V. Prakash, "Er doped phospahte glasses with improved gain characteristics for broadband optical amplifiers," *optical communications,* vol. 285, pp. 5364 - 5367, 2012.

[104] P. Babu, H. J. Seo, K. H. Jang, R. Balakrishnaiah and C. K. Jayasankar, "Optical spectroscopy 1.5 micron emission and upconversion properties of Er doped

metaphsopahte laser glasses," *journal of optical society america B,* vol. 24, no. 9, pp. 2218- 2227, 2007.

[105] K. Pradesh and C. J. Oton, "Optical Properties of Er doped alkali chlorophosphate glasses for optical amplifiers," *Optical Materials,* vol. 31, pp. 155-160, 2008.

[106] D. E. McCumber, ""“Einstein relations connecting broadband emission and absorption spectra,”," *Phys Rev,* vol. 136, pp. 954 - 957, 1964.

[107] J. h. Cambell and T. I. suratwala, "Nd-doped phosphate glasses for high-energy/high-peak power lasers," *Journal of Non-crystalline solids,* vol. 263 & 264, pp. 318 - 341, 2000.

[108] D. Yan-Li, S. Zhen-Rong and G. Fu-Xi, "Spectroscopic properties of Nd-doped phosphate glass with a high emission cross section," *Chinese physics IOP,* vol. 11, no. 6, pp. 613 - 618, 2002.

[109] H. Ebendroff-Heidepriem, W. Seeber and D. Ehrt, "Spectroscopic properties of Nd ions in phosphate glasses," *Journal of Non-Crystalline Solids,* vol. 183, pp. 191 - 200, 1995.

[110] B. C. Bunker, G. W. Arnold,, M. Rajaram and D. E. Day, "Corrosion of Phosphorus oxynitride glasses in water and humid air," *Journal of the American Ceramic Society,,* vol. 70, no. 6, pp. 425-430, 1984.

[111] D. Pugliese, N. G. Boetti and J. Lousteau, "Concentration quenching in an Er-doped phosphate glass for compact optical lasers and amplifiers," *Journal of Alloys and compounds,* vol. 657, pp. 678-683, 2016.

Chapter 5

CONCLUSION

The atomic-scale structure of rare-earth doped ultraphosphate glasses of composition $(RE_2O_3)_x(Na_2O)_y(P_2O_5)_{1-x-y}$, where $RE = Pr, Nd,$ and Er ($0.005 \leq x \leq 0.05$), has been investigated using high-energy X-ray diffraction technique (HEXRD). Thermal property measurements, optical spectroscopy, and Fourier transform infrared spectroscopy (FTIR) have been used as complementary techniques. The diffraction technique is crucial to extract information about structural features such as inter-atomic distances and coordination numbers and their dependence on the concentration of RE_2O_3. Such information has been obtained by analyzing pair distribution functions obtained from diffraction data. However, the atomic-level structure of glasses is disordered and a single diffraction technique alone cannot give a detailed picture of the atomic-level structure. Hence, data from above mentioned complementary techniques were utilized in this project to further investigate the atomic arrangement. The major research findings and their significance are summarized as follows.

5.1 Physical and Thermal Properties

The density and molar volume of glasses increase linearly with increasing RE_2O_3 concentration. The linear increase in density is a result of lighter atoms Na being replaced by heavier

RE atoms. Whereas, the increase in the molar volume indicates that the incorporation of RE_2O_3 makes the glass network open by expanding the structure. The change in the molar volume with RE_2O_3 concentration is also an indication that the modification that takes place through the depolymerization of glass network. The opening of the linkages between the phosphate chains takes places by breaking the bridge between two Q^2 networks.

The glass transition temperature (T_g) increases with RE_2O_3 concentration. This is due to increase in cross link density. This increase indicates that the incorporation of RE^{3+} strengthens the glass network. The slopes of T_g vs. RE^{3+} concentration graphs indicate that the cation field strength increases from Pr^{3+} to Er^{3+}.

5.2 Vibrational Properties

The $P-O^-$ band of FTIR spectra represents *NBO* bonds of Q^2 groups. This band shifts towards lower frequencies as Na_2O is substituted with RE_2O_3. This shifting of the *P-O*$^-$ band towards lower frequencies with increasing RE^{3+} concentration can be attributed to an increase in the number of $P-O^--RE^+$ linkages in the network. Because the field strength of RE^{3+} ion is higher than that of Na^+ ions, $P-O-P$ angles become smaller and phosphate chains become shorter with increasing RE^{3+}concentration. The presence of RE^{3+} distort the phosphate chains by increasing the cross-link density.

5.3 High energy X-ray Diffraction

The average $P-O$ coordination number (CN_{P-O}) is 3.8, slightly less than the expected value of four. This discrepancy may be attributed to relatively severe Fourier series termination ripples in the low r-region of pair distribution functions. The average CN_{P-O} and $P-O$ distance do not depend on the type rare earth dopant.

The CN_{RE-O} decreases by approximately 0.5 when the RE_2O_3 concentration increases from $x = 0.005$ to 0.05 for preseodymium and neodymium doped glasses. The corresponding change for erbium doped glasses is approximately 0.8. The average $Na - O$ coordination number CN_{Na-O}, which is approximately five, is independent of both the rare-earth concnetration and the type of rare earth ion.

5.4 Optical Properties

The decreasing of Judd-Ofelt parameter Ω_2 with increasing Nd^{3+} concentration suggests that the chemical bond $Nd - O$ is more ionic in nature than $P - O$. The decrease in Ω_6 is related to the decrease in the $\sigma - bond$ between $Nd - O$. Furthermore, this decrease in Ω_6 indicates an increase in electron density donated from the oxygen by decreasing the Coulombic interaction between the $Nd - O$. The lifetimes of level $^4I_{13/2}$ of Er^{3+} ions and $^4F_{3/2}$ level of Nd^{3+} ions decrease with increasing RE^{3+} concentration. The decrease in the lifetime is attributed to energy migrations process due to concentration quenching and the likely presence of OH^- group. The concentration quenching model indicates that the quenching starts at approximately $x = 0.01$ in erbium glasses. In contrast, quenching appears to start after $x = 0.04$ in neodymium-doped glasses. It is assumed that concentration quenching is the main contributing process in decreasing the lifetime of Er^{3+} ions along with the OH group. The number of particles participating in the interaction process is approximately three, which indicates that the energy is first transferred to a nearby donor (Er^{3+}) ion and then to the acceptor OH^- group. For neodymium glasses, the OH^- group is the leading energy transfer process because the number of particles participate in interaction is 2.

The Inokuti-Hirayama (IH) model analysis of the non-exponential nature of the decay curves reveals that the interaction responsible for cross-relaxation between the acceptor and donor ions is

of dipole-dipole type for Nd^{3+} ions, which increase with the concentration of Nd^{3+}. Furthermore, the energy transfer parameter (Q) increases with Nd_2O_3 concentration by decreasing the average separation distance between the two Nd^{3+} ions.